RETHINKING FAIRNESS IN MULTIMODAL LARGE LANGUAGE MODELS FOR MEDICAL IMAGING

Anonymous authors
Paper under double-blind review

ABSTRACT

Multimodal large language models (MLLMs) now answer clinical questions and draft radiology reports at expert-competitive quality, yet early audits show that their outputs differ in quality across demographic groups. Fairness in medical imaging has been studied extensively, but almost entirely for models that predict a label from an image alone, and the few studies of medical MLLMs are purely empirical and narrow in scope. As a result, there is no theoretical account of how unfairness arises in an MLLM, which is conditioned on both an image and a textual query and produces open-ended text, and no systematic benchmark to measure it. We address both gaps with MedFairVLM. We first define a fairness criterion for open-ended generation as the disparity in LLM-as-a-judge scores between demographic groups. Building on it, we derive an upper bound on the unfairness of an MLLM that decomposes it into five sources of bias: disparities in the image distribution, in the query distribution, in the two conditional dependencies between image and query, and in response generation given both inputs. We extend the bound to distribution shift and provide an estimator that quantifies each bias source from data. We then benchmark ten open-source and commercial MLLMs on eight datasets spanning four imaging modalities, four organs, and four sensitive attributes, across closed-ended visual question answering (VQA), open-ended VQA, and report generation, under zero-shot, fine-tuning, and distribution-shift scenarios. Unfairness is prevalent across all models and settings; under fine-tuning, fairness behavior is highly correlated with the bias sources identified by our theory; existing fairness methods fail to mitigate bias consistently; and distribution shift makes fairness harder still to control.

1 INTRODUCTION

Multimodal large language models (MLLMs) couple a language backbone with an image encoder, turning LLMs into systems that can hold open-ended, image-grounded dialogue (OpenAI, 2023; Liu et al., 2023; Yang et al., 2025a). Medicine is a natural target for this paradigm, and a rapid succession of medical MLLMs, from LLaVA-Med to Med-Gemini and MedGemma (Li et al., 2023; Saab et al., 2024; Sellergren et al., 2025), now reaches expert-competitive quality on radiology report generation and medical visual question answering (VQA) (Tu et al., 2024; Zambrano Chaves et al., 2025). These models, however, inherit the fairness failures of their unimodal ancestors: LLMs change their clinical recommendations when a patient's stated demographics change (Zack et al., 2024; Omar et al., 2025), and MLLMs answer visual questions less accurately for some genders and races than for others (Hall et al., 2023; Wu et al., 2025; Wang et al., 2026). In medical imaging the stakes are higher, because model outputs can shape triage, diagnosis, and treatment. Recent audits already find that medical MLLMs answer less accurately, and write lower-quality reports, for older, female, and racial-minority patients (Xia et al., 2024; Wu et al., 2024; Bhosale et al., 2026).

Such disparities are not new to medical imaging, where fairness has been studied extensively, though almost entirely for models that predict a label rather than generate text. Classical task-specific classifiers underdiagnose under-served subgroups and encode protected attributes such as race (Seyyed-Kalantari et al., 2021b; Gichoya et al., 2022), and fairness methods rarely beat empirical risk minimization (Zong et al., 2023; Pham et al., 2025a). Vision foundation models show the same disparities in classification and segmentation (Jin et al., 2024), and zero-shot vision–language models underdiagnose marginalized groups more severely than radiologists (Yang et al., 2025b). This literature,

Reviewers: please read the Reviewer Guidelines (iclr.cc/Conferences/2027/ReviewerGuidelines) and the AI Policy for Reviewers (iclr.cc/Conferences/2027/AIPolicyForReviewers). If you used AI to expand, edit, or polish your review, please provide the input text to the LLM. Better still, consider skipping the LLM and submitting your original text: we, and the authors, are much more interested in your unedited thoughts than in what an LLM has to say. AI-assisted or not, you are putting your name and reputation behind your review: LLM-generated falsehoods, hallucinations or misrepresentations are subject to disciplinary action, which may include desk-rejecting all papers you have authored.

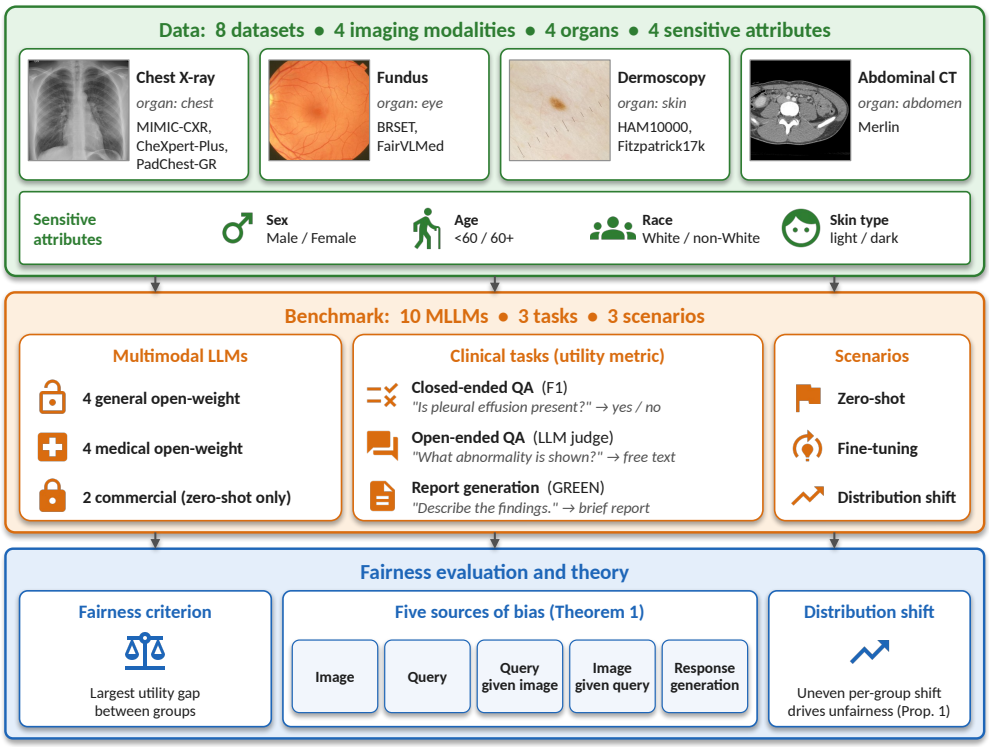

Figure 1: Overview of MedFairVLM. **Data:** eight medical imaging datasets covering chest X-ray, fundus, dermoscopy, and abdominal CT, with binarized sensitive attributes. **Benchmark:** ten MLLMs (general and medical open-weight models and two commercial models) evaluated on closed-ended QA, open-ended QA, and report generation, each with its own utility metric, under zero-shot, fine-tuning, and distribution-shift scenarios. **Fairness evaluation and theory:** the group-fairness criterion and its EMI-based proxy FEMI, the five model-independent sources of bias that bound FEMI (Theorem 1), and the behavior of FEMI under distribution shift (Proposition 1).

however, targets *prediction* rather than the *generation* tasks that make MLLMs useful, and treats the image as the only input, whereas an MLLM also conditions on a textual query. Fairness research on medical MLLMs themselves is only beginning (Xia et al., 2024; Wu et al., 2024; Bhosale et al., 2026) and leaves two gaps. First, it is purely empirical: with *no theoretical account* of how unfairness arises inside an MLLM, observed unfairness cannot be traced to the images, the prompts, their alignment, or the decoder, nor matched to a remedy (Jones et al., 2024). Second, there is *no systematic benchmark*: fairness is either one dimension of a broader trustworthiness audit or is studied on one or two modalities with a few open-source models, so no single study spans modalities, organs, tasks, commercial models, and deployment scenarios such as fine-tuning and distribution shift.

Closing these gaps is not a matter of re-running classical fairness pipelines on a new model class. Fairness criteria such as equalized odds (Hardt et al., 2016) presume a calibrated score or a binary decision, whereas open-ended generation yields a token sequence with no single ground-truth label, many valid phrasings of the same finding, and omissions that can be as harmful as errors (Suriyakumar et al., 2025; Gallegos et al., 2024). The language-only workaround, swapping a demographic word in the prompt and checking whether the output changes (Sheng et al., 2019), does not transfer either: medical prompts and reports rarely mention demographics, and the demographic signal is hidden in the image instead, where models can read it even when radiologists cannot (Gichoya et al., 2022; Yang et al., 2024). Measuring fairness in MLLMs therefore requires a notion of disparity defined over the whole generated text, clinically meaningful metrics to judge that text, and a way to attribute the disparity to the image, the query, or the generation process.

In this paper we step back and ask a foundational question: *where does unfairness in a medical MLLM come from, and how should it be measured?* We answer it with **MedFairVLM**, a theoretically grounded framework and benchmark for fairness in MLLMs for medical imaging (Figure 1). We first define a new fairness criterion for open-ended generation: the disparity in LLM-as-a-judge

scores between demographic groups, which aligns fairness with the standard way of evaluating generated text (Zheng et al., 2023; Ostmeier et al., 2024). Building on this criterion, we formulate an MLLM as a conditional distribution $P_{Y_\theta|X}$ of its response Y_θ given the multimodal input $X = (X_v, X_t)$ of image X_v and query X_t, and derive an upper bound on unfairness that decomposes it into five interpretable sources of bias: disparities in (i) the *image* distribution, (ii) the *query* distribution, (iii) the dependence of the query on the image, (iv) the dependence of the image on the query, and (v) the *response generation* given both inputs. We extend the analysis to distribution shift and propose an estimation procedure that quantifies each term from finite samples, so that observed unfairness can be attributed to its dominant source. Finally, we build a benchmark that evaluates ten open-source and commercial MLLMs on eight datasets spanning four imaging modalities, four organs, and four sensitive attributes, across three tasks (closed-ended VQA, open-ended VQA, and report generation) and three scenarios (zero-shot inference, fine-tuning, and distribution shift). Together, the theory and the benchmark let us not only detect unfairness in medical MLLMs but also explain where it comes from.

Our contributions are summarized as follows.

- **Theory.** A new fairness criterion for open-ended generation aligned with LLM-as-a-judge evaluation, and, to our knowledge, the first theoretical-inspired decomposition of group fairness for MLLMs: a bound on this criterion that decomposes unfairness into five sources of bias.
- **Bias source quantification.** A practical estimator for each source, enabling diagnosis of *why* a model is unfair rather than merely *whether* it is.
- **Benchmark.** MedFairVLM, covering ten MLLMs, eight datasets, four modalities, four organs, four sensitive attributes, three tasks, and three deployment scenarios.
- **Findings.** (i) Unfairness is prevalent across all ten MLLMs and across all tasks and scenarios; (ii) under fine-tuning, a model's fairness behavior is highly correlated with the bias sources identified by our theory; (iii) existing fairness methods fail to mitigate unfairness consistently; and (iv) distribution shift makes fairness even harder to control.

2 Problem Formulation

Notation. A sample is a tuple of random variables (X_v, X_t, Y, A): a medical image $X_v \in \mathcal{X}_v$, a textual query $X_t \in \mathcal{X}_t$, a reference response $Y \in \mathcal{Y}$, and a sensitive attribute $A \in \mathcal{A}$ from a finite set of demographic groups; $X = (X_v, X_t) \in \mathcal{X}$ is the multimodal input. We denote by P_{XY} the joint distribution of (X, Y), by $P_{Y|X}$ the ground-truth conditional distribution, and by $P^{(a)}_{XY} := P_{XY|A=a}$ the distribution of group a (likewise for its marginals and conditionals, e.g., $P^{(a)}_{X_t|X_v}$). An MLLM with parameters θ defines a conditional distribution $P_{Y_\theta|X}$ that approximates $P_{Y|X}$; its response $Y_\theta \sim P_{Y_\theta|X}$ induces the joint distribution $P^{(a)}_{XY_\theta} := P^{(a)}_X P_{Y_\theta|X}$ on group a.

Fairness criterion. Under group fairness, which requires equal performance across groups (Hardt et al., 2016; Zong et al., 2023), we define unfairness as the largest gap in a group-wise performance score $M^{(a)}(\theta)$,

$$\mathrm{F}_M(\theta) := \max_{a,a' \in \mathcal{A}} \left| M^{(a)}(\theta) - M^{(a')}(\theta) \right|, \tag{1}$$

where M is the F1 score in the closed-ended setting and an LLM-as-a-judge score (Zheng et al., 2023) in the open-ended setting. Because judge scores come from a black-box model, our theory replaces them with the effective mutual information (EMI) of Oh et al. (2025), $\mathrm{EMI}^{(a)}(\theta) := I_{P^{(a)}_{XY_\theta}}(X; Y_\theta) - I_{P^{(a)}_{XY}}(X; Y)$, the input information in the model's responses beyond that in the references; EMI is a suitable proxy because it is provably close to the judge-based relative preference score whenever $P_{Y_\theta|X}$ approximates $P_{Y|X}$, and the two correlate strongly in practice (Oh et al., 2025). Taking $M = \mathrm{EMI}$ in Eq. (1) gives our criterion, the *fairness-EMI* $\mathrm{FEMI}(\theta) := \max_{a,a' \in \mathcal{A}} |\mathrm{EMI}^{(a)}(\theta) - \mathrm{EMI}^{(a')}(\theta)|$, the largest difference in EMI between two groups.

Discrepancy measure. We measure the discrepancy between distributions P and Q by the Jensen–Shannon distance $d_{\mathrm{JS}}(P, Q) := \sqrt{D_{\mathrm{JS}}(P \,\|\, Q)}$, the root Jensen–Shannon divergence in base

two (Lin, 1991); unlike KL, it is symmetric, bounded in $[0, 1]$, and a metric (Endres & Schindelin, 2003). For conditional distributions we use $d_{\mathrm{JS,c}}(P_{Y|X}, Q_{Y|X}) := \big(\mathbb{E}_{P_X}[D_{\mathrm{JS}}(P_{Y|X} \,\|\, Q_{Y|X})] + \mathbb{E}_{Q_X}[D_{\mathrm{JS}}(P_{Y|X} \,\|\, Q_{Y|X})]\big)^{1/2}$, summing over both input marginals.

3 Theoretical Analysis

This section asks where the unfairness of an MLLM comes from. For a given model, FEMI compares the same $P_{Y_\theta|X}$ across groups, so unfairness arises when the model meets group-specific data: each group's input distribution $P_X^{(a)}$ and reference response distribution $P_{Y|X}^{(a)}$. Different models respond differently to the same data and so attain different FEMI, but for any given model its unfairness can be traced to differences in these two distributions. Section 3.1 bounds FEMI by five measurable differences between group distributions, Section 3.2 studies how FEMI changes when the model is deployed on a new population, and Section 3.3 estimates the five differences from data so that observed unfairness can be attributed to its dominant source. All proofs are given in Appendix B.

3.1 Fairness Bound for Multimodal LLMs

Assumption 1 (Bounded response probability)**.** *There exists a constant $C < \infty$ such that the reference and model response distributions satisfy $-\log P_{Y|X}^{(a)} \le C$ and $-\log P_{Y_\theta|X} \le C$, $\forall a \in \mathcal{A}$.*

We note that bounded-loss assumptions of this kind are commonly used in learning theory and domain adaptation (Mansour et al., 2009; Cortes & Mohri, 2014; Nguyen et al., 2022; Pham et al., 2024; 2025b). This assumption is reasonable rather than stringent.

Theorem 1 (Fairness bound for MLLMs)**.** *Under Assumption 1, for any parameters θ,*

$$\mathrm{FEMI}(\theta) \le \max_{a \neq a'} \Big\{ \kappa_{a,a'} \Big[\underbrace{d_{\mathrm{JS}}\big(P_{X_v}^{(a)}, P_{X_v}^{(a')}\big)}_{\textit{(i) image}} + \underbrace{d_{\mathrm{JS}}\big(P_{X_t}^{(a)}, P_{X_t}^{(a')}\big)}_{\textit{(ii) query}} + \underbrace{d_{\mathrm{JS,c}}\big(P_{X_t|X_v}^{(a)}, P_{X_t|X_v}^{(a')}\big)}_{\textit{(iii) query given image}} + \underbrace{d_{\mathrm{JS,c}}\big(P_{X_v|X_t}^{(a)}, P_{X_v|X_t}^{(a')}\big)}_{\textit{(iv) image given query}} \Big] + \kappa' \underbrace{d_{\mathrm{JS,c}}\big(P_{Y|X}^{(a)}, P_{Y|X}^{(a')}\big)}_{\textit{(v) response generation}} \Big\}, \tag{2}$$

where $\kappa_{a,a'} := \widehat{H}_{a,a'} + \sqrt{2}\,(2 + \sqrt{2}\,C)$, $\kappa' := \frac{2+\sqrt{2}}{2}\,(2 + \sqrt{2}\,C)$, and $\widehat{H}_{a,a'} := \frac{1}{2}\big[\sup_x H(P_{Y|X=x}^{(a)}) + \sup_x H(P_{Y|X=x}^{(a')})\big] + \sup_x H(P_{Y_\theta|X=x})$ is an output-entropy scale.

Five sources of bias. Because Eq. (2) is an upper bound, reducing any of the five distances on its right-hand side lowers the bound on FEMI, so each is an indicator to track fairness. We therefore call these five distances the *sources of bias* of an MLLM. Terms (i) and (ii) are *marginal* disparities: groups whose images or queries are distributed differently, for instance because one group is imaged with different equipment or asked different questions. Terms (iii) and (iv) are *cross-modal* disparities: groups may share the same image and query marginals yet pair them differently, for example when the questions asked about a finding depend on who the patient is; these terms vanish exactly when the coupling of image and query is the same across groups. Term (v) is the disparity in the *response generation*: the reference response distribution given the input may differ across groups, for instance when radiologists describe the same finding differently for different patients.

Model-independent sources of bias. The five sources in Theorem 1 are distances between group distributions on the data space, so they depend on the dataset alone and not on the model. This is a deliberate choice. An MLLM does not learn $P_{Y|X}$ from raw pixels and tokens; it first maps the image and the query to representations through its encoders and then learns the mapping from those representations to the response, and an analogous bound could be derived with the sources measured in that representation space. Such sources, however, would be entangled with the encoders of one particular model, would take different values for every model evaluated on the same data, and could not separate what the dataset contributes to unfairness from what the model contributes. Data-space sources are shared by all models evaluated on a dataset, which is exactly what we need to ask how properties of medical imaging datasets shape the fairness behavior of MLLMs, and to compare that behavior across the ten models in our benchmark on equal footing.

Notes on Theorem 1. Besides the five sources of bias, the right-hand side of Eq. (2) contains the constants $\kappa_{a,a'}$ and κ', which depend on the model through its output entropy and on the bound C. We thus use the theorem to identify which data-level disparities can drive unfairness and to track how unfairness changes with them, not to approximate the value of FEMI: the estimated sources are reported and compared entry by entry in Section 4, and are never used to certify a FEMI value.

3.2 Fairness under Distribution Shift

In practice, an MLLM is developed on one population but deployed on another, for example a different hospital or patient cohort. We therefore ask how FEMI changes when a trained model is moved from the source population P on which it was developed to a target population Q, where both populations contain the same groups $\mathcal{A}$ and Assumption 1 holds for every group in both. Since EMI and FEMI now depend on which population they are computed on, we add the population as a subscript, writing $\mathrm{EMI}_P^{(a)}(\theta)$ and $\mathrm{FEMI}_P(\theta)$ for their values under P and $\mathrm{EMI}_Q^{(a)}(\theta)$ and $\mathrm{FEMI}_Q(\theta)$ under Q, and define the group-wise shift $s_a := \mathrm{EMI}_Q^{(a)}(\theta) - \mathrm{EMI}_P^{(a)}(\theta), a \in \mathcal{A}$, the change in model performance of group a when moving from P to Q.

Per-group OOD sources. We define per-group OOD sources between $P^{(a)}$ and $Q^{(a)}$ as:

$$\mathcal{I}_a := d_{\mathrm{JS}}\big(P_{X_v}^{(a)}, Q_{X_v}^{(a)}\big) + d_{\mathrm{JS}}\big(P_{X_t}^{(a)}, Q_{X_t}^{(a)}\big) + d_{\mathrm{JS,c}}\big(P_{X_t|X_v}^{(a)}, Q_{X_t|X_v}^{(a)}\big) + d_{\mathrm{JS,c}}\big(P_{X_v|X_t}^{(a)}, Q_{X_v|X_t}^{(a)}\big),$$
$$\mathcal{R}_a := d_{\mathrm{JS,c}}\big(P_{Y|X}^{(a)}, Q_{Y|X}^{(a)}\big)$$

These terms correspond to the bias sources in Theorem 1, with the group pair (a, a') replaced by $(P^{(a)}, Q^{(a)})$. Accordingly, let $\kappa_a := \widehat{H}_a + \sqrt{2}\,(2 + \sqrt{2}\,C)$ with $\widehat{H}_a := \frac{1}{2}\big[\sup_x H(P_{Y|X=x}^{(a)}) + \sup_x H(Q_{Y|X=x}^{(a)})\big] + \sup_x H(P_{Y_\theta|X=x})$, with κ' as in Theorem 1, and define $\Delta_a := \kappa_a\,\mathcal{I}_a + \kappa'\,\mathcal{R}_a$.

Proposition 1 (FEMI under distribution shift)**.** *Under Assumption 1 for every group in P and in Q, for any parameters θ,*

$$\big|\mathrm{FEMI}_Q(\theta) - \mathrm{FEMI}_P(\theta)\big| \;\le\; \max_{a,a' \in \mathcal{A}} |s_a - s_{a'}| \;\le\; \max_{a,a' \in \mathcal{A}} \big(\Delta_a + \Delta_{a'}\big). \tag{3}$$

Fairness change is driven by uneven shift. The first inequality of Proposition 1 states that the change in unfairness under distribution shift is governed by how unevenly the shift affects the performance of the individual groups, as measured by their EMI. If every group's EMI changes by the same amount, however large, FEMI is unchanged; if the shift improves one group and degrades another, FEMI can change by up to their difference. The second inequality further relates this change in unfairness to group-specific OOD sources, quantifying how much each group's images, queries, image-query coupling, and reference responses differ between P and Q. Fairness established on a source population therefore carries over to a target population only when the shift affects all groups alike, which is rarely the case across hospitals, scanners, or patient cohorts and explains why unfairness can grow under shift even for a model that is fair in-distribution.

3.3 Quantifying the Sources of Bias

Theorem 1 involves population-level Jensen–Shannon distances, but a benchmark provides only few thousand samples per group, too few to estimate the density ratios they require, and the conditional distances compare distributions at inputs that never repeat. We therefore design an estimation procedure in which each estimated source vanishes whenever its theoretical counterpart does, and no source is inflated by group size; details are given in Appendix C.

Frozen embeddings. Because the sources of bias are model-independent (Section 3.1), they are estimated in a space that does not depend on the MLLM under evaluation. We therefore compute all quantities on frozen embeddings: Z_v from a CLIP image encoder (Radford et al., 2021) and Z_t, Z_y, Z_{y_θ} from one text encoder applied to the query, the reference response, and the model response, with Z_x the joint input embedding. The encoders are pretrained and frozen, and everything derived from them is computed once per dataset on all groups pooled and shared by all groups and models, so the representation cannot itself create a between-group difference.

EMI and FEMI. Group-wise EMI is the difference of two mutual informations, between the input and the model response and between the input and the reference response, both estimated with CLUB (Cheng et al., 2020); FEMI is the largest gap between the group-wise values.

Marginal distribution divergences (sources (i) and (ii)). We compare embedding distributions with kernel methods, which need only samples: each embedding space carries an RBF kernel k with bandwidth set by the median heuristic, and $\mathcal{H}$ denotes its reproducing kernel Hilbert space. Sources (i) and (ii) are then estimated as the maximum mean discrepancy (MMD) between the two groups' distributions of the image embedding $Z = Z_v$, respectively the query embedding $Z = Z_t$, $\mathrm{MMD}^2\big(P_Z^{(a)}, P_Z^{(a')}\big) = \|\mu_Z^{(a)} - \mu_Z^{(a')}\|_{\mathcal{H}}^2$ with $\mu_Z^{(a)} = \mathbb{E}_{P_Z^{(a)}}[k(Z,\cdot)]$ the kernel mean embedding of group a, using the unbiased estimator of Gretton et al. (2012); since the RBF kernel is characteristic, MMD vanishes exactly when the two groups' embedding distributions coincide.

Conditional distribution divergences (sources (iii) to (v)). For $(V,U) = (Z_v, Z_t)$, (Z_t, Z_v), and (Z_x, Z_y) respectively, we estimate within each group a the conditional mean embedding $\mu_{U|V=v}^{(a)} = \mathbb{E}^{(a)}[k(U,\cdot) \mid V = v] \in \mathcal{H}$, the analogue of $\mu_Z^{(a)}$ conditioned on $V = v$, by kernel ridge regression (Song et al., 2009; Grünewälder et al., 2012; Park & Muandet, 2020), which pools information across similar inputs. The two groups are then compared by the kernel conditional discrepancy of Park et al. (2021), which we take with a balanced reference measure and which we write as

$$\mathrm{CMMD}^2 := \mathbb{E}_{V\sim\rho}\big\|\mu_{U|V}^{(a)} - \mu_{U|V}^{(a')}\big\|^2, \qquad \rho := \tfrac{1}{2}\big(P_V^{(a)} + P_V^{(a')}\big), \tag{4}$$

which sums over the inputs of both groups as $d_{\mathrm{JS,c}}$ does.

4 Experiments

4.1 Experimental Setup

Datasets. MedFairVLM is built from eight public medical imaging datasets spanning four modalities: chest X-ray (MIMIC-CXR (Johnson et al., 2019a), CheXpert+ (Chambon et al., 2024), PadChest-GR (Castro et al., 2025)), fundus photography (BRSET (Nakayama et al., 2024), Harvard-FairVLMed (Luo et al., 2024)), dermoscopy (HAM10000 (Tschandl et al., 2018), Fitzpatrick17k (Groh et al., 2021)), and abdominal CT (Merlin (Blankemeier et al., 2026)). Sensitive attributes are `Sex`, `Age`, `Race`, and `Skin type`, each binarized (Appendix D.1).

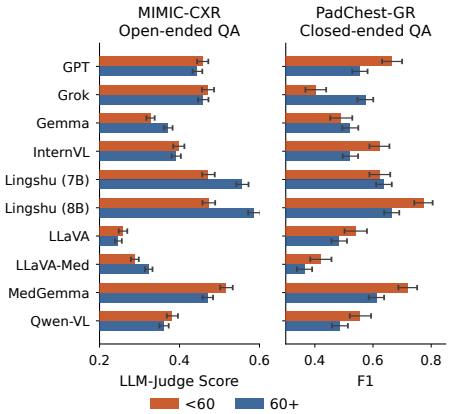

Figure 2: Zero-shot utility per `Age` group with 95% CIs, MIMIC-CXR open-ended QA (left) and PadChest-GR closed-ended QA (right). Most models are unfair, but the favored group differs across models.

Protocol. For fine-tuning, we pool the training samples of all tasks of a dataset, fine-tune each open-weight model on it, and evaluate every task; we also fine-tune with two fairness-enhancing methods, AI, which adds an attribute-invariance penalty on latent representations (Bhosale et al., 2026), and RW, which reweights the loss by group size (Kamiran & Calders, 2012). For distribution shift, we fine-tune on one dataset and evaluate on another of the same modality in both directions for two pairs: BRSET and FairVLMed, and MIMIC-CXR and CheXpert+ (Appendix D.4).

Models. We evaluate eight open-weight MLLMs in both zero-shot and fine-tuned settings: four general models, LLaVA-1.5-7B (Liu et al., 2024), Qwen2.5-VL-7B (Bai et al., 2025), InternVL3-8B (Zhu et al., 2025), and Gemma-3-4B (Gemma Team, 2025), and four medical models, MedGemma-4B (Sellergren et al., 2025), LLaVA-Med-7B (Li et al., 2023), Lingshu-7B, and Lingshu-I-8B (Xu et al., 2026). Two commercial models, GPT-4.1 (OpenAI, 2025) and Grok 4.20 (Non-Reasoning) (xAI, 2025), are evaluated zero-shot only (Appendix D.2).

Tasks and metrics. *Closed-ended QA* asks whether a finding is present (yes/no), with questions generated from each dataset's labels, and is scored by F1 to account for label skew. *Open-ended*

Dataset	Sex	Age	Race
CheXpert+	0.740	0.245	0.515
FairVLMed	0.343	<0.001	0.008
Merlin	0.465	0.011	0.938
MIMIC-CXR	0.095	0.076	0.059
PadChest-GR	0.007	0.088	N/A

(a) Zero-shot

Dataset	Sex	Age	Race
CheXpert+	0.219	0.804	0.004
FairVLMed	0.307	<0.001	<0.001
Merlin	0.004	0.002	0.059
MIMIC-CXR	0.008	<0.001	<0.001
PadChest-GR	<0.001	<0.001	N/A

(b) Fine-tuned

Table 1: Is the same group favored across models? Paired t-test p-values on the group-wise utility difference across models, open-ended QA. Shaded : $p < 0.05$; N/A: attribute unavailable.

QA asks a diagnosis-related question with a short free-text answer, built with GPT-5-mini from the datasets' reports, and is scored by an LLM judge that answers a checklist of binary questions on accuracy, detail, relevance, and helpfulness relative to the reference (Pereira et al., 2024; Zambrano Chaves et al., 2025). *Report generation* asks for a brief report of the findings and is scored with the GREEN score (Ostmeier et al., 2024) adapted to all modalities and judged by GPT-5-mini. Datasets with reports (the chest X-ray and CT datasets and FairVLMed) support all three tasks, whereas BRSET, HAM10000, and Fitzpatrick17k support closed-ended QA only. Utility is the task metric; unfairness is the absolute utility difference between the two groups of an attribute, i.e., F_M in Eq. (1) (Appendix D.3).

4.2 Results

We report the main findings here; complete results for every dataset, task, attribute, and model are in Appendix E.

Zero-shot MLLMs are unfair, but which group they favor is inconsistent. We first evaluate every model zero-shot and record its utility for each attribute group. Figure 2 shows two representative settings: most models show a significant gap, yet the favored group changes from model to model; on MIMIC-CXR open-ended QA, Gemma-3-4B and the Lingshu models favor patients aged 60+ while MedGemma-4B and Qwen2.5-VL-7B favor <60. Across the benchmark, every one of the ten models is significantly unfair (bootstrapping on the group-wise utility difference, 95% CI excludes zero, $N = 3{,}000$ resamples) in a large share of its (dataset, attribute, task) cases, from 36% to 57%, and the two commercial models are no exception (Appendix E.1). To quantify how much models agree on the favored group, we treat each model's group-wise utility difference as one paired observation and run a paired t-test for each dataset, task, and attribute. Table 1a shows that only 34% of cases exhibit a statistically significant performance difference between groups (Appendix E.2). Two factors likely explain the rest: each model has a different pretraining background that we do not control, so part of its disparity stems from pretraining data rather than from the evaluated dataset, and zero-shot utility is often low, so group differences are small and their direction close to random.

Task	FEMI	(i)	(ii)	(iii)	(iv)	(v)
Closed-ended QA ($n = 152$)	.29	.32	.28	.24	.33	.71
Open-ended QA ($n = 112$)	.40	.61	.36	.65	.61	.81
Report Generation ($n = 112$)	.17	.23	−.13	.16	.23	.57

Table 2: Spearman ρ between utility gap and FEMI, and between utility gap and each bias source, pooled across datasets, models, and attributes per task. Source (v) shows the strongest and most consistent correlation.

Fine-tuning makes unfairness consistent and widespread. To remove the pretraining confound and bring every model to a stronger operating point, we fine-tune each model on each dataset and re-evaluate every task. Under the same test, Table 1b shows significant, consistently directed unfairness across most datasets and attributes, and 74% of all cases now share a favored group across models (Appendix E.2). In-domain fine-tuning therefore does not remove group disparity; it aligns models on a common pattern that is set by the data, and this effect is broad rather than limited to one modality or question format. Among attributes, Age shows the most frequent group unfairness. This is expected, since age is a predictive factor for many diseases (Niccoli & Partridge, 2012). Fine-tuned models are therefore the setting in which we analyze the sources of bias next.

The sources of bias explain where unfairness comes from. We estimate FEMI and the five bias sources of Theorem 1 with the procedure of Section 3.3 and relate them to the utility gap. Figure 3

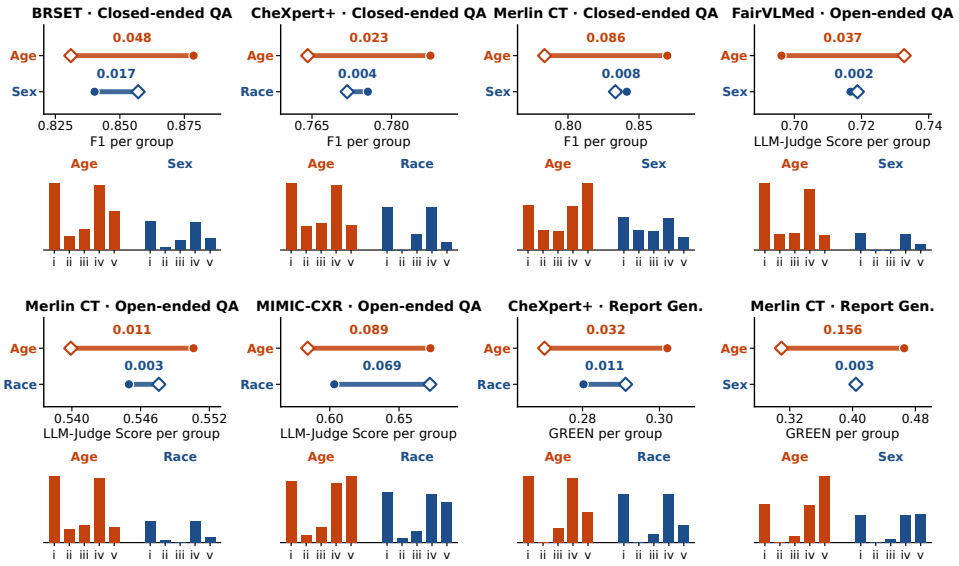

Figure 3: Utility gap and sources of bias after fine-tuning for the attribute with the larger (orange) and smaller (blue) gap per dataset and task. Top: per-group utility (● `Male`, `White`, `<60`; ◇ `Female`, `Non-white`, `60+`) and corresponding utility gap. Bottom: the five estimated bias sources (i)–(v). Larger bias sources go with the larger utility gap.

shows that, within each dataset and task, the sensitive attribute with larger bias sources has the larger utility gap; on Merlin open-ended QA, for instance, `Age` has both the larger utility gap and the larger image and image-given-query disparities, i.e., sources (i) and (iv) (Appendix E.3). Source (ii), the query-marginal disparity, is typically the smallest of the five and is near zero whenever queries are built from templates. Since this source measures how much the query distribution differs between groups, its small value indicates that our question construction introduces little between-group disparity. Table 2 quantifies this across all settings: FEMI and every bias source correlates positively with the gap in most cases, most strongly on open-ended QA, the setting for which our theory is designed, and source (v), the disparity in the reference response given the input, is the strongest and most consistent predictor across all three tasks. Table 8 shows the correlation with embeddings computed from BiomedCLIP (Zhang et al., 2023) in place of CLIP, revealing a consistent pattern and confirming that our observation is robust to the choice of encoder.

Fairness-enhancing fine-tuning does not help consistently. We compare fairness-enhancing fine-tuning checkpoints (AI and RW) with its own vanilla fine-tuned checkpoint (VA). Figure 4 shows the utility gap and sources of bias on open-ended QA for MedGemma, which retains strong utility after fairness-enhancing fine-tuning. Here, we estimate the bias sources as in Section 3.3, but use representations from a middle layer of the evaluated model rather than model-independent frozen embeddings. This isolates dataset effects on fairness, allowing the estimated bias sources to reflect fairness changes induced by fairness-enhanced fine-tuning relative to vanilla fine-tuning. On FairVLMed (`Sex`), both fairness methods reduce sources (i), (iii), and (iv) compared to VA, by learning more equitable representations or by upweighting minority-group samples, and unfairness falls. On CheXpert+ (`Age`), where the disparity is large and spread across several sources, neither method reduces them, and the larger utility drop of the disadvantaged group widens the gap. Across all settings, AI fails to improve fairness in 36% of cases and RW in 50% (Appendix E.4). Measuring the sources of bias thus reveals whether a method has addressed the cause of unfairness rather than only its symptom.

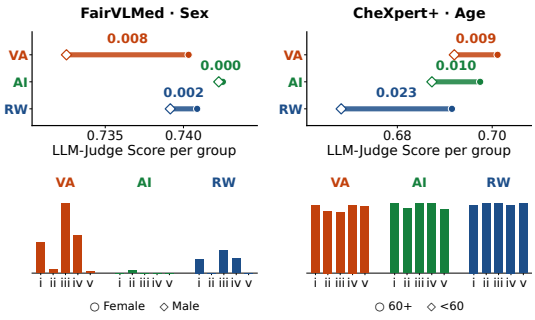

Figure 4: Utility gap and sources of bias for AI and RW versus vanilla fine-tuning (VA), MedGemma, open-ended QA. When a method reduces bias sources, unfairness (utility gap) falls.

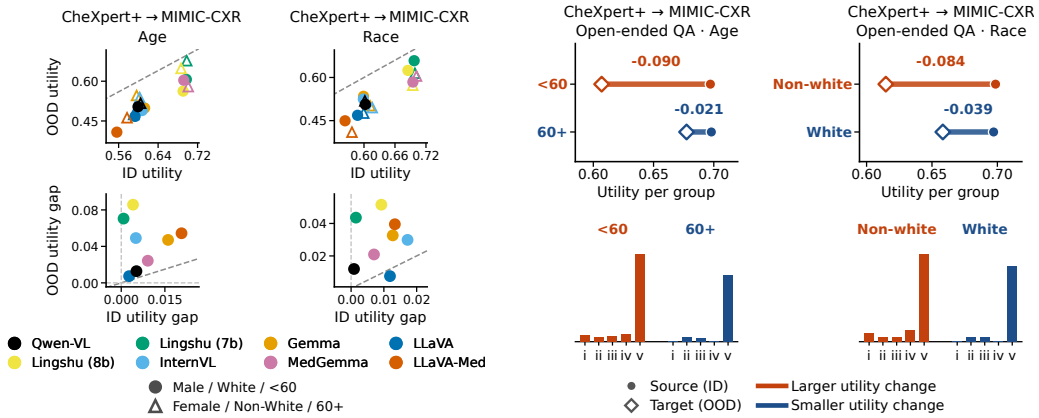

(a) ID vs. OOD utility (top) and gap (bottom)

(b) Utility change (top) and OOD sources (bottom)

Figure 5: CheXpert+ to MIMIC-CXR. (a) Utility drops for all group and model; the gap moves consistently per attribute. (b) Group whose OOD sources shift more suffers larger utility drop.

Distribution shift changes unfairness through uneven per-group shift. For each dataset pair and direction of distribution shift, we record each group's utility and the between-group utility gap (fairness), both in-distribution (ID), evaluated on the source dataset, and out-of-distribution (OOD), evaluated on the target dataset. We also estimate the five OOD sources for each group by comparing its source and target distributions (Appendix C.7). These sources are analogous to the between-group bias sources defined in Theorem 1, but instead characterize the distribution shift experienced by each group.

Figure 5 shows the CheXpert+ to MIMIC-CXR distribution shift direction. Utility drops OOD for every group and model (Figure 5a, top, all points below the diagonal), and the utility gap (bottom) changes consistently across models, though its direction depends on the attribute: for `Age` and `Race` almost every model becomes more unfair, whereas `Sex` is mixed, showing that shift affects attributes in different ways. According to Proposition 1, changes in fairness under distribution shift can be explained by shifts in per-group utility, which in turn can be attributed to the per-group OOD sources. Figure 5b illustrates this relationship concretely: `<60` undergoes a larger distribution shift than `60+`, particularly with respect to OOD source (v), resulting in a larger utility drop for `<60` and, consequently, a widening of the utility gap that was initially small on the source datasets. Table 3 shows that the EMI shift between source and target datasets predicts each group's utility shift. Consistent with our findings for bias sources, the OOD sources correlate most strongly with utility shift on open-ended QA.

Task	EMI shift	(i)	(ii)	(iii)	(iv)	(v)
Closed-ended QA ($n = 160$)	.30	.07	−.02	.01	.06	−.00
Open-ended QA ($n = 96$)	.44	.26	−.00	.30	.26	−.04
Report gen. ($n = 96$)	.62	−.08	−.09	.17	.11	−.49

Table 3: Spearman ρ between per-group utility shift and EMI shift, and between utility shift and each OOD source, pooled across datasets, models, and groups per task. EMI shift shows the strongest and most consistent correlation.

5 Conclusion

We systematically investigate fairness in multimodal LLMs for medical imaging, introducing a theoretical framework that defines fairness for open-ended generation, decomposes unfairness into five bias sources with estimators to quantify them, and analyzes fairness under distribution shift. Our benchmark, MedFairVLM, includes ten open-weight and commercial MLLMs, two fairness-enhancing methods, and eight public datasets spanning four imaging modalities, four sensitive attributes, three clinical tasks, and three deployment scenarios. Extensive experiments reveal prevalent unfairness across models and settings, links between bias sources and model unfairness after fine-tuning, inconsistent effectiveness of existing fairness methods, and the role of uneven per-group shifts under distribution shift. We hope our fine-grained analysis encourages more rigorous fairness evaluation and the development of new fairness algorithms for medical MLLMs.

ETHICS STATEMENT

This work studies whether multimodal LLMs treat demographic groups equally in medical imaging. All experiments use eight publicly available, de-identified datasets; we collected no new data from human subjects. Each dataset was obtained under its own access terms, including credentialed access on PhysioNet, data use agreements with Stanford AIMI and BIMCV, and Creative Commons non-commercial licenses, and was used for research only, as documented in Appendix D.1. Where model responses or reference text were processed by commercial APIs, this was done in accordance with the data use agreements of the corresponding datasets. Sensitive attributes are taken as recorded by each dataset and binarized (for example, `White` versus `Non-white` and lighter versus darker skin types) to obtain groups large enough for reliable estimation; this simplification cannot represent intersectional, non-binary, or finer-grained identities, and our group-level findings should not be read as statements about individuals. Our results show that current MLLMs, including commercial ones, are unfair across demographic groups in clinical tasks, and none of the evaluated models or fine-tuned checkpoints should be used for clinical decision making. We also note that LLM-as-a-judge scores may carry biases of the judge model itself; we mitigate this with a checklist-based protocol and complement it with the judge-independent EMI proxy, but the risk cannot be fully excluded. We release the benchmark construction code and evaluation pipeline so that fairness can be audited before deployment, and we see no direct path by which this work could be misused to harm patients. The authors declare no competing interests.

REPRODUCIBILITY STATEMENT

We have taken several steps to make our results reproducible. The problem setting and all notation are defined in Section 2, and complete proofs of Theorem 1 and Proposition 1, together with the supporting lemmas, are given in Appendix B. Appendix C specifies every estimator used to compute EMI, FEMI, and the five sources of bias, including the frozen encoders, the kernel and random-feature construction, the unbiased MMD and split-half CMMD estimators, and the normalization of reported values. Appendix D.1 describes each dataset, how its questions, answers, and reports were constructed, how sensitive attributes were binarized, the train, validation, and test splits, and the access terms and licenses. Appendix D.2 lists the exact model versions, Appendix D.3 gives the verbatim prompts used to generate open-ended questions and to score responses with the LLM judge and the adapted GREEN score, and Appendix D.4 reports all fine-tuning hyperparameters, which are shared across models and datasets, as well as the inference and hardware setup. Appendix E contains the complete results behind every figure and table in the main text, with bootstrap confidence intervals and statistical tests. Our code for benchmark construction, fine-tuning, evaluation, and estimation of the sources of bias is provided as anonymized supplementary material and will be released publicly upon publication; the datasets themselves must be obtained from their original sources under the terms described above.

AI USE STATEMENT

In this work, we used generative AI tools to generate synthetic data and to support data analysis: GPT-5-mini generated the open-ended question–answer pairs of our benchmark from the reports provided by each dataset, and GPT-5-mini served as the LLM judge that scores open-ended answers and generated reports, in both cases with the prompts given verbatim in Appendix D.3. Generative AI models are also the subject of our study: GPT-4.1 and Grok 4.20 are among the ten evaluated MLLMs. We have not used generative AI tools to develop the theoretical framework, formulate mathematical claims, provide ingredients for or write proofs, propose or refine hypotheses, design the research methodology or experiments, implement the methods, clean or reformat datasets beyond the question generation described above, or interpret the results. Assisting with translation and supporting qualitative or thematic data analysis are not applicable to this work. Additionally, we used generative AI tools to edit parts of the paper to improve readability, to identify and format references, to create and edit software code, and to create the overview figure. We have reviewed all AI-assisted work. Every generated question–answer pair passed automated consistency checks against the source report and a manual review of samples from each dataset; every reference was checked against the publisher or arXiv record before inclusion; all AI-assisted text, code, and figures

were verified by the authors against the underlying results. We take responsibility for the final content of this work, including text, claims, and artifacts produced with the aid of generative AI.

REFERENCES

Seongsu Bae, Daeun Kyung, Jaehee Ryu, Eunbyeol Cho, Gyubok Lee, Sunjun Kweon, Jungwoo Oh, Lei Ji, Eric Chang, Tackeun Kim, and Edward Choi. MIMIC-Ext-MIMIC-CXR-VQA: A complex, diverse, and large-scale visual question answering dataset for chest x-ray images (version 1.0.0). PhysioNet, 2024.

Shuai Bai, Keqin Chen, Xuejing Liu, Jialin Wang, Wenbin Ge, Sibo Song, Kai Dang, Peng Wang, Shijie Wang, Jun Tang, et al. Qwen2.5-VL technical report. *arXiv preprint arXiv:2502.13923*, 2025.

Mahesh Bhosale, Abdul Wasi, Shantam Srivastava, Shifa Latif, Tianyu Luan, Mingchen Gao, David Doermann, and Xuan Gong. FairLLaVA: Fairness-aware parameter-efficient fine-tuning for large vision-language assistants. In *Proceedings of the IEEE/CVF Conference on Computer Vision and Pattern Recognition (CVPR)*, 2026.

Louis Blankemeier, Ashwin Kumar, Joseph Paul Cohen, et al. Merlin: A computed tomography vision–language foundation model and dataset. *Nature*, 652(8112):1318–1328, 2026.

Alexander Brown, Nenad Tomasev, Jan Freyberg, Yuan Liu, Alan Karthikesalingam, and Jessica Schrouff. Detecting shortcut learning for fair medical AI using shortcut testing. *Nature Communications*, 14:4314, 2023.

Aurelia Bustos, Antonio Pertusa, Jose-Maria Salinas, and Maria de la Iglesia-Vayá. PadChest: A large chest x-ray image dataset with multi-label annotated reports. *Medical Image Analysis*, 66: 101797, 2020.

Daniel C. Castro, Aurelia Bustos, Shruthi Bannur, Stephanie L. Hyland, Kenza Bouzid, Maria Teodora Wetscherek, Maria Dolores Sánchez-Valverde, Lara Jaques-Pérez, Lourdes Pérez-Rodríguez, Kenji Takeda, José María Salinas, Javier Alvarez-Valle, Joaquín Galant Herrero, and Antonio Pertusa. PadChest-GR: A bilingual chest x-ray dataset for grounded radiology report generation. *NEJM AI*, 2(7), 2025.

Pierre Chambon, Jean-Benoit Delbrouck, Thomas Sounack, Shih-Cheng Huang, Zhihong Chen, Maya Varma, Steven QH Truong, Chu The Chuong, and Curtis P. Langlotz. CheXpert Plus: Augmenting a large chest x-ray dataset with text radiology reports, patient demographics and additional image formats. *arXiv preprint arXiv:2405.19538*, 2024.

Richard J. Chen, Judy J. Wang, Drew F. K. Williamson, Tiffany Y. Chen, Jana Lipkova, Ming Y. Lu, Sharifa Sahai, and Faisal Mahmood. Algorithmic fairness in artificial intelligence for medicine and healthcare. *Nature Biomedical Engineering*, 7(6):719–742, 2023.

Xiuying Chen, Tairan Wang, Juexiao Zhou, Zirui Song, Xin Gao, and Xiangliang Zhang. Evaluating and mitigating bias in AI-based medical text generation. *Nature Computational Science*, 5:388–396, 2025.

Harry Cheng, Yangyang Guo, Qingpei Guo, Ming Yang, Tian Gan, Weili Guan, and Liqiang Nie. Social debiasing for fair multi-modal LLMs. In *Proceedings of the IEEE/CVF International Conference on Computer Vision (ICCV)*, pp. 1740–1750, 2025.

Pengyu Cheng, Weituo Hao, Shuyang Dai, Jiachang Liu, Zhe Gan, and Lawrence Carin. CLUB: A contrastive log-ratio upper bound of mutual information. In *International Conference on Machine Learning (ICML)*, volume 119 of *Proceedings of Machine Learning Research*, pp. 1779–1788, 2020.

Victor Chernozhukov, Denis Chetverikov, Mert Demirer, Esther Duflo, Christian Hansen, Whitney Newey, and James Robins. Double/debiased machine learning for treatment and structural parameters. *The Econometrics Journal*, 21(1):C1–C68, 2018.

Alexis Conneau, Kartikay Khandelwal, Naman Goyal, Vishrav Chaudhary, Guillaume Wenzek, Francisco Guzmán, Edouard Grave, Myle Ott, Luke Zettlemoyer, and Veselin Stoyanov. Unsupervised cross-lingual representation learning at scale. In *Proceedings of the 58th Annual Meeting of the Association for Computational Linguistics*, pp. 8440–8451, 2020.

Corinna Cortes and Mehryar Mohri. Domain adaptation and sample bias correction theory and algorithm for regression. *Theoretical Computer Science*, 519:103–126, 2014.

Roxana Daneshjou, Kailas Vodrahalli, Roberto A. Novoa, Melissa Jenkins, Weixin Liang, Veronica Rotemberg, Justin Ko, Susan M. Swetter, Elizabeth E. Bailey, Olivier Gevaert, et al. Disparities in dermatology AI performance on a diverse, curated clinical image set. *Science Advances*, 8(32): eabq6147, 2022.

Jwala Dhamala, Tony Sun, Varun Kumar, Satyapriya Krishna, Yada Pruksachatkun, Kai-Wei Chang, and Rahul Gupta. BOLD: Dataset and metrics for measuring biases in open-ended language generation. In *Proceedings of the ACM Conference on Fairness, Accountability, and Transparency (FAccT)*, 2021.

Raman Dutt, Ondrej Bohdal, Sotirios A. Tsaftaris, and Timothy Hospedales. FairTune: Optimizing parameter efficient fine tuning for fairness in medical image analysis. In *International Conference on Learning Representations (ICLR)*, 2024.

Dominik Maria Endres and Johannes E. Schindelin. A new metric for probability distributions. *IEEE Transactions on Information Theory*, 49(7):1858–1860, 2003.

Kenji Fukumizu, Le Song, and Arthur Gretton. Kernel Bayes' rule: Bayesian inference with positive definite kernels. *Journal of Machine Learning Research*, 14:3753–3783, 2013.

Isabel O. Gallegos, Ryan A. Rossi, Joe Barrow, Md Mehrab Tanjim, Sungchul Kim, Franck Dernoncourt, Tong Yu, Ruiyi Zhang, and Nesreen K. Ahmed. Bias and fairness in large language models: A survey. *Computational Linguistics*, 50(3):1097–1179, 2024.

Gemma Team. Gemma 3 technical report. *arXiv preprint arXiv:2503.19786*, 2025.

Judy Wawira Gichoya, Imon Banerjee, Ananth Reddy Bhimireddy, John L. Burns, Leo Anthony Celi, Li-Ching Chen, Ramon Correa, Natalie Dullerud, Marzyeh Ghassemi, Shih-Cheng Huang, et al. AI recognition of patient race in medical imaging: A modelling study. *The Lancet Digital Health*, 4(6):e406–e414, 2022.

Ben Glocker, Charles Jones, Mélanie Bernhardt, and Stefan Winzeck. Algorithmic encoding of protected characteristics in chest x-ray disease detection models. *eBioMedicine*, 89:104467, 2023a.

Ben Glocker, Charles Jones, Mélanie Roschewitz, and Stefan Winzeck. Risk of bias in chest radiography deep learning foundation models. *Radiology: Artificial Intelligence*, 5(6):e230060, 2023b.

Arthur Gretton, Karsten M. Borgwardt, Malte J. Rasch, Bernhard Schölkopf, and Alexander Smola. A kernel two-sample test. *Journal of Machine Learning Research*, 13:723–773, 2012.

Matthew Groh, Caleb Harris, Luis Soenksen, Felix Lau, Rachel Han, Aerin Kim, Arash Koochek, and Omar Badri. Evaluating deep neural networks trained on clinical images in dermatology with the Fitzpatrick 17k dataset. In *Proceedings of the IEEE/CVF Conference on Computer Vision and Pattern Recognition Workshops (CVPRW)*, pp. 1820–1828, 2021.

Steffen Grünewälder, Guy Lever, Luca Baldassarre, Sam Patterson, Arthur Gretton, and Massimilano Pontil. Conditional mean embeddings as regressors-supplementary. *arXiv preprint arXiv:1205.4656*, 2012.

Siobhan Mackenzie Hall, Fernanda Gonçalves Abrantes, Hanwen Zhu, Grace A. Sodunke, Aleksandar Shtedritski, and Hannah Rose Kirk. VisoGender: A dataset for benchmarking gender bias in image-text pronoun resolution. In *Advances in Neural Information Processing Systems (NeurIPS), Datasets and Benchmarks Track*, 2023.

Moritz Hardt, Eric Price, and Nathan Srebro. Equality of opportunity in supervised learning. In *Advances in Neural Information Processing Systems (NeurIPS)*, 2016.

Iryna Hartsock and Ghulam Rasool. Vision-language models for medical report generation and visual question answering: A review. *Frontiers in Artificial Intelligence*, 7:1430984, 2024.

Phillip Howard, Avinash Madasu, Tiep Le, Gustavo Lujan Moreno, Anahita Bhiwandiwalla, and Vasudev Lal. SocialCounterfactuals: Probing and mitigating intersectional social biases in vision-language models with counterfactual examples. In *Proceedings of the IEEE/CVF Conference on Computer Vision and Pattern Recognition (CVPR)*, pp. 11975–11985, 2024.

Edward J. Hu, Yelong Shen, Phillip Wallis, Zeyuan Allen-Zhu, Yuanzhi Li, Shean Wang, Lu Wang, and Weizhu Chen. LoRA: Low-rank adaptation of large language models. In *International Conference on Learning Representations (ICLR)*, 2022.

Ruinan Jin, Zikang Xu, Yuan Zhong, Qingsong Yao, Qi Dou, S. Kevin Zhou, and Xiaoxiao Li. FairMedFM: Fairness benchmarking for medical imaging foundation models. In *Advances in Neural Information Processing Systems (NeurIPS), Datasets and Benchmarks Track*, 2024.

Alistair E. W. Johnson, Tom J. Pollard, Seth J. Berkowitz, Nathaniel R. Greenbaum, Matthew P. Lungren, Chih-ying Deng, Roger G. Mark, and Steven Horng. MIMIC-CXR, a de-identified publicly available database of chest radiographs with free-text reports. *Scientific Data*, 6:317, 2019a.

Alistair E. W. Johnson, Tom J. Pollard, Nathaniel R. Greenbaum, Matthew P. Lungren, Chih-ying Deng, Yifan Peng, Zhiyong Lu, Roger G. Mark, Seth J. Berkowitz, and Steven Horng. MIMIC-CXR-JPG, a large publicly available database of labeled chest radiographs. *arXiv preprint arXiv:1901.07042*, 2019b.

Alistair E. W. Johnson, Lucas Bulgarelli, Lu Shen, Alvin Gayles, Ayad Shammout, Steven Horng, Tom J. Pollard, Sicheng Hao, Benjamin Moody, Brian Gow, Li-wei H. Lehman, Leo A. Celi, and Roger G. Mark. MIMIC-IV, a freely accessible electronic health record dataset. *Scientific Data*, 10:1, 2023.

Charles Jones, Daniel C. Castro, Fabio De Sousa Ribeiro, Ozan Oktay, Melissa McCradden, and Ben Glocker. A causal perspective on dataset bias in machine learning for medical imaging. *Nature Machine Intelligence*, 6(2):138–146, 2024.

Faisal Kamiran and Toon Calders. Data preprocessing techniques for classification without discrimination. *Knowledge and Information Systems*, 33(1):1–33, 2012.

Muhammad Osama Khan, Muhammad Muneeb Afzal, Shujaat Mirza, and Yi Fang. How fair are medical imaging foundation models? In *Machine Learning for Health (ML4H)*, volume 225 of *Proceedings of Machine Learning Research*, pp. 217–231, 2023.

Ira Ktena, Olivia Wiles, Isabela Albuquerque, Sylvestre-Alvise Rebuffi, Ryutaro Tanno, Abhijit Guha Roy, Shekoofeh Azizi, Danielle Belgrave, Pushmeet Kohli, Taylan Cemgil, Alan Karthikesalingam, and Sven Gowal. Generative models improve fairness of medical classifiers under distribution shifts. *Nature Medicine*, 30(4):1166–1173, 2024.

Agostina J. Larrazabal, Nicolás Nieto, Victoria Peterson, Diego H. Milone, and Enzo Ferrante. Gender imbalance in medical imaging datasets produces biased classifiers for computer-aided diagnosis. *Proceedings of the National Academy of Sciences*, 117(23):12592–12594, 2020.

Chunyuan Li, Cliff Wong, Sheng Zhang, Naoto Usuyama, Haotian Liu, Jianwei Yang, Tristan Naumann, Hoifung Poon, and Jianfeng Gao. LLaVA-Med: Training a large language-and-vision assistant for biomedicine in one day. In *Advances in Neural Information Processing Systems (NeurIPS), Datasets and Benchmarks Track*, 2023.

Percy Liang, Rishi Bommasani, Tony Lee, Dimitris Tsipras, Dilara Soylu, Michihiro Yasunaga, Yian Zhang, Deepak Narayanan, Yuhuai Wu, Ananya Kumar, et al. Holistic evaluation of language models. *Transactions on Machine Learning Research*, 2023.

Jianhua Lin. Divergence measures based on the Shannon entropy. *IEEE Transactions on Information Theory*, 37(1):145–151, 1991.

Haotian Liu, Chunyuan Li, Qingyang Wu, and Yong Jae Lee. Visual instruction tuning. In *Advances in Neural Information Processing Systems (NeurIPS)*, 2023.

Haotian Liu, Chunyuan Li, Yuheng Li, and Yong Jae Lee. Improved baselines with visual instruction tuning. In *Proceedings of the IEEE/CVF Conference on Computer Vision and Pattern Recognition (CVPR)*, pp. 26296–26306, 2024.

Yan Luo, Min Shi, Muhammad Osama Khan, Muhammad Muneeb Afzal, Hao Huang, Shuaihang Yuan, Yu Tian, Luo Song, Ava Kouhana, Tobias Elze, Yi Fang, and Mengyu Wang. FairCLIP: Harnessing fairness in vision-language learning. In *Proceedings of the IEEE/CVF Conference on Computer Vision and Pattern Recognition (CVPR)*, pp. 12289–12301, 2024.

Yishay Mansour, Mehryar Mohri, and Afshin Rostamizadeh. Domain adaptation: Learning bounds and algorithms. In *Conference on Learning Theory (COLT)*, 2009.

Ričards Marcinkevičs, Ece Ozkan, and Julia E. Vogt. Debiasing deep chest x-ray classifiers using intra- and post-processing methods. In *Proceedings of the Machine Learning for Healthcare Conference (MLHC)*, volume 182 of *Proceedings of Machine Learning Research*, pp. 504–536, 2022.

Rafid Mehda, Ramisa Anjum Oishi, Tamzid Tanvi Alam, Md Kishor Morol, and Liew Tze Hui. Cross-modal bias in medical vision-language models: A pipeline-aware framework for mechanisms, evaluation, and mitigation. *Frontiers in Digital Health*, 8:1904053, 2026.

Peter Moskvichev, Siu Lun Chau, and Dino Sejdinovic. Measuring differences between conditional distributions using kernel embeddings. *arXiv preprint arXiv:2605.02260*, 2026.

Luis Filipe Nakayama, David Restrepo, João Matos, Lucas Zago Ribeiro, Fernando Korn Malerbi, Leo Anthony Celi, and Caio Saito Regatieri. BRSET: A brazilian multilabel ophthalmological dataset of retina fundus photos. *PLOS Digital Health*, 3(7):e0000454, 2024.

A. Tuan Nguyen, Toan Tran, Yarin Gal, Philip Torr, and Atılım Güneş Baydin. KL guided domain adaptation. In *International Conference on Learning Representations (ICLR)*, 2022.

Teresa Niccoli and Linda Partridge. Ageing as a risk factor for disease. *Current Biology*, 22(17): R741–R752, 2012.

Ziad Obermeyer, Brian Powers, Christine Vogeli, and Sendhil Mullainathan. Dissecting racial bias in an algorithm used to manage the health of populations. *Science*, 366(6464):447–453, 2019.

Changdae Oh, Zhen Fang, Shawn Im, Xuefeng Du, and Yixuan Li. Understanding multimodal LLMs under distribution shifts: An information-theoretic approach. In *International Conference on Machine Learning (ICML)*, volume 267 of *Proceedings of Machine Learning Research*, 2025.

Kingsley Okoye and Samira Hosseini. Wilcoxon statistics in r: Signed-rank test and rank-sum test. In *R Programming: Statistical data analysis in research*, pp. 279–303. Springer, 2024.

Mahmud Omar, Shelly Soffer, Reem Agbareia, Nicola Luigi Bragazzi, Donald U. Apakama, Carol R. Horowitz, Alexander W. Charney, Robert Freeman, Benjamin Kummer, Benjamin S. Glicksberg, Girish N. Nadkarni, and Eyal Klang. Sociodemographic biases in medical decision making by large language models. *Nature Medicine*, 31:1873–1881, 2025.

Jesutofunmi A. Omiye, Jenna C. Lester, Simon Spichak, Veronica Rotemberg, and Roxana Daneshjou. Large language models propagate race-based medicine. *npj Digital Medicine*, 6: 195, 2023.

OpenAI. GPT-4 technical report. *arXiv preprint arXiv:2303.08774*, 2023.

OpenAI. Introducing GPT-4.1 in the API. `https://openai.com/index/gpt-4-1/`, 2025.

Sophie Ostmeier, Justin Xu, Zhihong Chen, Maya Varma, Louis Blankemeier, Christian Bluethgen, Arne Edward Michalson, Michael Moseley, Curtis Langlotz, Akshay S. Chaudhari, and Jean-Benoit Delbrouck. GREEN: Generative radiology report evaluation and error notation. In *Findings of the Association for Computational Linguistics: EMNLP 2024*, pp. 374–390, 2024.

Junhyung Park and Krikamol Muandet. A measure-theoretic approach to kernel conditional mean embeddings. In *Advances in Neural Information Processing Systems (NeurIPS)*, 2020.

Junhyung Park, Uri Shalit, Bernhard Schölkopf, and Krikamol Muandet. Conditional distributional treatment effect with kernel conditional mean embeddings and u-statistic regression. In *International Conference on Machine Learning (ICML)*, volume 139 of *Proceedings of Machine Learning Research*, pp. 8401–8412, 2021.

Alicia Parrish, Angelica Chen, Nikita Nangia, Vishakh Padmakumar, Jason Phang, Jana Thompson, Phu Mon Htut, and Samuel R. Bowman. BBQ: A hand-built bias benchmark for question answering. In *Findings of the Association for Computational Linguistics: ACL 2022*, pp. 2086–2105, 2022.

Jayr Pereira, Andre Assumpcao, and Roberto Lotufo. Check-Eval: A checklist-based approach for evaluating text quality. *arXiv preprint arXiv:2407.14467*, 2024.

Stephen R. Pfohl, Heather Cole-Lewis, Rory Sayres, Darlene Neal, Mercy Asiedu, Awa Dieng, Nenad Tomasev, Qazi Mamunur Rashid, Shekoofeh Azizi, Negar Rostamzadeh, et al. A toolbox for surfacing health equity harms and biases in large language models. *Nature Medicine*, 30(12): 3590–3600, 2024.

Thai-Hoang Pham, Xueru Zhang, and Ping Zhang. Non-stationary domain generalization: Theory and algorithm. In *Uncertainty in Artificial Intelligence (UAI)*, volume 244 of *Proceedings of Machine Learning Research*, pp. 2902–2927, 2024.

Thai-Hoang Pham, Jiayuan Chen, Seungyeon Lee, Yuanlong Wang, Sayoko Moroi, Xueru Zhang, and Ping Zhang. The boundaries of fair AI in medical image prognosis: A causal perspective. In *Advances in Neural Information Processing Systems (NeurIPS)*, volume 38, pp. 147872–147930, 2025a.

Thai-Hoang Pham, Yuanlong Wang, Changchang Yin, Xueru Zhang, and Ping Zhang. Open-set heterogeneous domain adaptation: Theoretical analysis and algorithm. In *Proceedings of the AAAI Conference on Artificial Intelligence*, volume 39, pp. 19895–19903, 2025b.

Esther Puyol-Antón, Bram Ruijsink, Stefan K. Piechnik, Stefan Neubauer, Steffen E. Petersen, Reza Razavi, and Andrew P. King. Fairness in cardiac MR image analysis: An investigation of bias due to data imbalance in deep learning based segmentation. In *Medical Image Computing and Computer Assisted Intervention (MICCAI)*, pp. 413–423, 2021.

Alec Radford, Jong Wook Kim, Chris Hallacy, Aditya Ramesh, Gabriel Goh, Sandhini Agarwal, Girish Sastry, Amanda Askell, Pam Mishkin, Jack Clark, Gretchen Krueger, and Ilya Sutskever. Learning transferable visual models from natural language supervision. In *International Conference on Machine Learning (ICML)*, volume 139 of *Proceedings of Machine Learning Research*, pp. 8748–8763, 2021.

Ali Rahimi and Benjamin Recht. Random features for large-scale kernel machines. In *Advances in Neural Information Processing Systems (NeurIPS)*, 2007.

Yong Ren, Jialian Li, Yucen Luo, and Jun Zhu. Conditional generative moment-matching networks. In *Advances in Neural Information Processing Systems (NeurIPS)*, 2016.

Khaled Saab, Tao Tu, Wei-Hung Weng, Ryutaro Tanno, David Stutz, Ellery Wulczyn, Fan Zhang, Tim Strother, Chunjong Park, Elahe Vedadi, et al. Capabilities of Gemini models in medicine. *arXiv preprint arXiv:2404.18416*, 2024.

Andrew Sellergren, Sahar Kazemzadeh, Tiam Jaroensri, Atilla Kiraly, Madeleine Traverse, Timo Kohlberger, Shawn Xu, Fayaz Jamil, Cían Hughes, Charles Lau, et al. MedGemma technical report. *arXiv preprint arXiv:2507.05201*, 2025.

Laleh Seyyed-Kalantari, Guanxiong Liu, Matthew McDermott, Irene Y. Chen, and Marzyeh Ghassemi. CheXclusion: Fairness gaps in deep chest x-ray classifiers. In *Pacific Symposium on Biocomputing*, volume 26, pp. 232–243, 2021a.

Laleh Seyyed-Kalantari, Haoran Zhang, Matthew B. A. McDermott, Irene Y. Chen, and Marzyeh Ghassemi. Underdiagnosis bias of artificial intelligence algorithms applied to chest radiographs in under-served patient populations. *Nature Medicine*, 27(12):2176–2182, 2021b.

Emily Sheng, Kai-Wei Chang, Premkumar Natarajan, and Nanyun Peng. The woman worked as a babysitter: On biases in language generation. In *Proceedings of the 2019 Conference on Empirical Methods in Natural Language Processing and the 9th International Joint Conference on Natural Language Processing (EMNLP-IJCNLP)*, pp. 3407–3412, 2019.

Le Song, Jonathan Huang, Alex Smola, and Kenji Fukumizu. Hilbert space embeddings of conditional distributions with applications to dynamical systems. In *International Conference on Machine Learning (ICML)*, pp. 961–968, 2009.

Bharath K. Sriperumbudur, Arthur Gretton, Kenji Fukumizu, Bernhard Schölkopf, and Gert R. G. Lanckriet. Hilbert space embeddings and metrics on probability measures. *Journal of Machine Learning Research*, 11:1517–1561, 2010.

Vinith M. Suriyakumar, Anna Zink, Maia Hightower, Marzyeh Ghassemi, and Brett Beaulieu-Jones. Computational challenges arising in algorithmic fairness and health equity with generative AI. *Nature Computational Science*, 5(9):698–700, 2025.

Xuwei Tan, Ziyu Hu, and Xueru Zhang. Benchmarking bias mitigation toward fairness without harm from vision to LVLMs. In *International Conference on Learning Representations (ICLR)*, 2026.

Yu Tian, Min Shi, Yan Luo, Ava Kouhana, Tobias Elze, and Mengyu Wang. FairSeg: A large-scale medical image segmentation dataset for fairness learning using segment anything model with fair error-bound scaling. In *International Conference on Learning Representations (ICLR)*, 2024a.

Yu Tian, Congcong Wen, Min Shi, Muhammad Muneeb Afzal, Hao Huang, Muhammad Osama Khan, Yan Luo, Yi Fang, and Mengyu Wang. FairDomain: Achieving fairness in cross-domain medical image segmentation and classification. In *European Conference on Computer Vision (ECCV)*, 2024b.

Philipp Tschandl, Cliff Rosendahl, and Harald Kittler. The HAM10000 dataset, a large collection of multi-source dermatoscopic images of common pigmented skin lesions. *Scientific Data*, 5: 180161, 2018.

Tao Tu, Shekoofeh Azizi, Danny Driess, Mike Schaekermann, Mohamed Amin, Pi-Chuan Chang, Andrew Carroll, Charles Lau, Ryutaro Tanno, Ira Ktena, et al. Towards generalist biomedical AI. *NEJM AI*, 1(3):AIoa2300138, 2024.

Anurag Vaidya, Richard J. Chen, Drew F. K. Williamson, Andrew H. Song, Guillaume Jaume, Yuzhe Yang, Thomas Hartvigsen, Emma C. Dyer, Ming Y. Lu, Jana Lipkova, et al. Demographic bias in misdiagnosis by computational pathology models. *Nature Medicine*, 30:1174–1190, 2024.

Yixin Wan, George Pu, Jiao Sun, Aparna Garimella, Kai-Wei Chang, and Nanyun Peng. "Kelly is a warm person, Joseph is a role model": Gender biases in LLM-generated reference letters. In *Findings of the Association for Computational Linguistics: EMNLP 2023*, pp. 3730–3748, 2023.

Peiran Wang, Linjie Tong, Jiaxiang Wu, Jiaxiang Liu, and Zuozhu Liu. Fair-MoE: Medical fairness-oriented mixture of experts in vision-language models. In *Medical Image Computing and Computer Assisted Intervention (MICCAI)*, 2025.

Sibo Wang, Xiangkui Cao, Jie Zhang, Zheng Yuan, Shiguang Shan, Xilin Chen, and Wen Gao. VLBiasBench: A comprehensive benchmark for evaluating bias in large vision-language model. *IEEE Transactions on Pattern Analysis and Machine Intelligence*, 48(8), 2026. doi: 10.1109/TPAMI.2026.3683747.

Peiran Wu, Che Liu, Canyu Chen, Jun Li, Cosmin I. Bercea, and Rossella Arcucci. FMBench: Benchmarking fairness in multimodal large language models on medical tasks. *arXiv preprint arXiv:2410.01089*, 2024.

Xuyang Wu, Yuan Wang, Hsin-Tai Wu, Zhiqiang Tao, and Yi Fang. Evaluating fairness in large vision-language models across diverse demographic attributes and prompts. In *Findings of the Association for Computational Linguistics: EMNLP 2025*, pp. 22973–22991, 2025.

xAI. Grok 4 model card. `https://data.x.ai/2025-08-20-grok-4-model-card.pdf`, 2025.

Peng Xia, Ze Chen, Juanxi Tian, Yangrui Gong, Ruibo Hou, Yue Xu, Zhenbang Wu, Zhiyuan Fan, Yiyang Zhou, Kangyu Zhu, et al. CARES: A comprehensive benchmark of trustworthiness in medical vision language models. In *Advances in Neural Information Processing Systems (NeurIPS), Datasets and Benchmarks Track*, 2024.

Yisong Xiao, Aishan Liu, QianJia Cheng, Zhenfei Yin, Siyuan Liang, Jiapeng Li, Jing Shao, Xianglong Liu, and Dacheng Tao. GenderBias-VL: Benchmarking gender bias in vision language models via counterfactual probing. *International Journal of Computer Vision*, 133:8332–8355, 2025. doi: 10.1007/s11263-025-02556-7.

Sonnet Xu, Joseph D. Janizek, Yixing Jiang, and Roxana Daneshjou. BiasICL: In-context learning and demographic biases of vision language models. In *Medical Image Computing and Computer Assisted Intervention (MICCAI)*, 2025.

Weiwen Xu, Hou Pong Chan, Long Li, Mahani Aljunied, Ruifeng Yuan, et al. Lingshu: A generalist foundation model for unified multimodal medical understanding and reasoning. *IEEE Transactions on Pattern Analysis and Machine Intelligence*, 2026. to appear.

Zikang Xu, Jun Li, Qingsong Yao, Han Li, Mingyue Zhao, and S. Kevin Zhou. Addressing fairness issues in deep learning-based medical image analysis: A systematic review. *npj Digital Medicine*, 7:286, 2024.

Xinyu Yang, Junlin Han, Rishi Bommasani, Jinqi Luo, Wenjie Qu, Wangchunshu Zhou, Adel Bibi, Xiyao Wang, et al. Reliable and responsible foundation models: A comprehensive survey. *Transactions on Machine Learning Research*, 2025a.

Yuzhe Yang, Haoran Zhang, Judy W. Gichoya, Dina Katabi, and Marzyeh Ghassemi. The limits of fair medical imaging AI in real-world generalization. *Nature Medicine*, 30(10):2838–2848, 2024.

Yuzhe Yang, Yujia Liu, Xin Liu, Avanti Gulhane, Domenico Mastrodicasa, Wei Wu, Edward J. Wang, Dushyant Sahani, and Shwetak Patel. Demographic bias of expert-level vision-language foundation models in medical imaging. *Science Advances*, 11(13):eadq0305, 2025b.

Travis Zack, Eric Lehman, Mirac Suzgun, Jorge A. Rodriguez, Leo Anthony Celi, Judy Gichoya, Dan Jurafsky, Peter Szolovits, David W. Bates, Raja-Elie E. Abdulnour, Atul J. Butte, and Emily Alsentzer. Assessing the potential of GPT-4 to perpetuate racial and gender biases in health care: A model evaluation study. *The Lancet Digital Health*, 6(1):e12–e22, 2024.

Juan Manuel Zambrano Chaves, Shih-Cheng Huang, Yanbo Xu, Hanwen Xu, Naoto Usuyama, Sheng Zhang, Fei Wang, Yujia Xie, Mahmoud Khademi, Ziyi Yang, et al. A clinically accessible small multimodal radiology model and evaluation metric for chest x-ray findings. *Nature Communications*, 16:3108, 2025. doi: 10.1038/s41467-025-58344-x.

Haoran Zhang, Natalie Dullerud, Karsten Roth, Lauren Oakden-Rayner, Stephen Pfohl, and Marzyeh Ghassemi. Improving the fairness of chest x-ray classifiers. In *Proceedings of the Conference on Health, Inference, and Learning (CHIL)*, volume 174 of *Proceedings of Machine Learning Research*, pp. 204–233, 2022.

Sheng Zhang, Yanbo Xu, Naoto Usuyama, Hanwen Xu, Jaspreet Bagga, Robert Tinn, Sam Preston, Rajesh Rao, Mu Wei, Naveen Valluri, et al. Biomedclip: a multimodal biomedical foundation model pretrained from fifteen million scientific image-text pairs. *arXiv preprint arXiv:2303.00915*, 2023.

Lianmin Zheng, Wei-Lin Chiang, Ying Sheng, Siyuan Zhuang, Zhanghao Wu, Yonghao Zhuang, Zi Lin, Zhuohan Li, Dacheng Li, Eric P. Xing, Hao Zhang, Joseph E. Gonzalez, and Ion Stoica. Judging LLM-as-a-judge with MT-Bench and Chatbot Arena. In *Advances in Neural Information Processing Systems (NeurIPS), Datasets and Benchmarks Track*, 2023.

Jinguo Zhu, Weiyun Wang, Zhe Chen, Zhaoyang Liu, Shenglong Ye, Lixin Gu, Hao Tian, Yuchen Duan, Weijie Su, Jie Shao, et al. InternVL3: Exploring advanced training and test-time recipes for open-source multimodal models. *arXiv preprint arXiv:2504.10479*, 2025.

Yongshuo Zong, Yongxin Yang, and Timothy Hospedales. MEDFAIR: Benchmarking fairness for medical imaging. In *International Conference on Learning Representations (ICLR)*, 2023.

APPENDIX CONTENTS

A Extended Related Work . . . 20
A.1 Fairness in LLMs and Multimodal LLMs . . . 20
A.2 Fairness in Medical Imaging . . . 20
A.3 Evaluating Open-Ended Generation . . . 21
B Additional Lemmas and Proofs . . . 22
B.1 Lemmas . . . 22
B.2 EMI transfer inequality . . . 24
B.3 Proof of Theorem 1 . . . 25
B.4 Proof of Proposition 1 . . . 26
C Method Details . . . 26
C.1 Evaluation units and frozen embeddings . . . 26
C.2 Group-wise EMI and FEMI . . . 27
C.3 Kernel and random Fourier features . . . 27
C.4 Marginal sources (i) and (ii) . . . 28
C.5 Conditional sources (iii) to (v) . . . 28
C.6 Normalization and reported sources . . . 29
C.7 Use under distribution shift . . . 30
D Experiment Details . . . 30
D.1 Datasets . . . 30
D.2 Models . . . 33
D.3 Tasks and metrics . . . 33
D.4 Implementation details . . . 36
E Additional Results . . . 36
E.1 Fairness in zero-shot settings . . . 36
E.2 Fairness in fine-tuned settings . . . 44
E.3 Bias sources and fairness . . . 52
E.4 Fairness-mitigation methods . . . 55
E.5 Distribution-shift and fairness . . . 57
E.6 OOD source and fairness . . . 60

A Extended Related Work

A.1 Fairness in LLMs and Multimodal LLMs

Fairness in LLMs. Group fairness asks whether a model performs equally well for populations defined by a sensitive attribute (Hardt et al., 2016). For LLMs, this question was first posed with task-based benchmarks: BBQ (Parrish et al., 2022) compares question-answering accuracy across nine social dimensions, BOLD (Dhamala et al., 2021) scores open-ended continuations per demographic group with sentiment, regard (Sheng et al., 2019), toxicity, and psycholinguistic norms, and HELM (Liang et al., 2023) treats fairness as one of several evaluation axes by testing whether performance is invariant to demographic perturbations of the prompt. For free-text outputs, Wan et al. (2023) show that counterfactual prompts differing only in a name or pronoun elicit systematically different reference letters, and Gallegos et al. (2024) survey the resulting fairness metrics, which fall into counterfactual, lexicon-, classifier-, and distribution-based families and formalize the desiderata a fairness notion for generated text should satisfy. All of these methods rely on demographics that are stated in the prompt or salient in the output, which is not the case for medical images.

Fairness of LLMs in healthcare. Applied to medicine, the same comparisons reveal group disparities in clinical recommendations. Omiye et al. (2023) find that commercial LLMs reproduce debunked race-based medical claims; Zack et al. (2024) show that GPT-4 changes differential diagnoses, treatment plans, and subjective patient assessments with race and gender; and Omar et al. (2025) evaluate nine LLMs on over one million emergency-department outputs and find that cases labeled as Black, unhoused, or LGBTQIA+ are directed more often to urgent care, invasive interventions, or mental-health evaluations. Chen et al. (2025) extend these findings to medical text generation, documenting quality disparities across race, sex, and age and proposing an optimization-based mitigation. On the evaluation side, Pfohl et al. (2024) introduce human-rated rubrics and adversarial datasets for surfacing equity harms, and Suriyakumar et al. (2025) argue that generative outputs, which lack a single ground truth and a decision score, require new fairness definitions rather than the reuse of classification metrics. Our fairness criterion, a group disparity in judge scores with EMI as its theoretical proxy, is one answer to that call.

Fairness in vision–language models and MLLMs. Group-level performance disparities in vision–language models have been measured across several tasks. VisoGender (Hall et al., 2023) compares pronoun-resolution accuracy by perceived gender, Wu et al. (2025) compare VQA accuracy across demographic attributes and prompt formulations, and large synthetic benchmarks such as SocialCounterfactuals (Howard et al., 2024), GenderBias-VL (Xiao et al., 2025), and VLBias-Bench (Wang et al., 2026) generate counterfactual images with diffusion models to compare model behavior across intersectional and occupational groups. Fairness-enhancing methods for MLLMs include counter-stereotype fine-tuning on counterfactual data (Cheng et al., 2025), and NH-Fair (Tan et al., 2026) standardizes the comparison of such methods across vision and vision–language models under fairness-without-harm criteria. These works concern natural images with explicit or visually salient demographics; none studies medical imaging, where the demographic signal is latent in the pixels and correctness is clinically defined, and none gives a theoretical account of where unfairness in multimodal generation originates.

A.2 Fairness in Medical Imaging

Classical task-specific models. Unequal algorithmic performance in healthcare was brought to broad attention by Obermeyer et al. (2019), and in medical imaging by a series of chest X-ray studies: CheXclusion (Seyyed-Kalantari et al., 2021a) documented true-positive-rate gaps across sex, age, race, and insurance type, Seyyed-Kalantari et al. (2021b) showed that classifiers systematically underdiagnose under-served and intersectional subgroups, and Larrazabal et al. (2020) showed that sex imbalance in training data degrades performance for the minority sex. Similar disparities have been reported in dermatology (Daneshjou et al., 2022), cardiac MR segmentation (Puyol-Antón et al., 2021), and computational pathology (Vaidya et al., 2024); see Chen et al. (2023) and Xu et al. (2024) for reviews of fairness in medical AI. Mechanistic work shows that models recover self-reported race and other protected attributes from images even when radiologists cannot (Gichoya et al., 2022; Glocker et al., 2023a), that shortcut learning explains only part of the observed disparity (Brown et al., 2023), and that distinct causal sources of disparity, in prevalence, presentation, and

annotation, call for distinct remedies (Jones et al., 2024). Our five sources of bias can be read as the analogue of this causal taxonomy for multimodal generation. Fairness-enhancing methods span pre-, in-, and post-processing (Zhang et al., 2022; Marcinkevičs et al., 2022; Ktena et al., 2024), yet systematic benchmarks find that no method consistently improves on empirical risk minimization, in diagnosis (Zong et al., 2023) as well as prognosis (Pham et al., 2025a), and Yang et al. (2024) show that removing demographic shortcuts in-distribution can worsen fairness under distribution shift. All of this work concerns predicting a label from a single image.

Vision foundation models. As pretraining scaled, fairness audits followed. Khan et al. (2023) find that foundation models pretrained on medical images are more accurate but less fair than those pretrained on natural images, and Glocker et al. (2023b) show that a chest radiography foundation model encodes sex and race in its embeddings, leading to disparate downstream performance. Yang et al. (2025b) evaluate zero-shot vision–language models such as CheXzero on five international chest X-ray datasets and find that they underdiagnose marginalized and intersectional groups more severely than board-certified radiologists. FairMedFM (Jin et al., 2024) benchmarks the fairness of twenty foundation models on seventeen datasets across classification and segmentation, and fairness-annotated datasets with matched fairness-enhancing methods have appeared for vision–language pretraining (Luo et al., 2024; Wang et al., 2025), segmentation (Tian et al., 2024a), cross-domain transfer (Tian et al., 2024b), and parameter-efficient fine-tuning (Dutt et al., 2024). These studies evaluate fixed embeddings or closed-set predictions and do not consider open-ended generation.

Multimodal LLMs. Fairness evaluation of medical MLLMs is recent and sparse. CARES (Xia et al., 2024) evaluates trustworthiness along five dimensions, one of which is fairness, and reports accuracy gaps by age, sex, and race on closed- and open-ended VQA across sixteen modalities, with fairness treated as one dimension among many. FMBench (Wu et al., 2024) is the first benchmark devoted to the fairness of MLLMs on medical tasks, evaluating eight open-source models on fundus VQA and report generation with lexical and LLM-based metrics and proposing a fairness-aware performance score, but it covers a single dataset and zero-shot inference only. BiasICL (Xu et al., 2025) shows that the demographic composition of in-context examples shifts subgroup performance in dermatology and chest X-ray tasks, and FairLLaVA (Bhosale et al., 2026) reduces report-generation disparities with a mutual-information regularizer during instruction tuning, extending equity-scaled metrics to generative outputs. Mehda et al. (2026) offer a qualitative, pipeline-level taxonomy of the mechanisms through which unfairness can arise in medical vision–language models. Relative to these works, MedFairVLM contributes a fairness criterion aligned with LLM-as-a-judge evaluation, a theoretical bound that decomposes unfairness into five model-independent sources together with estimators for each, and a benchmark that spans ten open-source and commercial MLLMs, four imaging modalities, four organs, three sensitive attributes, three tasks, and three deployment scenarios.

A.3 Evaluating Open-Ended Generation

Because open-ended responses admit many valid phrasings, lexical overlap metrics correlate poorly with clinical correctness, and the field has moved to model-based judges (Hartsock & Rasool, 2024). LLM-as-a-judge scoring (Zheng et al., 2023) uses a strong model to rate responses against a rubric or a reference, and radiology-specific variants such as GREEN (Ostmeier et al., 2024) and CheXprompt (Zambrano Chaves et al., 2025) count clinically significant errors in generated reports; FMBench (Wu et al., 2024) likewise pairs lexical metrics with clinician-verified LLM-based ones. Judge scores are black-box quantities without mathematical guarantees, which motivated Oh et al. (2025) to introduce effective mutual information (EMI) as an information-theoretic measure of query–response relevance, to prove that EMI is close to the judge-based relative preference score whenever the model approximates the data distribution, and to bound the EMI change under distribution shift by input and output discrepancies. We adopt EMI as the proxy through which our fairness criterion becomes analyzable, and our bound can be seen as transporting their shift analysis from the in-distribution versus out-of-distribution setting to the comparison between demographic groups.

B Additional Lemmas and Proofs

Setup. Throughout this appendix, P_{XY} and Q_{XY} denote two joint distributions of the pair (X, Y). In the proof of Theorem 1 they are instantiated as the distributions of two groups, $P_{XY}^{(a)}$ and $P_{XY}^{(a')}$. Both P_{XY} and Q_{XY} are evaluated under the same fixed model $P_{Y_\theta|X}$, which combines with each input distribution to form the joint distributions $P_{XY_\theta} := P_X\, P_{Y_\theta|X}$ and $Q_{XY_\theta} := Q_X\, P_{Y_\theta|X}$ over (X, Y_θ). We write P_{Y_θ} and Q_{Y_θ} for the marginals these assign to Y_θ, namely the distribution of the model's responses when its inputs are drawn from P_X and from Q_X, respectively. There is no "$Q_{Y_\theta|X}$", since the model itself is unchanged and the two response distributions differ only because the two input distributions do. Because the group superscript notation $\mathrm{EMI}^{(a)}(\theta)$ of Section 2 carries only one distribution, we make the distribution an explicit argument instead,

$$\mathrm{EMI}(P_{XY}; \theta) := I_{P_{XY_\theta}}(X; Y_\theta) - I_{P_{XY}}(X; Y),$$

which recovers the group-wise quantity as $\mathrm{EMI}^{(a)}(\theta) = \mathrm{EMI}(P_{XY}^{(a)}; \theta)$. The lemmas below bound how much $\mathrm{EMI}(P_{XY}; \theta)$ can change as the distribution moves from P_{XY} to Q_{XY}. Finally, V and U denote a generic pair of random variables, with V the conditioning variable, as in Section 3.3; the lemmas below instantiate them as $(V, U) = (X_v, X_t)$, (X_t, X_v), and (X, Y).

Distance between conditional distributions. The squared conditional JS distance of Section 2 adds the average of $D_{\mathrm{JS}} = d_{\mathrm{JS}}^2$ over the input under each of the two input marginals. Writing $\mu_V := \frac{1}{2}(P_V + Q_V)$ for their equal mixture, this sum equals twice the average under the mixture:

$$d_{\mathrm{JS,c}}^2(P_{U|V}, Q_{U|V}) = \int (p_V + q_V)\, d_{\mathrm{JS}}^2(P_{U|V=v}, Q_{U|V=v})\, dv = 2\, \mathbb{E}_{\mu_V}\left[d_{\mathrm{JS}}^2(P_{U|V}, Q_{U|V})\right], \quad (5)$$

the form used throughout the proofs below. The integral form is the one the chain rule of Lemma 3 needs, and the expectation form the one used in the proof of Lemma 5.

Bounded marginal distributions. The proofs below apply Assumption 1 not only to conditional response probabilities but also to marginal ones, and this extension holds automatically: P_Y, Q_Y, P_{Y_θ}, and Q_{Y_θ} are each an average, over x, of conditionals $P_{Y|X=x}(y)$, $Q_{Y|X=x}(y)$, $P_{Y_\theta|X=x}(y)$ that Assumption 1 already bounds below by 2^{-C}, and an average of numbers each at least 2^{-C} is itself at least 2^{-C}.

B.1 Lemmas

The first two lemmas control how much an expectation and an entropy can change when the distribution moves. The last two decompose a Jensen–Shannon distance across variables.

Lemma 1 (Bounded-functional transport)**.** *Let P, Q be distributions on the same measurable space, and let $D_{\mathrm{TV}}(P, Q) := \frac{1}{2}\int |dP - dQ|$ be the total variation distance between them, normalized to take values in $[0, 1]$. Then the following three transport facts hold.*

(i) If $0 \le \ell \le B$, then $|\mathbb{E}_P \ell - \mathbb{E}_Q \ell| \le B\, D_{\mathrm{TV}}(P, Q)$.

(ii) $D_{\mathrm{TV}}(P, Q) \le \sqrt{2}\, d_{\mathrm{JS}}(P, Q)$.

(iii) If g is bounded, then $|\mathbb{E}_P g - \mathbb{E}_Q g| \le \sqrt{2}\, \mathrm{osc}(g)\, d_{\mathrm{JS}}(P, Q)$, where $\mathrm{osc}(g) := \sup g - \inf g$; if $g \ge 0$, then $\mathrm{osc}(g) \le \sup g$.

Proof. (i) Let $\nu := P + Q$ be a dominating measure, $p := dP/d\nu$, $q := dQ/d\nu$, and $E := \{p \ge q\}$. Then

$$\mathbb{E}_P \ell - \mathbb{E}_Q \ell = \int \ell\,(p - q)\, d\nu \overset{(1)}{\le} \int_E \ell\,(p - q)\, d\nu \overset{(2)}{\le} B \int_E (p - q)\, d\nu = B\, D_{\mathrm{TV}}(P, Q),$$

by (1) $\ell \ge 0$ and $p - q < 0$ off E, and (2) $\ell \le B$ and $p - q \ge 0$ on E. Exchanging P and Q gives the other sign.

(ii) With $\mu = \frac{1}{2}(P+Q)$,

$$d_{\mathrm{JS}}^2(P,Q) = \tfrac{1}{2}\big[D_{\mathrm{KL}}(P\,\|\,\mu) + D_{\mathrm{KL}}(Q\,\|\,\mu)\big] \overset{(1)}{\geq} D_{\mathrm{TV}}^2(P,\mu) + D_{\mathrm{TV}}^2(Q,\mu) = \tfrac{1}{2}D_{\mathrm{TV}}^2(P,Q),$$

where (1) is Pinsker's inequality $D_{\mathrm{KL}} \geq 2D_{\mathrm{TV}}^2$ (using the natural logarithm; converting to the base-two bits can only increase the left side, so the inequality continues to hold), and the last step uses $D_{\mathrm{TV}}(P,\mu) = D_{\mathrm{TV}}(Q,\mu) = \frac{1}{2}D_{\mathrm{TV}}(P,Q)$.

(iii) Apply (i) to $\ell := g - \inf g$ with $B := \mathrm{osc}(g)$, then apply (ii), to convert the resulting total variation bound into one in terms of d_{JS}. □

Lemma 2 (Entropy continuity)**.** *Let $\beta < \infty$, and let P, Q be distributions on $\mathcal{Y}$ with $P(y), Q(y) \geq 2^{-\beta}$ for every $y \in \mathcal{Y}$. Then*

$$|H(P) - H(Q)| \leq (2 + \sqrt{2}\beta)\, d_{\mathrm{JS}}(P,Q). \tag{6}$$

Proof. Let m be the mass function of $\mu = \frac{1}{2}(P+Q)$. Then

$$\begin{aligned}
|H(P) - H(Q)| &\overset{(1)}{\leq} |H(P) - H(\mu)| + |H(Q) - H(\mu)| \\
&\overset{(2)}{\leq} D_{\mathrm{KL}}(P\,\|\,\mu) + D_{\mathrm{KL}}(Q\,\|\,\mu) + \beta\big[D_{\mathrm{TV}}(P,\mu) + D_{\mathrm{TV}}(Q,\mu)\big] \\
&= 2\, d_{\mathrm{JS}}^2(P,Q) + \beta\, D_{\mathrm{TV}}(P,Q) \overset{(3)}{\leq} 2\, d_{\mathrm{JS}}^2(P,Q) + \sqrt{2}\beta\, d_{\mathrm{JS}}(P,Q) \\
&\overset{(4)}{\leq} (2 + \sqrt{2}\beta)\, d_{\mathrm{JS}}(P,Q).
\end{aligned}$$

We have (1) by the triangle inequality; (2) because $H(P) - H(\mu) = -D_{\mathrm{KL}}(P\,\|\,\mu) + \mathbb{E}_P[-\log m] - \mathbb{E}_\mu[-\log m]$, where $2^{-\beta} \leq m \leq 1$, the lower bound because $m(y) = \frac{1}{2}[P(y) + Q(y)] \geq 2^{-\beta}$ by hypothesis, so $0 \leq -\log m \leq \beta$ and Lemma 1(i) applies with $\ell = -\log m$ and $B = \beta$, and likewise for Q; (3) by Lemma 1(ii); (4) because $d_{\mathrm{JS}} \leq 1$. □

Lemma 3 (Chain rule for the squared JS distance)**.** *For joint distributions P_{VU} and Q_{VU},*

$$d_{\mathrm{JS}}^2(P_{VU}, Q_{VU}) \leq d_{\mathrm{JS}}^2(P_V, Q_V) + d_{\mathrm{JS,c}}^2(P_{U|V}, Q_{U|V}). \tag{7}$$

Proof. First we define an unbalanced version of d_{JS}^2. For $\alpha \in [0,1]$ put $\mu_\alpha := \alpha P + (1-\alpha)Q$, write $\mu := \mu_{1/2} = \frac{1}{2}(P+Q)$ for the balanced case, and set

$$D_\alpha(P\,\|\,Q) := \alpha D_{\mathrm{KL}}(P\,\|\,\mu_\alpha) + (1-\alpha) D_{\mathrm{KL}}(Q\,\|\,\mu_\alpha).$$

Then

$$D_\alpha(P\,\|\,Q) = \alpha D_{\mathrm{KL}}(P\,\|\,\mu) + (1-\alpha) D_{\mathrm{KL}}(Q\,\|\,\mu) - D_{\mathrm{KL}}(\mu_\alpha\,\|\,\mu) \leq 2\, d_{\mathrm{JS}}^2(P,Q), \tag{8}$$

using $\alpha, 1-\alpha \leq 1$ and $D_{\mathrm{KL}} \geq 0$.

Now let $\mu := \frac{1}{2}(P_{VU} + Q_{VU})$ and $\alpha(v) := p_V(v)/[p_V(v) + q_V(v)]$, so that $\mu_V = \frac{1}{2}(P_V + Q_V)$ and $\mu_{U|V=v} = \alpha(v) P_{U|V=v} + [1-\alpha(v)] Q_{U|V=v}$. The chain rule for D_{KL} gives

$$\begin{aligned}
d_{\mathrm{JS}}^2(P_{VU}, Q_{VU}) &= d_{\mathrm{JS}}^2(P_V, Q_V) + \tfrac{1}{2}\int (p_V + q_V)\, D_{\alpha(v)}(P_{U|V=v}\,\|\,Q_{U|V=v})\, dv \\
&\overset{(1)}{\leq} d_{\mathrm{JS}}^2(P_V, Q_V) + \int (p_V + q_V)\, d_{\mathrm{JS}}^2(P_{U|V=v}, Q_{U|V=v})\, dv \\
&\overset{(2)}{=} \text{right side of Eq. (7)},
\end{aligned}$$

by (1) Eq. (8) at each v, and (2) Eq. (5). □

Lemma 4 (Multimodal decomposition)**.** *For joint distributions P_X and Q_X of the multimodal input $X = (X_v, X_t)$,*

$$\begin{aligned}
2\, d_{\mathrm{JS}}^2(P_X, Q_X) \leq\ & d_{\mathrm{JS}}^2(P_{X_v}, Q_{X_v}) + d_{\mathrm{JS}}^2(P_{X_t}, Q_{X_t}) \\
& + d_{\mathrm{JS,c}}^2(P_{X_t|X_v}, Q_{X_t|X_v}) + d_{\mathrm{JS,c}}^2(P_{X_v|X_t}, Q_{X_v|X_t}).
\end{aligned} \tag{9}$$

Proof. Apply Eq. (7) twice, with $(V,U) = (X_v, X_t)$ and with $(V,U) = (X_t, X_v)$. Both bound the same left-hand side $d_{\mathrm{JS}}^2(P_X, Q_X)$; adding them gives Eq. (9). □

B.2 EMI TRANSFER INEQUALITY

This subsection bounds how far EMI can move between two arbitrary distributions P_{XY} and Q_{XY}; the proof of Theorem 1 later instantiates these as two groups' distributions, $P_{XY}^{(a)}$ and $P_{XY}^{(a')}$, of one dataset, and the proof of Proposition 1 as one group's distributions in the source and target populations, $P_{XY}^{(a)}$ and $Q_{XY}^{(a)}$. Lemma 5 bounds this change in terms of the joint input distance $d_{\mathrm{JS}}(P_X, Q_X)$, by expanding EMI as a difference of entropies and bounding the resulting terms with Lemmas 1 and 2; Lemma 6 then applies Lemma 4 to split that joint distance into the four input sources of Theorem 1.

For P_{XY} and Q_{XY} we write the four input sources and the response source as

$$\begin{aligned}\mathcal{I}(P_X, Q_X) &:= d_{\mathrm{JS}}(P_{X_v}, Q_{X_v}) + d_{\mathrm{JS}}(P_{X_t}, Q_{X_t}) \\ &\quad + d_{\mathrm{JS,c}}(P_{X_t|X_v}, Q_{X_t|X_v}) + d_{\mathrm{JS,c}}(P_{X_v|X_t}, Q_{X_v|X_t}), \\ \mathcal{R}(P_{XY}, Q_{XY}) &:= d_{\mathrm{JS,c}}(P_{Y|X}, Q_{Y|X}),\end{aligned} \tag{10}$$

and define, as in Theorem 1,

$$\widehat{H}(P_{XY}, Q_{XY}) := \tfrac{1}{2}\Big[\sup_x H(P_{Y|X=x}) + \sup_x H(Q_{Y|X=x})\Big] + \sup_x H(P_{Y_\theta|X=x}), \tag{11}$$

with $\kappa(P_{XY}, Q_{XY}) := \widehat{H}(P_{XY}, Q_{XY}) + \sqrt{2}(2+\sqrt{2}C)$ and $\kappa' := \frac{2+\sqrt{2}}{2}(2+\sqrt{2}C)$. Writing $\mathcal{I}(a,a') := \mathcal{I}(P_X^{(a)}, P_X^{(a')})$ and $\mathcal{R}(a,a') := \mathcal{R}(P_{XY}^{(a)}, P_{XY}^{(a')})$, these recover $\widehat{H}_{a,a'}$, $\kappa_{a,a'}$ and the five sources of Theorem 1. Here $\mathcal{I}$ collects the four input-side distances (i)–(iv) of Theorem 1, while $\mathcal{R}$ is the response-side distance (v); $\widehat{H}$ is the entropy scale built from the reference and model response entropies, and κ, κ' are the constants that multiply $\mathcal{I}$ and $\mathcal{R}$, respectively, in the bound below.

Lemma 5 (EMI transfer)**.** *Suppose $P_{Y|X=x}(y)$, $Q_{Y|X=x}(y)$ and $P_{Y_\theta|X=x}(y)$ are at least 2^{-C} for every $x \in \mathcal{X}$ and $y \in \mathcal{Y}$. Then*

$$\big|\mathrm{EMI}(P_{XY};\theta) - \mathrm{EMI}(Q_{XY};\theta)\big| \le \sqrt{2}\,\kappa(P_{XY}, Q_{XY})\, d_{\mathrm{JS}}(P_X, Q_X) + \kappa'\,\mathcal{R}(P_{XY}, Q_{XY}). \tag{12}$$

Proof. Write $H_P(x) := H(P_{Y|X=x})$, $H_Q(x) := H(Q_{Y|X=x})$, $H_\theta(x) := H(P_{Y_\theta|X=x})$, and $d_X := d_{\mathrm{JS}}(P_X, Q_X)$; here $\mu = \frac{1}{2}(P_X + Q_X)$. Expanding each mutual information as $I(X;Y) = H(Y) - \mathbb{E}_X[H(Y \mid X)]$ gives

$$\begin{aligned}\mathrm{EMI}(P_{XY};\theta) - \mathrm{EMI}(Q_{XY};\theta) = &\underbrace{[H(P_{Y_\theta}) - H(Q_{Y_\theta})] - [H(P_Y) - H(Q_Y)]}_{\text{(A)}} \\ &+ \underbrace{\mathbb{E}_{P_X} H_P - \mathbb{E}_{Q_X} H_Q}_{\text{(B)}} - \underbrace{(\mathbb{E}_{P_X} - \mathbb{E}_{Q_X}) H_\theta}_{\text{(C)}}.\end{aligned}$$

We bound the three terms (A), (B), and (C) in turn as follows.

Term (A)*: response entropies.*

$$\begin{aligned}|(\mathrm{A})| &\overset{(1)}{\le} |H(P_{Y_\theta}) - H(Q_{Y_\theta})| + |H(P_Y) - H(Q_Y)| \\ &\overset{(2)}{\le} (2+\sqrt{2}C)\big[d_{\mathrm{JS}}(P_{Y_\theta}, Q_{Y_\theta}) + d_{\mathrm{JS}}(P_Y, Q_Y)\big] \\ &\overset{(3)}{\le} (2+\sqrt{2}C)\big[d_X + d_{\mathrm{JS}}(P_{XY}, Q_{XY})\big] \\ &\overset{(4)}{\le} (2+\sqrt{2}C)\Big[d_X + \big(d_X^2 + \mathcal{R}^2(P_{XY}, Q_{XY})\big)^{1/2}\Big] \\ &\overset{(5)}{\le} (2+\sqrt{2}C)\big[2\,d_X + \mathcal{R}(P_{XY}, Q_{XY})\big].\end{aligned}$$

We have (1) by the triangle inequality; (2) by Lemma 2 with $\beta = C$, which applies because all four marginals are bounded below by 2^{-C}; (3) by the data-processing inequality for d_{JS}, since Y_θ comes from X through the same model under both distributions and Y is a marginal of (X, Y); (4) by Lemma 3 with $(V, U) = (X, Y)$; (5) because $\sqrt{u+v} \le \sqrt{u} + \sqrt{v}$.

Term (B)*: reference entropies.* We separate two effects: the integrand changes, because H_P differs from H_Q, and the measure it is integrated against changes, because P_X differs from Q_X. This gives

$$(\mathrm{B}) = \underbrace{\mathbb{E}_\mu[H_P - H_Q]}_{(\mathrm{B}_1)} + \underbrace{\tfrac{1}{2}(\mathbb{E}_{P_X} - \mathbb{E}_{Q_X})[H_P + H_Q]}_{(\mathrm{B}_2)}.$$

For (B_1), Lemma 2 with $\beta = C$ at each x, then applying Jensen's inequality, then Eq. (5) give

$$\begin{aligned}|(\mathrm{B}_1)| &\le (2+\sqrt{2}C)\,\mathbb{E}_\mu\, d_{\mathrm{JS}}(P_{Y|X}, Q_{Y|X}) \\ &\le (2+\sqrt{2}C)\big[\mathbb{E}_\mu\, d^2_{\mathrm{JS}}(P_{Y|X}, Q_{Y|X})\big]^{1/2} = \tfrac{2+\sqrt{2}C}{\sqrt{2}}\,\mathcal{R}(P_{XY}, Q_{XY}).\end{aligned}$$

For (B_2), Lemma 1(iii) applies since $H_P + H_Q \ge 0$, giving

$$|(\mathrm{B}_2)| \le \tfrac{\sqrt{2}}{2}\sup_x\big[H_P(x) + H_Q(x)\big]\,d_X \le \tfrac{\sqrt{2}}{2}\Big[\sup_x H_P(x) + \sup_x H_Q(x)\Big]d_X.$$

Term (C)*: model entropy.* By Lemma 1(iii) and $H_\theta \ge 0$,

$$|(\mathrm{C})| \le \sqrt{2}\,\operatorname{osc}(H_\theta)\,d_X \le \sqrt{2}\sup_x H_\theta(x)\,d_X.$$

Combining. The d_X coefficients from (B_2) and (C) sum to $\sqrt{2}\,\widehat{H}(P_{XY}, Q_{XY})$ by Eq. (11). Adding all four bounds,

$$\begin{aligned}\big|\mathrm{EMI}(P_{XY};\theta) - \mathrm{EMI}(Q_{XY};\theta)\big| &\le |(\mathrm{A})| + |(\mathrm{B}_1)| + |(\mathrm{B}_2)| + |(\mathrm{C})| \\ &\le \big[\sqrt{2}\,\widehat{H}(P_{XY}, Q_{XY}) + 2(2+\sqrt{2}C)\big]d_X \\ &\quad + \big(\tfrac{1}{\sqrt{2}} + 1\big)(2+\sqrt{2}C)\,\mathcal{R}(P_{XY}, Q_{XY}),\end{aligned}$$

which is Eq. (12), since $\sqrt{2}\widehat{H}(P_{XY}, Q_{XY}) + 2(2+\sqrt{2}C) = \sqrt{2}\kappa(P_{XY}, Q_{XY})$ and $(\frac{1}{\sqrt{2}} + 1)(2 + \sqrt{2}C) = \kappa'$. □

Lemma 6 (Modality-resolved EMI transfer)**.** *Under the same lower bound assumption of Lemma 5, we have*

$$\big|\mathrm{EMI}(P_{XY};\theta) - \mathrm{EMI}(Q_{XY};\theta)\big| \le \kappa(P_{XY}, Q_{XY})\,\mathcal{I}(P_X, Q_X) + \kappa'\,\mathcal{R}(P_{XY}, Q_{XY}). \tag{13}$$

Proof. It suffices to bound the joint input distance of Eq. (12) by the four separate sources:

$$\sqrt{2}\,d_{\mathrm{JS}}(P_X, Q_X) = \big(2\,d^2_{\mathrm{JS}}(P_X, Q_X)\big)^{1/2} \overset{(1)}{\le} \big(\text{right side of Eq. (9)}\big)^{1/2} \overset{(2)}{\le} \mathcal{I}(P_X, Q_X),$$

by (1) Lemma 4, and (2) $\sqrt{\sum_k u_k} \le \sum_k \sqrt{u_k}$ for $u_k \ge 0$. Substituting into Eq. (12) gives Eq. (13). □

B.3 Proof of Theorem 1

The proof applies Lemma 6 to every pair of groups and takes the maximum over pairs.

Proof. By Assumption 1, every pair $(P^{(a)}_{XY}, P^{(a')}_{XY})$ satisfies the hypotheses of Lemma 5, so Lemma 6 applies to each pair:

$$\mathrm{FEMI}(\theta) = \max_{a \ne a'}\big|\mathrm{EMI}^{(a)}(\theta) - \mathrm{EMI}^{(a')}(\theta)\big| \le \max_{a \ne a'}\big\{\kappa_{a,a'}\,\mathcal{I}(a,a') + \kappa'\,\mathcal{R}(a,a')\big\},$$

where the maximum may be restricted to $a \ne a'$ because the diagonal terms vanish. Unfolding $\mathcal{I}(a,a')$ and $\mathcal{R}(a,a')$ through Eq. (10) into sources (i)–(v) gives Eq. (2). □

B.4 Proof of Proposition 1

Proof. First inequality. By the definition of s_a, for every pair (a, a'),

$$\mathrm{EMI}_Q^{(a)}(\theta) - \mathrm{EMI}_Q^{(a')}(\theta) = \left[\mathrm{EMI}_P^{(a)}(\theta) - \mathrm{EMI}_P^{(a')}(\theta)\right] + (s_a - s_{a'}). \tag{14}$$

Taking absolute values and the maximum over pairs gives $\mathrm{FEMI}_Q(\theta) \le \mathrm{FEMI}_P(\theta) + \max_{a,a'} |s_a - s_{a'}|$; exchanging the roles of P and Q gives the reverse inequality.

Second inequality. Fix a group a. By assumption, $P_{XY}^{(a)}$ and $Q_{XY}^{(a)}$ satisfy the lower bound of Lemma 5, so Lemma 6 with $(P_{XY}, Q_{XY}) = (P_{XY}^{(a)}, Q_{XY}^{(a)})$ gives

$$|s_a| \le \kappa_a \mathcal{I}_a + \kappa' \mathcal{R}_a = \Delta_a,$$

since for this pair κ, $\mathcal{I}$, and $\mathcal{R}$ of Eqs. (10) and (11) reduce to κ_a, $\mathcal{I}_a$, and $\mathcal{R}_a$ of Section 3.2. Hence $|s_a - s_{a'}| \le \Delta_a + \Delta_{a'}$, and taking the maximum over pairs completes the proof. □

C Method Details

This appendix gives the estimation procedure summarized in Section 3.3. Theorem 1 is a statement about population Jensen–Shannon distances. A benchmark of a few thousand samples per group cannot estimate these directly: the marginal distances require density ratios in a high-dimensional space, and the conditional ones compare distributions at inputs that essentially never repeat. We therefore replace each of the five sources with a kernel discrepancy on frozen embeddings that plays the same diagnostic role, vanishing when its theoretical counterpart does, under conditions we state where each source is introduced. The rest of this appendix follows the same order as Eq. (2): Section C.1 fixes the representation, Section C.2 estimates the left-hand side, Sections C.3–C.5 estimate the right-hand side, and Sections C.6–C.7 cover normalization and the distribution-shift setting.

The pipeline assembles standard tools: a variational mutual information bound for the left-hand side, and kernel two-sample and conditional mean embedding estimators for the right-hand side. We cite the original source of each component where it is introduced and do not restate its derivation. Our own contribution here is the mapping from the five theoretical sources of Eq. (2) to five estimators that stay comparable across groups of very unequal size, together with the bias corrections that such comparability requires.

One clarification is needed before we begin. MMD and CMMD are not numerically equal to d_{JS} and $d_{\mathrm{JS,c}}$. The weights of Theorem 1, namely the entropy scale $\widehat{H}_{a,a'}$ and the bounded-response constant of Assumption 1, come from the entropy-continuity argument rather than from any calibration we perform. We therefore never substitute the estimated sources into Eq. (2) and claim a certified finite-sample upper bound. Instead, the five sources are reported entry by entry, as a theory-guided account of where a dataset's group disparity is located; the one composite we form from them is an unweighted sum.

C.1 Evaluation units and frozen embeddings

Each sample is a realization of the tuple (X_v, X_t, Y, A) from Section 2 (image, query, reference response, and sensitive attribute), together with the model response $Y_\theta \sim P_{Y_\theta|X}$ and identifiers for the evaluated model and the task. Samples are grouped by the value of A, which is exactly what the superscript in $P_{XY}^{(a)}$ selects. We treat each image–question row as one independent sample. Every quantity reported below is computed separately within one dataset–model–task stratum; when a benchmark provides more than one sensitive attribute, A is instantiated once per attribute, and each attribute is audited independently of the others.

Raw variables are mapped to a common frozen space by fixed encoders, following the EMI estimation protocol of Oh et al. (2025). The vision embedding $Z_v = f_v(X_v)$ comes from the vision tower of CLIP ViT-B/32 (Radford et al., 2021), taking the mean of the final-layer patch tokens. The text embeddings $Z_t = f_t(X_t)$, $Z_y = f_t(Y)$, and $Z_{y_\theta} = f_t(Y_\theta)$ all come from a single XLM-R base text encoder (Conneau et al., 2020), applied respectively to the query, the reference response,

and the model response. All embeddings are ℓ_2-normalized. For the kernel discrepancies, the joint input embedding is the stacked vector $Z_x := (Z_v^\top, Z_t^\top)^\top$, renormalized to unit norm. The CLUB critic of Section C.2 instead consumes the averaged input $\widetilde{Z}_x := \frac{1}{2}(Z_v + Z_t)$, which keeps its input dimension equal to the encoder width. Throughout, a lowercase symbol with a sample index denotes the corresponding realization, so that $z_{x,i}$, $\widetilde{z}_{x,i}$ and $z_{y,i}$ are the embeddings of sample i.

Two properties of this construction are important for fairness estimation. First, the encoders are pretrained and never adapted. Every kernel, bandwidth, and random feature map derived from them is fitted once per dataset, on all groups pooled, and then shared by every group and every model. Had each group been given a separately fitted representation or kernel, the resulting differences could reflect the estimators rather than the group distributions. Second, the model response Z_{y_θ} enters only the group-wise EMI on the left-hand side of Eq. (2). The five sources on the right-hand side are computed from Z_v, Z_t, Z_x, Z_y alone, which makes them model-independent in the sense of Section 3.1, and therefore comparable across the ten models of our benchmark. For the same reason, the kernel on the response space is fitted on the references only, then applied to both Z_y and Z_{y_θ}. Fitting it on the two pooled together would let the model's outputs move the bandwidth, so that source (v), which reads inputs and references alone, would change when the model changes, for no reason other than kernel selection.

One deviation from this rule is deliberate. Comparing a fairness-enhancing fine-tuned checkpoint against its own vanilla checkpoint (Fig. 4) asks whether the intervention changed the representation the model actually uses, which frozen external encoders cannot see. For that comparison alone, Z_v and Z_t are taken from a middle layer of the evaluated model instead of from the frozen encoders; every step below is otherwise unchanged. Those values are comparable across the checkpoints of one model, not across models, and they are not pooled with the model-independent sources reported everywhere else.

C.2 Group-wise EMI and FEMI

Each group's EMI is a difference of two mutual informations, and a mutual information is a divergence between a joint distribution and the product of its marginals, neither of which is available here. We use CLUB (Cheng et al., 2020), which avoids density estimation by learning a variational conditional model $q_\eta(z_y \mid \widetilde{z}_x)$, taken to be a diagonal Gaussian $\mathcal{N}\big(m_\eta(\widetilde{z}_x), \operatorname{diag} e^{\ell_\eta(\widetilde{z}_x)}\big)$ whose mean and log-variance heads are two-layer $\tanh$ networks. For the n_a samples of group a,

$$\widehat{I}_{\mathrm{CLUB},a}(\widetilde{Z}_x; Z_y) = \frac{1}{n_a}\sum_{i=1}^{n_a} \log q_\eta(z_{y,i} \mid \widetilde{z}_{x,i}) - \frac{1}{n_a^2}\sum_{i=1}^{n_a}\sum_{j=1}^{n_a} \log q_\eta(z_{y,j} \mid \widetilde{z}_{x,i}), \tag{15}$$

where the first average scores observed pairs and the second, over mismatched pairs, represents the product of the marginals; we refer to Cheng et al. (2020) for the derivation and for the conditions under which Eq. (15) upper-bounds the mutual information. Because $\log q_\eta$ is quadratic in its target under a diagonal Gaussian, the double sum in Eq. (15) can be computed exactly in $O(n_a)$ time, from the first two moments of $\{z_{y,j}\}$ and the per-sample quantities $e^{-\ell_\eta}$, $m_\eta e^{-\ell_\eta}$, and $m_\eta^2 e^{-\ell_\eta}$. No minibatch permutation approximation is needed, and the value does not depend on batch ordering.

The two mutual informations of $\mathrm{EMI}^{(a)}(\theta)$ in Section 2 are estimated this way in the frozen embedding space, giving

$$\widehat{\mathrm{EMI}}^{(a)} = \widehat{I}_{\mathrm{CLUB},a}(\widetilde{Z}_x; Z_{y_\theta}) - \widehat{I}_{\mathrm{CLUB},a}(\widetilde{Z}_x; Z_y), \qquad \widehat{\mathrm{FEMI}} = \max_{a,a' \in \mathcal{A}} \big|\widehat{\mathrm{EMI}}^{(a)} - \widehat{\mathrm{EMI}}^{(a')}\big|, \tag{16}$$

where $\widetilde{Z}_x$, Z_{y_θ} and Z_y stand for embeddings of X, Y_θ and Y; the second expression is Eq. (1) with $M = \widehat{\mathrm{EMI}}$, so it is the empirical counterpart of $\mathrm{FEMI}(\theta)$. A single critic, trained once on the pooled data, is frozen and reused for both mutual informations and for every group. The two terms of $\widehat{\mathrm{EMI}}^{(a)}$ therefore share architecture, capacity, optimization budget, and stopping rule, so their difference is unlikely to be dominated by unequal estimator capacity.

C.3 Kernel and random Fourier features

We use two standard properties of this kernel repeatedly below. This kernel is *characteristic* (Sriperumbudur et al., 2010): its induced MMD is zero if and only if the two compared distributions

are identical, so the marginal discrepancy of Section C.4 vanishes exactly when the two groups' marginals coincide. The conditional discrepancy of Section C.5 enjoys the same guarantee, but only under the additional conditions stated there (Park & Muandet, 2020). The kernel is also *bounded*, i.e., $0 < k_\sigma \leq 1$, so every discrepancy built from it takes values in a fixed, known range; Section C.6 uses this range to place all five sources on a common $[0, 1]$ scale.

Exact kernel computation is cubic in the group size because the conditional estimator of Section C.5 inverts an $n_g \times n_g$ Gram matrix. We therefore work in the primal form given by R random Fourier features (Rahimi & Recht, 2007): a map $\varphi(z) \in \mathbb{R}^R$ whose r-th coordinate is $\sqrt{2/R}\cos(\omega_r^\top z + b_r)$, with frequencies $\omega_r \sim \mathcal{N}(0, \sigma^{-2} I_d)$ and phases $b_r \sim \mathrm{Unif}[0, 2\pi]$ drawn once per space and shared by all groups, so that $\varphi(z)^\top \varphi(z') \approx k_\sigma(z, z')$. This replaces an inversion of size n_g by one of size R, at the cost of an approximation that becomes exact only as R grows. Since $\varphi(z)^\top \varphi(z)$ is therefore not exactly 1 in a finite feature space, the corrections below that drop the diagonal terms are written in terms of the observed $\|\varphi(z)\|^2$ rather than assuming the value one.

C.4 Marginal sources (i) and (ii)

Sources (i) and (ii) compare two groups' marginal distributions of Z_v and of Z_t. We use the maximum mean discrepancy between kernel mean embeddings introduced in Section 3.3, $\mathrm{MMD}^2(P_Z^{(a)}, P_Z^{(a')}) = \|\mu_Z^{(a)} - \mu_Z^{(a')}\|_{\mathcal{H}}^2$ with $\mu_Z^{(a)} := \mathbb{E}_{P_Z^{(a)}}[k_\sigma(Z, \cdot)]$. Unlike the marginal d_{JS} terms it stands in for, this needs only samples.

We use the unbiased U-statistic of Gretton et al. (2012), which omits the diagonal terms. In the primal form it is computed from group moments alone: writing $\bar{\varphi}_g := \frac{1}{n_g}\sum_i \varphi(z_i)$ and $\bar{k}_g := \frac{1}{n_g}\sum_i \|\varphi(z_i)\|^2$ for group g,

$$\widehat{\mathrm{MMD}}_u^2 = \frac{n_a\|\bar{\varphi}_a\|^2 - \bar{k}_a}{n_a - 1} + \frac{n_{a'}\|\bar{\varphi}_{a'}\|^2 - \bar{k}_{a'}}{n_{a'} - 1} - 2\,\langle \bar{\varphi}_a, \bar{\varphi}_{a'} \rangle. \tag{17}$$

This differs from the plug-in value $\|\bar{\varphi}_a - \bar{\varphi}_{a'}\|^2$ by exactly $-\operatorname{tr}\mathrm{Cov}_a(\varphi)/(n_a - 1) - \operatorname{tr}\mathrm{Cov}_{a'}(\varphi)/(n_{a'} - 1)$, where $\mathrm{Cov}_g(\varphi)$ is the covariance of the random features inside group g. That the plug-in value is too large by a term of order $1/n_g$, even when the two distributions are identical, is standard (Gretton et al., 2012). The consequence for a fairness audit is the reason we correct it: a pair containing a small group would otherwise appear more disparate for reasons of sample size alone. Eq. (17) can be negative when the distributions coincide, which is the correct behavior of an unbiased estimator and is clipped only at the normalization step. Applying the normalization of Eq. (20) to this value with $Z = Z_v$ and with $Z = Z_t$ gives the two marginal sources, which we write $\widehat{d}_v$ and $\widehat{d}_t$.

C.5 Conditional sources (iii) to (v)

Sources (iii), (iv) and (v) compare conditional distributions, for the pairs $(V, U) = (Z_v, Z_t)$, (Z_t, Z_v) and (Z_x, Z_y) respectively. A histogram-style conditional divergence is unavailable because the conditioning inputs are continuous embeddings that essentially never repeat, so we compare conditional mean embeddings instead.

Conditional mean embedding. Within group a, the conditional mean embedding $\mu_{U|V=v}^{(a)} := \mathbb{E}^{(a)}[\psi(U) \mid V = v]$ is estimated by kernel ridge regression (Song et al., 2009; Grünewälder et al., 2012; Park & Muandet, 2020), which pools information across similar conditioning inputs instead of requiring exact repeats. With $\Phi^{(a)} \in \mathbb{R}^{n_a \times R}$ and $\Psi^{(a)} \in \mathbb{R}^{n_a \times R}$ the feature matrices of the conditioning and response variables, the regularized conditional mean operator is

$$\widehat{C}_{U|V}^{(a)} = \big(\Psi^{(a)}\big)^\top \Phi^{(a)} \Big[\big(\Phi^{(a)}\big)^\top \Phi^{(a)} + n_a \lambda_a I_R\Big]^{-1}, \qquad \widehat{\mu}_{U|V=v}^{(a)} = \widehat{C}_{U|V}^{(a)} \varphi(v), \tag{18}$$

which in practice is obtained by a linear solve rather than an explicit matrix inverse. The regularization level is $\lambda_g = c_\lambda\, n_g^{-\gamma}$ with $c_\lambda = 0.1$ and $\gamma = 0.25$, an exponent in the range $(0, \frac{1}{3})$ for which this estimator is consistent (Fukumizu et al., 2013); the same rule is applied to every group.

Conditional MMD. The two groups are compared by the conditional MMD of Eq. (4), which averages $\|\mu^{(a)}_{U|V} - \mu^{(a')}_{U|V}\|^2$ over the balanced mixture $\rho := \frac{1}{2}(P^{(a)}_V + P^{(a')}_V)$. This is the kernel conditional discrepancy of Park et al. (2021), whose Lemma 4.3 gives the condition under which it separates two conditional distributions, estimated there with the same regularized operators as in Eq. (18); Moskvichev et al. (2026) place it in a hierarchy of kernel conditional discrepancies, in which the operator-norm variant of Ren et al. (2016) forms a separate level. Averaging over ρ rather than over one group's inputs draws on both input marginals, as $d_{\mathrm{JS,c}}$ does in Eq. (5), though with the two weights normalized rather than summed; it also keeps the quantity symmetric in a and a'. The empirical averaging measure $\widehat{\rho}$ puts weight $\frac{1}{2}$ on each group's own conditioning points.

Why the plug-in estimator needs correcting. Substituting Eq. (18) into Eq. (4) gives the plug-in estimator $\mathbb{E}_{v\sim\widehat{\rho}}\|\widehat{\Delta}\varphi(v)\|^2$, with $\widehat{\Delta} := \widehat{C}^{(a)}_{U|V} - \widehat{C}^{(a')}_{U|V}$. Writing $\widehat{\Delta} = \Delta + E^{(a)} - E^{(a')}$, the true operator difference plus the two estimation errors, and squaring, the errors contribute their own norms $\mathbb{E}\|E^{(g)}\varphi(v)\|^2$, each nonnegative and of order $1/n_g$. This is the conditional counterpart of the plug-in bias of Section C.4, with the same consequence: the estimate stays positive even when the two conditional distributions are identical, by an amount that grows as a group shrinks, so any pair containing a small group would appear more disparate.

Split-half estimator. Splitting removes the offset, in the spirit of the cross-fitting argument of Chernozhukov et al. (2018). For each group g, we divide its n_g samples at random into two disjoint halves and fit Eq. (18) separately on each, with the regularization rule evaluated at the half size, $c_\lambda\lfloor n_g/2\rfloor^{-\gamma}$. This gives two differences $\Delta_h := \widehat{C}^{(a)}_h - \widehat{C}^{(a')}_h$ for $h \in \{1, 2\}$. The estimator then replaces the squared norm by an inner product of these two,

$$\widehat{\mathrm{CMMD}}^2 := \mathbb{E}_{v\sim\widehat{\rho}}\big\langle \Delta_1\varphi(v),\, \Delta_2\varphi(v)\big\rangle. \tag{19}$$

The two halves share no sample, so their estimation errors are independent. The fluctuating part of those errors has mean zero, so the cross term it contributes to Eq. (19) vanishes in expectation, and the $1/n_g$ floor vanishes with it. The systematic part, the bias of the ridge regression, is shared by both halves and does not cancel; we return to it below. Once the cross term is gone, the estimator reduces to the squared difference of the two conditional mean operators, which vanishes when the two conditional distributions agree. The converse direction makes the quantity a discrepancy rather than a mere summary, and a characteristic kernel on the response space delivers it: because ρ dominates both groups' conditioning distributions, the estimand vanishes only when the two conditional distributions agree ρ-almost everywhere (Park et al., 2021). The estimator inherits this only approximately. It replaces the conditional mean embeddings by regularized operators in a finite random-feature space, which need not be rich enough to represent them (Moskvichev et al., 2026), and we assume rather than verify that it is. As with the unbiased MMD of Eq. (17), the value may come out negative, which means that no conditional difference is resolvable at the available sample size. We average Eq. (19) over five independent random splits, which reduces the noise introduced by the split itself.

The estimator has two limits. Splitting removes the variance floor but not the bias of the ridge regression, which is why λ is set from the half size $\lfloor n_g/2\rfloor$ rather than from n_g. And $\widehat{\rho}$ is built from the same conditioning points used to fit the operators; the resulting dependence is of smaller order, and we do not correct for it. The three conditional sources are then $\widehat{c}_{t|v}$, $\widehat{c}_{v|t}$ and $\widehat{c}_{y|x}$, the split-half estimates of Eq. (4) for $(V, U) = (Z_v, Z_t)$, (Z_t, Z_v) and (Z_x, Z_y), in the order in which sources (iii), (iv) and (v) appear in Eq. (2).

C.6 Normalization and reported sources

The five estimates are not yet comparable to one another. The reason is units, not substance. The theoretical sources they stand for live on two different scales: the marginal ones are d_{JS} values in $[0, 1]$, while the conditional ones are $d_{\mathrm{JS,c}}$ values in $[0, \sqrt{2}]$, because the convention of Eq. (5) sums over the two input marginals instead of averaging over them. Left as they are, a conditional source would read as larger than a marginal one for no reason but the scale it happens to sit on, and five numbers meant to show *where* a disparity lies would instead show where the units are widest. The raw quantities are at least bounded: expanding either squared discrepancy into its expected kernel

values (Gretton et al., 2012) and using $0 < k_\sigma \leq 1$ caps it at two, and for the conditional case the cap survives the averaging over ρ.

We therefore put every estimate on a common $[0, 1]$ scale by applying

$$\widehat{D}^2 \;\longmapsto\; \min\Big\{1,\ \sqrt{\max\{0, \widehat{D}^2\}/2}\Big\} \in [0, 1], \tag{20}$$

to the unbiased MMD of Eq. (17) and to the split-half CMMD of Eq. (19) alike. The square root matches the one in $d_{\mathrm{JS}} = \sqrt{D_{\mathrm{JS}}}$ and the division rescales the $[0, 2]$ range. The floor at zero absorbs the negative values a debiased estimator is entitled to return, and the ceiling at one absorbs the small overshoots that the random-feature approximation can produce.

For each group pair we then report the five normalized sources themselves: the two marginal distances $\widehat{d}_v$ and $\widehat{d}_t$, then the three conditional ones $\widehat{c}_{t|v}$, $\widehat{c}_{v|t}$ and $\widehat{c}_{y|x}$, in the order in which sources (i) to (v) appear in Eq. (2). The figures and tables of Section 4, and the figures of Appendix E, carry these same five entries in the same order, but label them by their roman numerals rather than by these symbols.

C.7 Use under distribution shift

The distribution-shift analysis of Section 3.2 asks a different question of the same machinery. Only the inputs change. Instead of comparing two groups inside one dataset, we compare a single group across two datasets: the two samples entering the marginal and conditional estimators become that group's source and target data, in place of the two groups' data. MMD then measures how far that group's image and query distributions travel from source to target, and the split-half CMMD measures how far its cross-modal coupling and its reference mechanism travel. Everything else is reused verbatim: the frozen encoders, the pooled bandwidth, the normalization. A source measured across the shift is therefore on the same scale as the same source measured between two groups.

D Experiment Details

D.1 Datasets

D.1.1 MIMIC-CXR

Dataset description. MIMIC-CXR (Johnson et al., 2019a) is a large-scale chest radiograph collection acquired at the Beth Israel Deaconess Medical Center in Boston, MA, USA, comprising 377,110 de-identified images across 227,835 imaging studies. We use the JPG-converted release, MIMIC-CXR-JPG (Johnson et al., 2019b), as the image source. We link each study to MIMIC-IV (Johnson et al., 2023) to obtain patient demographics.

Benchmark construction. We use the closed-ended and open-ended QAs from MIMIC-Ext-MIMIC-CXR-VQA (Bae et al., 2024), a human- and program-authored VQA benchmark of 377,391 pairs generated from radiology knowledge-graph-grounded programs over three official splits, and reshape it into tasks using its own `semantic_type` field: `verify` items become closed-ended QA, `query` items become open-ended QA. Demographics are joined from MIMIC-IV `hosp/patients.csv` and `hosp/admissions.csv`. We use the LLaVA-Rad MIMIC-CXR annotations (Zambrano Chaves et al., 2025), in which the Findings section has already been extracted from each real report, for our Report Generation task. The resulting benchmark contains 137,193 / 33,225 / 6,143 closed-ended QA pairs, 85,312 / 22,672 / 4,689 open-ended QA pairs, and 300,169 / 2,454 / 4,523 report generation pairs for the train / validation / test splits, with sensitive attributes `Sex`, `Age`, and `Race`.

Dataset access and license. All four component resources are hosted on PhysioNet and are separate credentialed projects, each requiring its own approval: MIMIC-CXR-JPG (`https://physionet.org/content/mimic-cxr-jpg/`), MIMIC-Ext-MIMIC-CXR-VQA (`https://physionet.org/content/mimic-ext-mimic-cxr-vqa/`), MIMIC-IV (`https://physionet.org/content/mimiciv/`), and the LLaVA-Rad annotations (`https://physionet.org/content/llava-rad-mimic-cxr-annotation/1.0.0/`).

D.1.2 CHEXPERT PLUS

Dataset description. CheXpert Plus (Chambon et al., 2024) augments the widely used CheXpert chest radiograph collection from Stanford Hospital with the corresponding free-text radiology reports and patient demographics. It contains 223,228 unique image–report pairs across 187,711 studies from 64,725 patients, together with 14 CheXbert pathology labels per study and eight de-identified demographic fields.

Benchmark construction. We construct our own split, grouped by patient identifier so that all studies from a patient fall in the same partition and near-duplicate repeat radiographs cannot leak across it, and stratified by whether a patient has at least one abnormal study, at an 80/10/10 ratio. Closed-ended QA questions are templated directly from the 14 finding columns, one binary question per finding. Report generation copies the real Findings text as the reference answer. Sex, age, and race are binarized to Male/Female, <60/60+, and White/Non-white respectively, and records that do not resolve on all three are dropped. This yields 209,321 / 26,742 / 26,932 closed-ended QA pairs over the train / validation / test splits.

Dataset access and license. CheXpert Plus is distributed through the Stanford AIMI shared-datasets portal (`https://aimi.stanford.edu/datasets/chexpert-plus`) under the Stanford University Dataset Research Use Agreement.

D.1.3 PADCHEST-GR

Dataset description. PadChest-GR (Castro et al., 2025) is a bilingual grounded-reporting subset of PadChest (Bustos et al., 2020), the chest X-ray collection acquired at Hospital Universitario de San Juan in Alicante, Spain. It comprises 4,555 frontal chest X-ray studies (3,099 abnormal and 1,456 normal), each paired with a complete list of sentences describing individual present and absent findings in both Spanish and English, for a total of 7,037 positive and 3,422 negative finding sentences. Positive findings additionally carry radiologist-drawn bounding boxes.

Benchmark construction. We use the English sentence-level findings and discard the bounding-box annotations. Closed-ended QA is templated from the per-study finding labels, one binary question per finding category. QAs are resampled to balance the yes and no answers while covering all finding areas. Report generation concatenates the grounded report sentences into a reference findings paragraph. Sex and age are binarized to Male/Female and <60/60+. The resulting benchmark contains 6,982 / 988 / 1,998 closed-ended QA pairs (3,045 / 442 / 881 unique images) and 3,185 / 455 / 915 pairs for each of open-ended QA and report generation over train / validation / test.

Dataset access and license. PadChest-GR is distributed by the Medical Imaging Databank of the Valencia Region (BIMCV) at `https://bimcv.cipf.es/bimcv-projects/padchest-gr/`.

D.1.4 MERLIN ABDOMINAL CT

Dataset description. The Merlin Abdominal CT dataset (Blankemeier et al., 2026) consists of 25,494 abdominal and pelvic CT scans from 18,317 patients, acquired at the Stanford Hospital Emergency Department between 2012 and 2018 and identified by CPT code. Each scan is stored as a de-identified 3D NIfTI volume paired with its real radiology report, patient demographics (age, gender, race), an official train/validation/test split, and 30 zero-shot-derived finding labels spanning conditions such as submucosal edema, renal cyst, and hepatic steatosis.

Benchmark construction. Closed-ended QA is templated from the 30 finding columns and report generation copies the real report text. Open-ended QA pairs are synthesized per study with GPT-5-mini grounded in the real report. We retain the official split and binarize sex, age, and race to Male/Female, <60/60+, and White/Non-white, dropping the studies with missing demographics. The result is 100,544 / 33,751 / 33,577 closed-ended QA pairs and 15,088 / 5,008 / 5,050 pairs for each of open-ended QA and report generation over train / validation / test.

Dataset access and license. The dataset is hosted by the Stanford AIMI Center at https://stanfordaimi.azurewebsites.net/datasets/60b9c7ff-877b-48ce-96c3-0194c8205c40.

D.1.5 FAIRVLMED

Dataset description. Harvard-FairVLMed (Luo et al., 2024) is a vision–language dataset built explicitly for fairness research in ophthalmology. It contains 10,000 subjects who received glaucoma care at Massachusetts Eye and Ear, Harvard Medical School, between 2015 and 2022. Each subject contributes one scanning laser ophthalmoscopy (SLO) fundus image, a de-identified clinical note summarizing the glaucoma assessment, a ground-truth glaucoma label, and six self-reported demographic attributes: age, gender, race, ethnicity, preferred language, and marital status.

Benchmark construction. We retain the official 7,000 / 1,000 / 2,000 train / validation / test split. Closed-ended QA poses a single templated binary question per image about the presence of glaucoma, giving one QA pair per image and 7,000 / 1,000 / 2,000 pairs respectively. We binarize gender to Male/Female, age to <60/60+, and race to White/Non-white, collapsing the dataset's Asian and Black categories into the latter.

Dataset access and license. FairVLMed is released by the Harvard Ophthalmology AI Lab through the FairCLIP project page (https://github.com/Harvard-Ophthalmology-AI-Lab/FairCLIP) under the CC BY-NC-ND 4.0 license.

D.1.6 BRSET

Dataset description. The Brazilian Multilabel Ophthalmological Dataset (BRSET) (Nakayama et al., 2024) comprises 16,266 color fundus photographs from 8,524 patients, collected between 2010 and 2020 at three outpatient ophthalmological centers in São Paulo, Brazil. Each image is accompanied by patient demographics (age, sex, nationality, clinical history), anatomical and quality-control annotations, two diabetic-retinopathy severity gradings, and 13 binary finding labels including diabetic retinopathy, macular edema, drusen, age-related macular degeneration, and hemorrhage.

Benchmark construction. BRSET ships no free-text report at all, only structured labels. Closed-ended QA is therefore templated directly from the 13 finding columns, one binary question per finding, exactly as for the other datasets. BRSET also provides no split column, so we construct one: grouped by patient, stratified by diabetic-retinopathy positivity, at an 80/20 ratio with a fixed seed. Sex and age are binarized to Male/Female and <60/60+. This yields 26,049 closed-ended QA pairs over 8,683 training images and 6,381 pairs over 2,127 test images.

Dataset access and license. BRSET is hosted on PhysioNet at https://physionet.org/content/brazilian-ophthalmological/ (we use v1.0.2) as a credentialed resource.

D.1.7 HAM10000

Dataset description. HAM10000 ("Human Against Machine with 10000 training images") (Tschandl et al., 2018) contains 10,015 dermatoscopic images of pigmented skin lesions, collected over twenty years at two sites: the Department of Dermatology at the Medical University of Vienna, Austria, and the skin cancer practice of Cliff Rosendahl in Queensland, Australia. Images are labeled with seven diagnostic categories, of which melanoma is the clinically critical one. Per-image metadata includes a lesion identifier, age, sex, and lesion localization.

Benchmark construction. Closed-ended QA asks one templated binary question per image, namely whether the lesion is melanoma, rather than one-hot encoding all seven diagnostic categories. This keeps the task clinically meaningful and avoids the extreme per-question class imbalance that one-hot encoding would introduce. We construct our own split directly from the public release: grouped by lesion identifier so that multiple images of the same lesion cannot leak across the boundary, and stratified to match the melanoma rate across partitions. Sex and age are binarized

to Male/Female and <60/60+. The result is 7,955 training and 1,993 test closed-ended QA pairs, one per image.

Dataset access and license. HAM10000 is deposited at the Harvard Dataverse (`https://doi.org/10.7910/DVN/DBW86T`) and mirrored in the ISIC Archive, under the CC BY-NC 4.0 license.

D.1.8 FITZPATRICK17K

Dataset description. Fitzpatrick17k (Groh et al., 2021) contains 16,577 clinical (rather than dermatoscopic) dermatology photographs compiled from two online atlases, DermaAmin (12,672 images) and Atlas Dermatologico (3,905 images), spanning 114 skin conditions with at least 53 images per condition. Every image is annotated with a Fitzpatrick skin type on the six-point scale from Type I (lightest) to Type VI (darkest), assigned by a dynamic-consensus protocol over two to five annotators calibrated against a dermatologist-labeled gold-standard subset.

Benchmark construction. Fitzpatrick17k carries `skin_type`, binarized to **Lighter** (Types I–III) versus **Darker** (Types IV–VI). Images without a confident skin type annotation (565 of 16,577, or 3.4%) are dropped. Closed-ended QA asks one templated binary question per image, whether the depicted condition is malignant, derived from the three-way benign/malignant/non-neoplastic partition label and yielding a 13.5% positive rate. We construct a random split stratified by the malignancy label at an 80/20 ratio with a fixed seed. This yields 12,809 training and 3,203 test closed-ended QA pairs, one per image, with a 69.2%/30.8% Lighter/Darker composition in training.

Dataset access and license. The Fitzpatrick skin-type annotations are published at `https://github.com/mattgroh/fitzpatrick17k` under a CC BY-NC-SA license. We obtained the image archive by submitting the request form provided by the dataset authors, as their documentation directs.

D.2 MODELS

Generalist models. **LLaVA-1.5-7B** (Liu et al., 2024) pairs a CLIP ViT-L/14 vision encoder with a Vicuna-7B language backbone through a two-layer MLP projector, trained with visual instruction tuning on public academic-task data. **Qwen2.5-VL-7B** (Bai et al., 2025) is a 7B model with a native dynamic-resolution vision transformer and window attention, supporting fine-grained visual grounding and document understanding. **InternVL3-8B** (Zhu et al., 2025) is an 8B model trained with a native multimodal pre-training recipe that jointly learns from multimodal and text-only corpora in a single stage. **Gemma-3-4B** (Gemma Team, 2025) is a 4B open multimodal model from the Gemma 3 family, supporting image understanding and long context.

Medical specialist models. **MedGemma-4B** (Sellergren et al., 2025) further trains Gemma-3-4B on medical image–text data for medical image understanding and reasoning. **Lingshu-7B** and **Lingshu-I-8B** (Xu et al., 2026) are generalist medical foundation models built on the Qwen2.5-VL and InternVL3 backbone, respectively. Both of them are trained on curated medical imaging, text, and VQA data through a multi-stage alignment/instruction-tuning/reinforcement-learning pipeline. **LLaVA-Med-7B** (Li et al., 2023) adapts LLaVA to biomedicine via figure–caption pairs and GPT-4-generated instruction data drawn from the biomedical literature.

Commercial models (zero-shot only). **GPT-4.1** (OpenAI, 2025) and **Grok 4.20** (xAI, 2025) are proprietary multimodal models accessed via API. Since we cannot fine-tune them, they are evaluated zero-shot only, alongside the zero-shot runs of the 8 open-weight models above.

D.3 TASKS AND METRICS

Closed-ended QA with F1. Every closed-ended question is templated directly from a dataset's own binary finding labels. We prompt MLLMs to respond with only "yes" or "no", parse the selected answer from each response, and compute the F1 score against the ground-truth yes/no label.

Open-ended QA with LLM-judge Score. We synthesize each open-ended question/answer pair with GPT-5-mini, grounded in the reports provided by the dataset. The exact prompt, with {context} substituted per image, is shown below.

Open-ended QA generation prompt

```
You are creating one open-ended visual-question-answering example for
↪  a medical imaging dataset. The question must NOT be answerable
↪  with a simple yes/no.

Ground-truth clinical context for this image (the only information you
↪  may use): {context}

Generate ONE clinically plausible open-ended question a clinician
↪  might ask about this image, and a medically accurate answer, both
↪  strictly grounded in the provided context. The questions should be
↪  able to answer from image only, but not based on other information
↪  such as medical history or results of other tests which may appear
↪  in the context. Remember when people are trying to answer the
↪  questions you provide, they do not have access to any other
↪  information except for the image -- in particular, do NOT ask
↪  about interval change, comparison to a prior exam, or whether a
↪  finding is new/stable/unchanged/resolved/improved/worsened, since
↪  no prior image is available to compare against, only this single
↪  one. The question and answer to it should be concise (within 20
↪  words).

Respond with ONLY a JSON object: {"question": "<question>", "answer":
↪  "<answer>"}
```

Model responses are scored by GPT-5-mini as follows. Rather than asking the judge for a single holistic score, we decompose the judgment into the 5-item yes/no checklist shown below, covering core-finding match, absence of contradiction, level of detail, relevance, and clinical helpfulness. LLM-judge Score is the fraction of the 5 items answered "yes". This checklist decomposition is intended to make the judge's decision more consistent and interpretable than a single 1–10 rating, following prior work (Pereira et al., 2024). Specifically, we use the following prompt to score each response.

Open-ended QA judge prompt

```
We would like to request your feedback on the performance of an AI
↪  assistant in response to the user question given below. The user
↪  asks the question on observing
an image.

Question: {question}
Reference (correct) answer: {reference}
Model's answer: {prediction}

Answer each of the following checklist questions about the model's
↪  answer with strictly "yes" or "no" (judging against the reference
↪  answer, not writing style):

1. Does the prediction hit at least one core finding from the
↪  reference (synonyms or directionally consistent terms count)?

2. Does the prediction avoid explicitly negating or directly
↪  contradicting a finding stated in the reference?

3. Does the prediction cover most clinically significant findings in
↪  the reference, without omitting a key finding that would change
↪  the diagnostic direction?
```

```
4. Does the category of information given match what the question asks
↪  for (e.g., disease diagnosis vs. technical assessment)?

5. Is the answer specific and concrete enough to inform the next
↪  clinical step, rather than vague or generic?

Respond with ONLY a JSON object of the form:
{"core_finding_match": <"yes" or "no">, "no_contradiction": <"yes" or
↪  "no">, "level_of_detail": <"yes" or "no">, "relevance": <"yes" or
↪  "no">, "helpfulness": <"yes" or "no">, "rationale": "<one sentence
↪  explanation>"}
```

Report generation with GREEN. For report generation we adapt the GREEN scoring design (Ostmeier et al., 2024): the LLM judge is asked to enumerate clinically significant errors, grouped into four categories (false finding, missed finding, wrong anatomic location, wrong severity), and to separately list matched findings, shown below. We compute $\texttt{GREEN} = n_{\text{matched}}/(n_{\text{matched}} + n_{\text{errors}})$ from the parsed counts, adapting the original chest-X-ray-specific GREEN prompt to our general medical report-writing setting.

Report generation judge prompt

```
Objective: Evaluate the accuracy of a candidate medical report in
↪  comparison to a reference report composed by experts.

Process Overview:
You will be presented with:
1. The criteria for making a judgment.
2. The reference report.
3. The candidate report.
4. The desired format for your assessment.

1. Criteria for Judgment:
For each candidate report, determine the count of clinically
↪  significant errors.
Errors can fall into one of these categories:
a) False report of a finding in the candidate.
b) Missing a finding present in the reference.
c) Misidentification of a finding's anatomic location/position.
d) Misassessment of the severity of a finding.

Note: Concentrate on the clinical findings rather than the report's
↪  writing style. Evaluate only the findings that appear in both
↪  reports. Ignore any comparisons to prior studies mentioned in the
↪  reference report, and ignore any other information that cannot be
↪  observed from a single image (e.g. clinical history, prior exams).

2. Reference Report:
{reference}

3. Candidate Report:
{prediction}

4. Reporting Your Assessment:
Follow this specific format for your output, even if no errors are
↪  found:
```
[Clinically Significant Errors]:
(a) <Error Type>: <The number of errors>. <Error 1>; <Error 2>; ...;
↪ <Error n>
....
(d) <Error Type>: <The number of errors>. <Error 1>; <Error 2>; ...;
↪ <Error n>
[Matched Findings]:
```
```

```
<The number of matched findings>. <Finding 1>; <Finding 2>; ...;
↪  <Finding n>
```

D.4 Implementation details

Every model is fine-tuned with Low-Rank Adaptation (LoRA) (Hu et al., 2022) for one epoch on a single training set that pools all task types for that dataset, using plain AdamW at a learning rate of 2×10^{-5}, LoRA rank $r = 32$, LoRA $\alpha = 16$, LoRA dropout 0.1, and gradient-norm clipping at 1.0. LoRA adapters target every attention and MLP projection layer; the vision tower and multimodal projector are kept frozen throughout. The batch size is 32, identical across all models and datasets, and these hyperparameters are fixed across all 8 architectures and all 8 datasets. Evaluation is performed with vLLM where supported and with Hugging Face Transformers otherwise; vLLM is used for LLaVA-1.5, Gemma-3-4B, MedGemma-4B, Qwen2.5-VL-7B, and InternVL3-8B. Training and evaluation are run on A100 GPUs.

Fairness-aware fine-tuning algorithms ATTRIBUTE INVARIANT and REWEIGHT otherwise use the same LoRA setup above; both group by the full intersection of a dataset's sensitive attributes. ATTRIBUTE INVARIANT penalizes a CLUB (Contrastive Log-ratio Upper Bound) estimate of the mutual information between the sensitive attribute and a representation pooled over the image-token positions of the LLM backbone's middle decoder layer (50% network depth), L2-normalized before pooling. The training objective is $\mathcal{L} = w_{\text{ce}}\mathcal{L}_{\text{ce}} + w_{\text{fair}}\big(w_{\text{mi}}\mathcal{L}_{\text{mi}} + w_{\text{club}}\mathcal{L}_{\text{club}}\big)$, with $w_{\text{ce}} = 1$, $w_{\text{fair}} = 1$, $w_{\text{club}} = 1$, $w_{\text{mi}} = 0.5$. REWEIGHT assigns each group g a fixed weight $w_g = n/\big(|\mathcal{G}| \cdot \max(n_g,\, 0.5\, n/|\mathcal{G}|)\big)$, where n is the training-set size, $|\mathcal{G}|$ the number of groups, and n_g group g's count.

E Additional Results

E.1 Fairness in zero-shot settings

Fig. 6–23 present complete per-model, per-group zero-shot results, with bootstrap 95% confidence intervals with $N = 3{,}000$ resamples, for every (dataset, task) case, with one figure per case and one column per attribute. The results show that most models exhibit a significant performance disparity, although the favored group is not always consistent across models. Besides, zero-shot performance is often low, since the evaluated datasets are not necessarily part of the pretraining data.

Table 4 shows that every model exhibits unfairness: for each (dataset, task, attribute) cell, we run a bootstrapping (95% CI excludes zero, $N = 3{,}000$ resamples) on that model's utility values across groups. Every model shows a significant utility disparity in at least 36% of its zero-shot cells, indicating that unfairness is not confined to a small subset of models.

Table 5 instead measures whether the favored group is consistent across models for each case. For each cell, we collect every zero-shot model's group-wise utility and apply a paired t-test against zero, with one paired observation per model. Cells report the p-value; shaded cells are significant at $p < 0.05$, and – marks a cell where the attribute or task type does not exist for that dataset. Only 34% of testable cells are significant. Taken together with Table 4, this shows that although every model exhibits some degree of unfairness, the favored group is inconsistent across models in most cases.

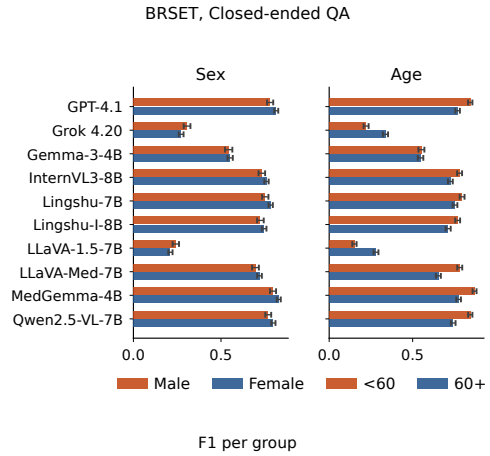

Figure 6: Per-model, per-group zero-shot utility on BRSET, Closed-ended QA, across all attributes, with bootstrap 95% confidence intervals.

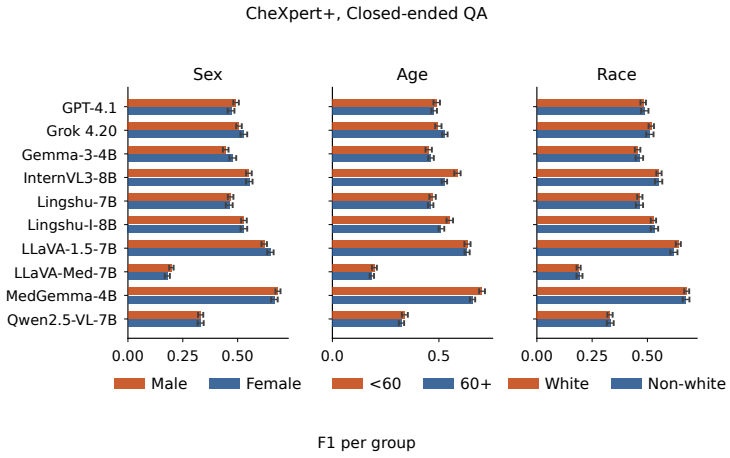

Figure 7: Per-model, per-group zero-shot utility on CheXpert Plus, Closed-ended QA, across all attributes, with bootstrap 95% confidence intervals.

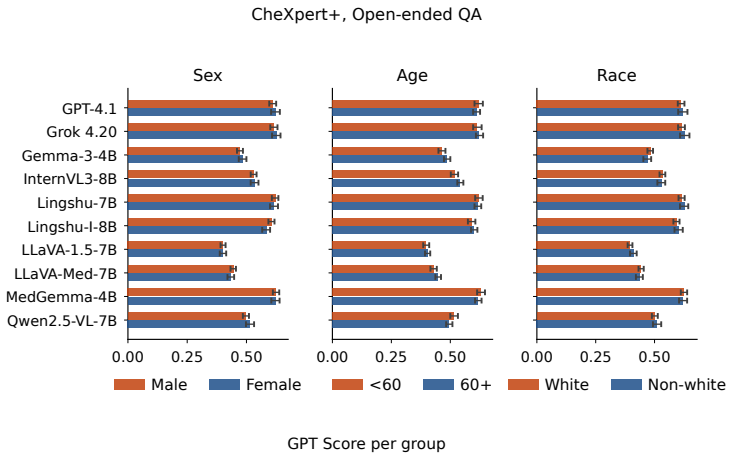

Figure 8: Per-model, per-group zero-shot utility on CheXpert Plus, Open-ended QA, across all attributes, with bootstrap 95% confidence intervals.

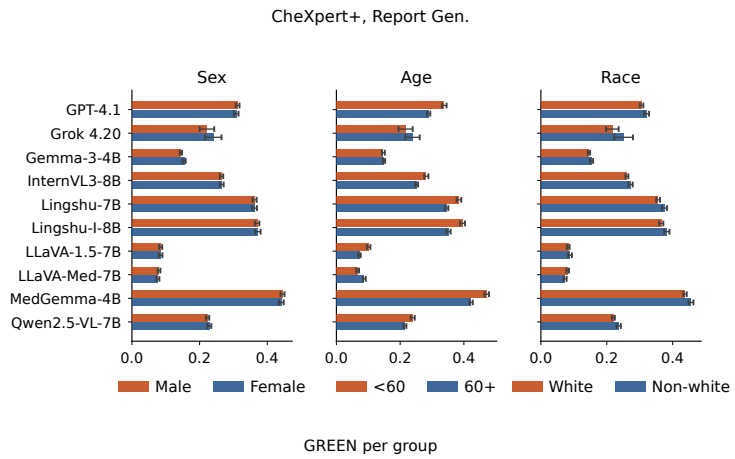

Figure 9: Per-model, per-group zero-shot utility on CheXpert Plus, Report Generation, across all attributes, with bootstrap 95% confidence intervals.

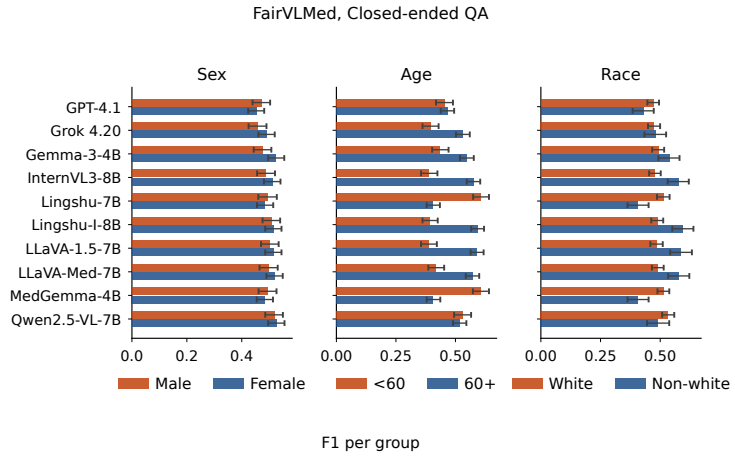

Figure 10: Per-model, per-group zero-shot utility on FairVLMed, Closed-ended QA, across all attributes, with bootstrap 95% confidence intervals.

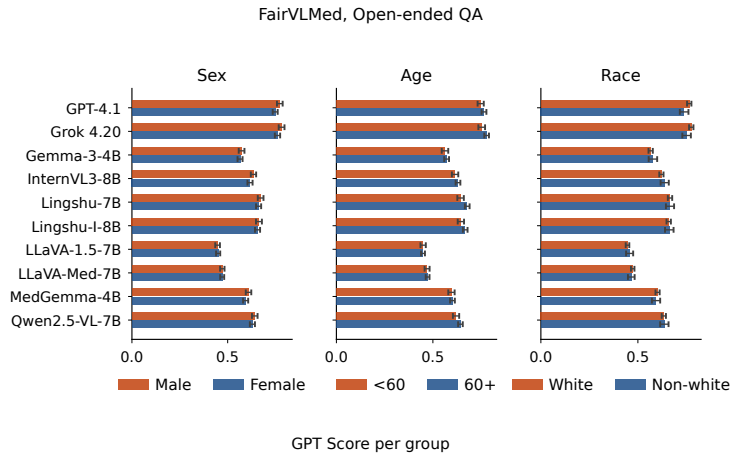

Figure 11: Per-model, per-group zero-shot utility on FairVLMed, Open-ended QA, across all attributes, with bootstrap 95% confidence intervals.

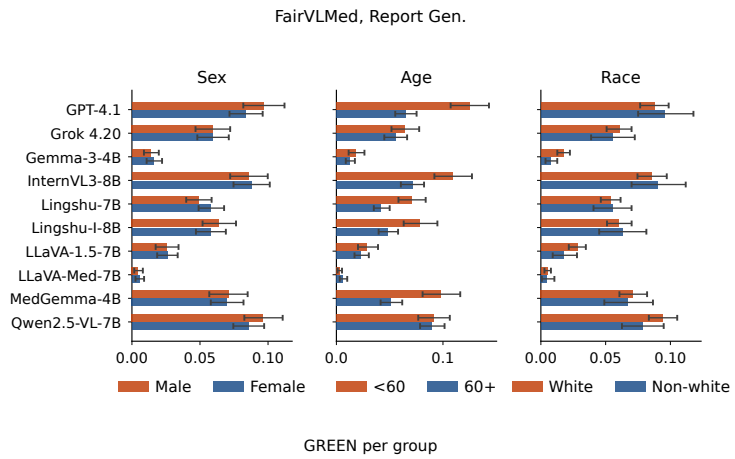

Figure 12: Per-model, per-group zero-shot utility on FairVLMed, Report Generation, across all attributes, with bootstrap 95% confidence intervals.

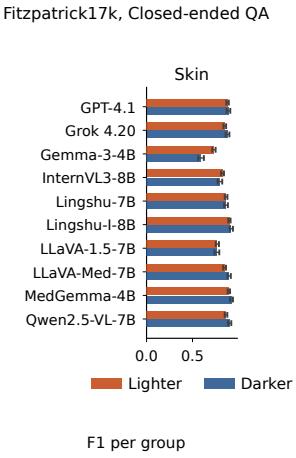

Figure 13: Per-model, per-group zero-shot utility on Fitzpatrick17k, Closed-ended QA, across all attributes, with bootstrap 95% confidence intervals.

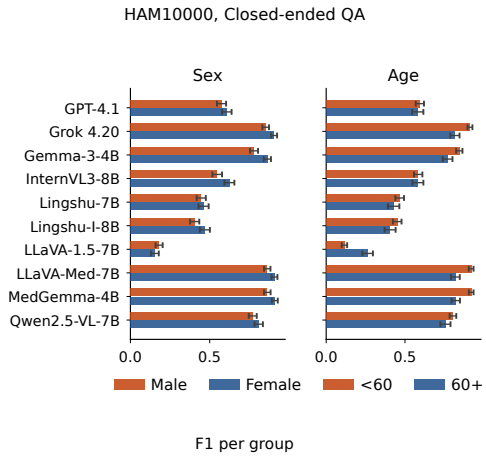

Figure 14: Per-model, per-group zero-shot utility on HAM10000, Closed-ended QA, across all attributes, with bootstrap 95% confidence intervals.



Figure 15: Per-model, per-group zero-shot utility on Merlin CT, Closed-ended QA, across all attributes, with bootstrap 95% confidence intervals.



Figure 16: Per-model, per-group zero-shot utility on Merlin CT, Open-ended QA, across all attributes, with bootstrap 95% confidence intervals.

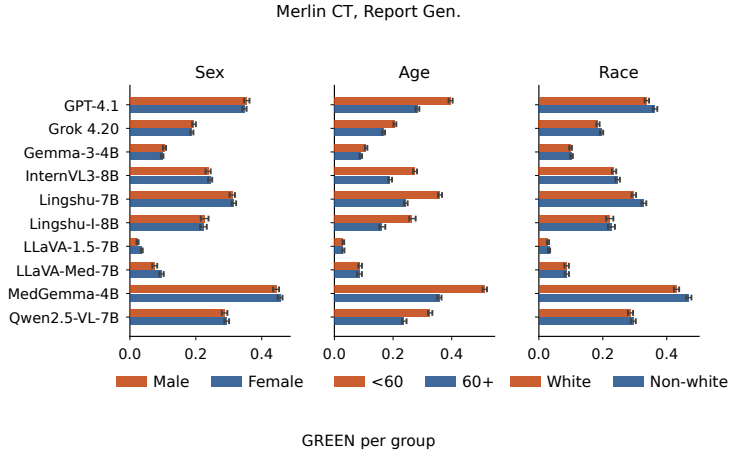

Figure 17: Per-model, per-group zero-shot utility on Merlin CT, Report Generation, across all attributes, with bootstrap 95% confidence intervals.

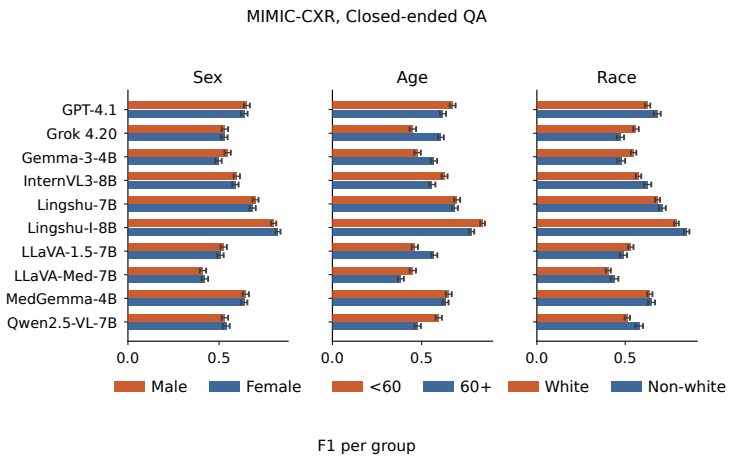

Figure 18: Per-model, per-group zero-shot utility on MIMIC-CXR, Closed-ended QA, across all attributes, with bootstrap 95% confidence intervals.

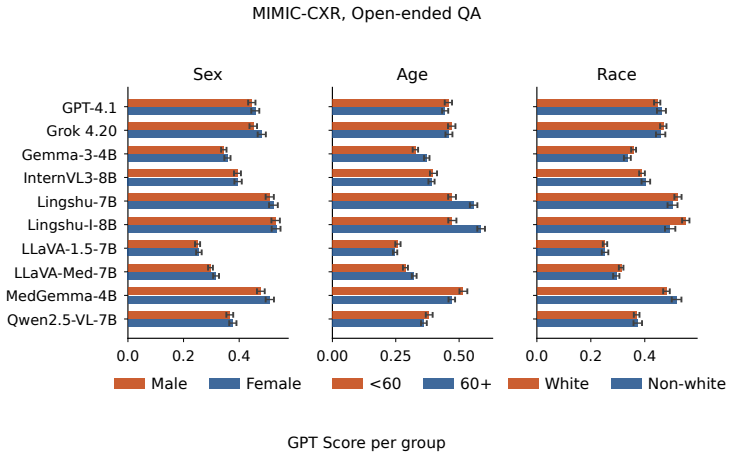

Figure 19: Per-model, per-group zero-shot utility on MIMIC-CXR, Open-ended QA, across all attributes, with bootstrap 95% confidence intervals.

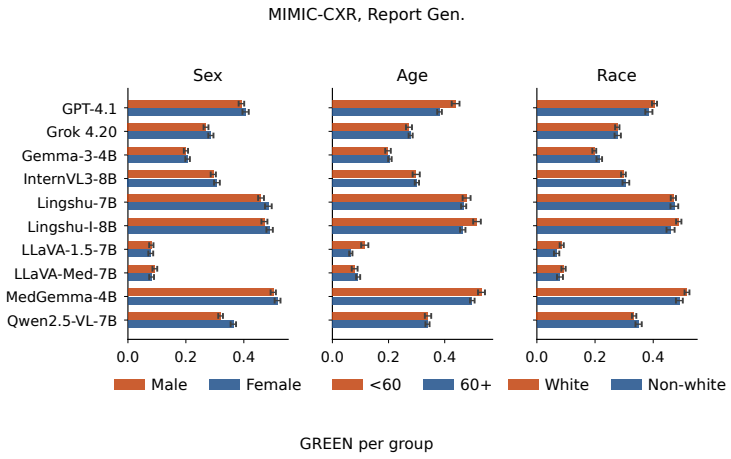

Figure 20: Per-model, per-group zero-shot utility on MIMIC-CXR, Report Generation, across all attributes, with bootstrap 95% confidence intervals.

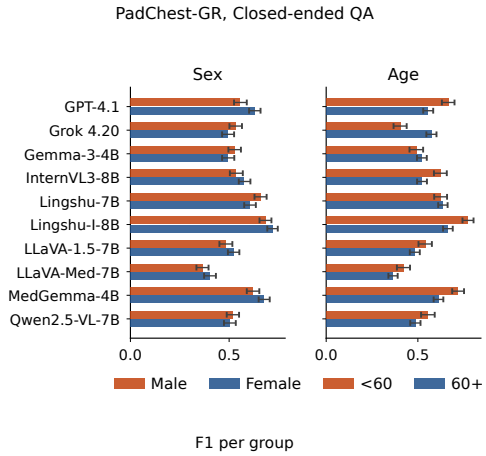

Figure 21: Per-model, per-group zero-shot utility on PadChest-GR, Closed-ended QA, across all attributes, with bootstrap 95% confidence intervals.

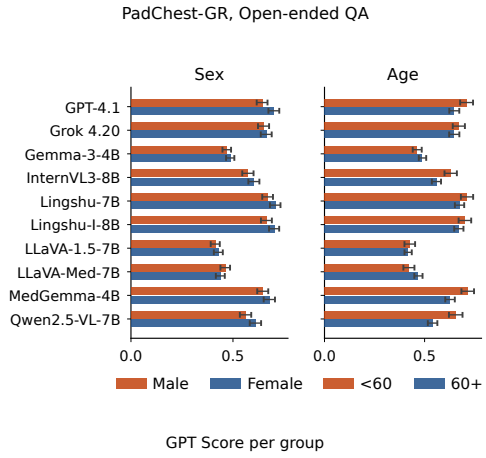

Figure 22: Per-model, per-group zero-shot utility on PadChest-GR, Open-ended QA, across all attributes, with bootstrap 95% confidence intervals.

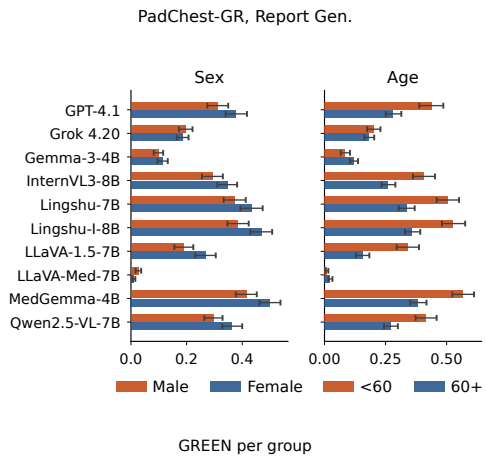

Figure 23: Per-model, per-group zero-shot utility on PadChest-GR, Report Generation, across all attributes, with bootstrap 95% confidence intervals.

Model	Ratio
Lingshu-I-8B	57.4%
MedGemma-4B	55.3%
LLaVA-Med-7B	51.1%
GPT-4.1	46.8%
Qwen2.5-VL-7B	44.7%
InternVL3-8B	42.6%
Lingshu-7B	42.6%
Grok-4-20	40.4%
Gemma-3-4B	40.4%
LLaVA-1.5-7B	36.2%

Table 4: Fraction of (dataset, task, attribute) cells with a significant within-model gap in zero-shot settings (bootstrapping on the group-wise utility difference, 95% CI excludes zero, $N = 3{,}000$ resamples), per model.

Dataset	Closed-ended QA				Open-ended QA				Report Generation			
	Sex	Age	Race	Skin	Sex	Age	Race	Skin	Sex	Age	Race	Skin
BRSET	0.041	0.341	–	–	–	–	–	–	–	–	–	–
CheXpert Plus	0.655	0.026	0.368	–	0.740	0.245	0.515	–	0.283	0.041	0.007	–
FairVLMed	0.132	0.446	0.501	–	0.343	<0.001	0.008	–	0.080	0.016	0.531	–
Fitzpatrick17k	–	–	–	0.726	–	–	–	–	–	–	–	–
HAM10000	0.353	0.415	–	–	–	–	–	–	–	–	–	–
Merlin CT	0.091	0.472	0.993	–	0.465	0.011	0.938	–	0.048	0.008	0.008	–
MIMIC-CXR	0.308	0.983	0.505	–	0.095	0.076	0.059	–	0.022	0.028	0.344	–
PadChest-GR	0.158	0.062	–	–	0.007	0.088	–	–	0.004	0.003	–	–

Table 5: Group disparity under zero-shot evaluation. For each cell we collect each zero-shot model's group-wise utility and apply a paired t-test against zero, one paired observation per model. Cells report the p-value; shaded cells are significant at $p < 0.05$, and – marks cells where the attribute or task type does not exist for that dataset. 34% testable cells are significant.

E.2 FAIRNESS IN FINE-TUNED SETTINGS

Fig. 24–41 present complete per-model, per-group fine-tuned results (bootstrap 95% confidence intervals with $N = 3{,}000$ resamples) for every (dataset, task) case, with one figure per case and one column per attribute. Each caption additionally reports whether every fine-tuned model happens to favor the same group on a given attribute, judged by mean utility.

Table 6 shows that fine-tuning increases the prevalence of unfairness within every model: each of the 8 fine-tuned architectures now shows a significant utility disparity in at least 49% of its (dataset, task, attribute) cells, compared with at least 36% before fine-tuning (Table 4).

Table 7 measures whether the favored group is consistent across models for each case, using the same paired t-test as Table 5. Here, 74% of testable cells are significant, more than the 34% observed in the zero-shot setting. Because every architecture is fine-tuned on the same in-domain data, this increase indicates that fine-tuning mitigates the disparate pretraining backgrounds responsible for the zero-shot grid's inconsistent favored group, and replaces them with a shared bias pattern on each dataset across models.

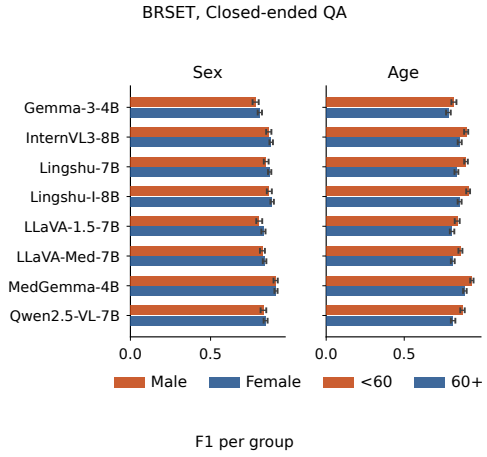

Figure 24: Per-model, per-group fine-tuned utility on BRSET, Closed-ended QA, across all attributes, with bootstrap 95% confidence intervals. All models favor `Female` on `Sex`; all models favor `<60` on `Age`.

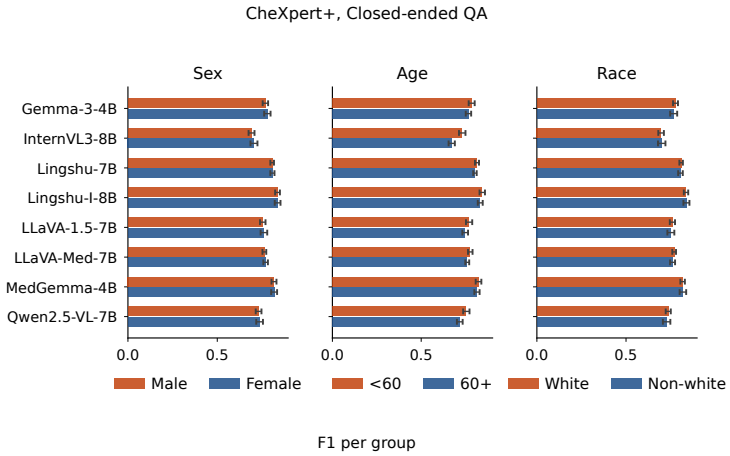

Figure 25: Per-model, per-group fine-tuned utility on CheXpert Plus, Closed-ended QA, across all attributes, with bootstrap 95% confidence intervals. All models favor `Female` on `Sex`; all models favor `<60` on `Age`.

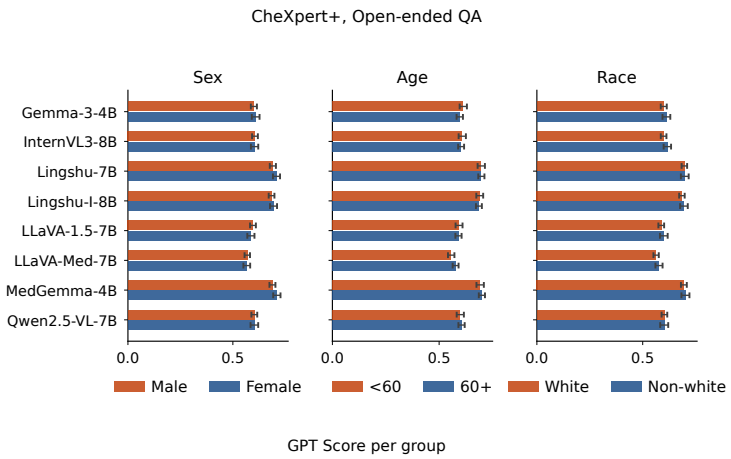

Figure 26: Per-model, per-group fine-tuned utility on CheXpert Plus, Open-ended QA, across all attributes, with bootstrap 95% confidence intervals.



Figure 27: Per-model, per-group fine-tuned utility on CheXpert Plus, Report Generation, across all attributes, with bootstrap 95% confidence intervals.

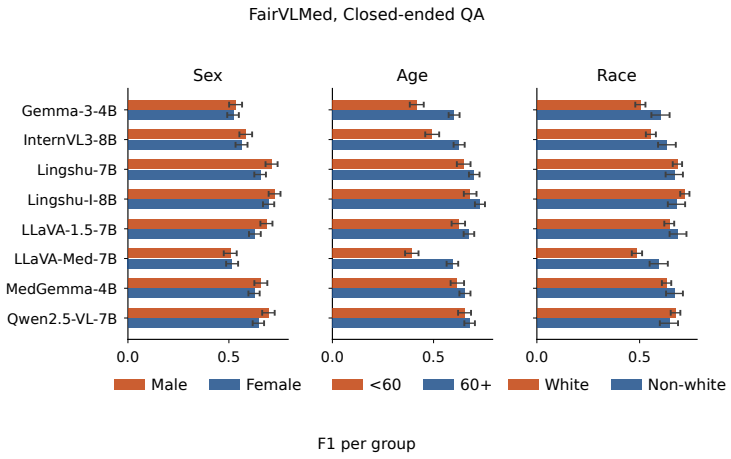

Figure 28: Per-model, per-group fine-tuned utility on FairVLMed, Closed-ended QA, across all attributes, with bootstrap 95% confidence intervals. All models favor `60+` on `Age`.

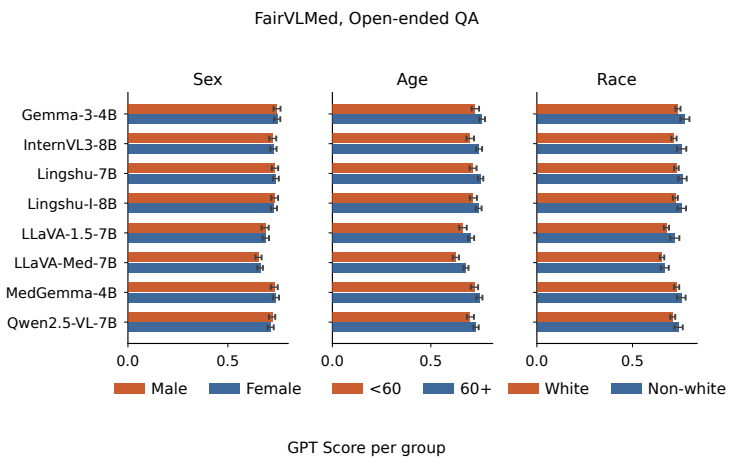

Figure 29: Per-model, per-group fine-tuned utility on FairVLMed, Open-ended QA, across all attributes, with bootstrap 95% confidence intervals. All models favor `60+` on `Age`; all models favor `Non-white` on `Race`.

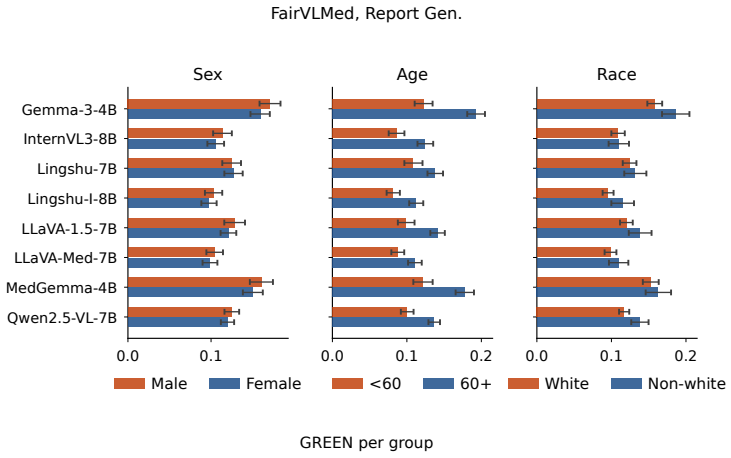

Figure 30: Per-model, per-group fine-tuned utility on FairVLMed, Report Generation, across all attributes, with bootstrap 95% confidence intervals. All models favor `60+` on `Age`; all models favor `Non-white` on `Race`.

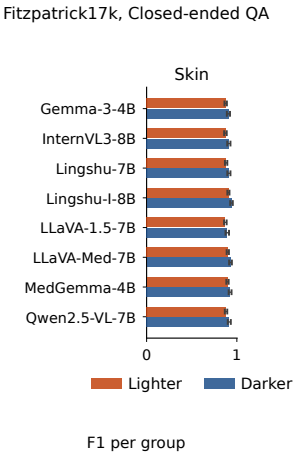

Figure 31: Per-model, per-group fine-tuned utility on Fitzpatrick17k, Closed-ended QA, across all attributes, with bootstrap 95% confidence intervals. All models favor `Darker` on `Skin`.

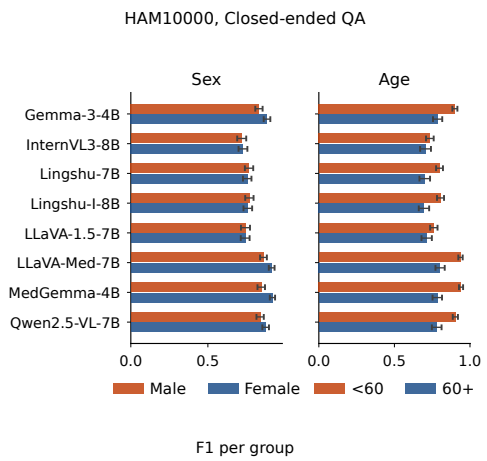

Figure 32: Per-model, per-group fine-tuned utility on HAM10000, Closed-ended QA, across all attributes, with bootstrap 95% confidence intervals. All models favor `<60` on `Age`.



Figure 33: Per-model, per-group fine-tuned utility on Merlin CT, Closed-ended QA, across all attributes, with bootstrap 95% confidence intervals. All models favor `<60` on `Age`; all models favor `Non-white` on `Race`.



Figure 34: Per-model, per-group fine-tuned utility on Merlin CT, Open-ended QA, across all attributes, with bootstrap 95% confidence intervals. All models favor `Female` on `Sex`; all models favor `<60` on `Age`.

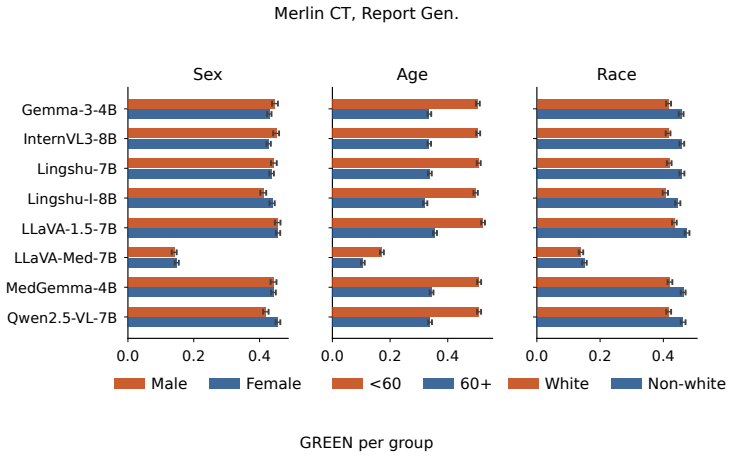

Figure 35: Per-model, per-group fine-tuned utility on Merlin CT, Report Generation, across all attributes, with bootstrap 95% confidence intervals. All models favor `<60` on `Age`; all models favor `Non-white` on `Race`.



Figure 36: Per-model, per-group fine-tuned utility on MIMIC-CXR, Closed-ended QA, across all attributes, with bootstrap 95% confidence intervals. All models favor `<60` on `Age`; all models favor `Non-white` on `Race`.

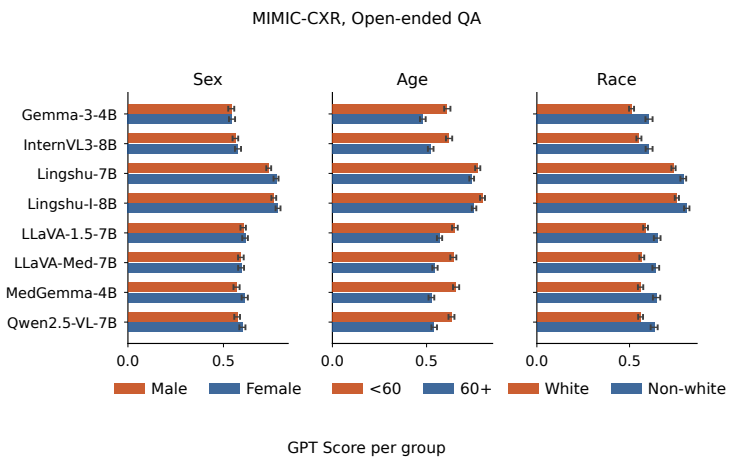

Figure 37: Per-model, per-group fine-tuned utility on MIMIC-CXR, Open-ended QA, across all attributes, with bootstrap 95% confidence intervals. All models favor `Female` on `Sex`; all models favor `<60` on `Age`; all models favor `Non-white` on `Race`.



Figure 38: Per-model, per-group fine-tuned utility on MIMIC-CXR, Report Generation, across all attributes, with bootstrap 95% confidence intervals. All models favor `<60` on `Age`; all models favor `White` on `Race`.

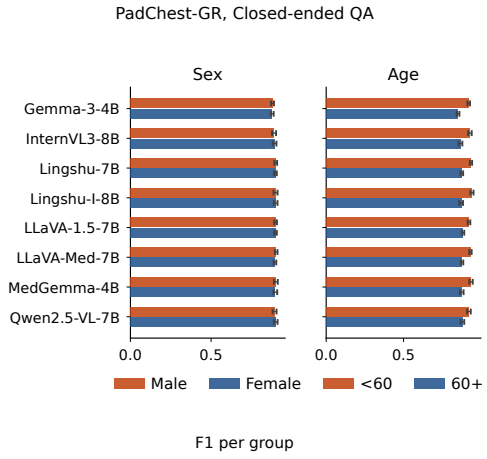

Figure 39: Per-model, per-group fine-tuned utility on PadChest-GR, Closed-ended QA, across all attributes, with bootstrap 95% confidence intervals. All models favor `<60` on `Age`.

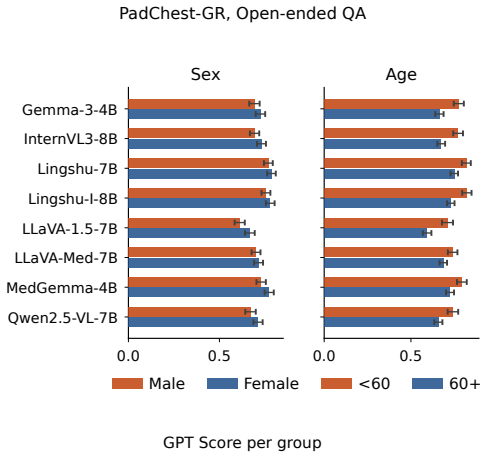

Figure 40: Per-model, per-group fine-tuned utility on PadChest-GR, Open-ended QA, across all attributes, with bootstrap 95% confidence intervals. All models favor `Female` on `Sex`; all models favor `<60` on `Age`.

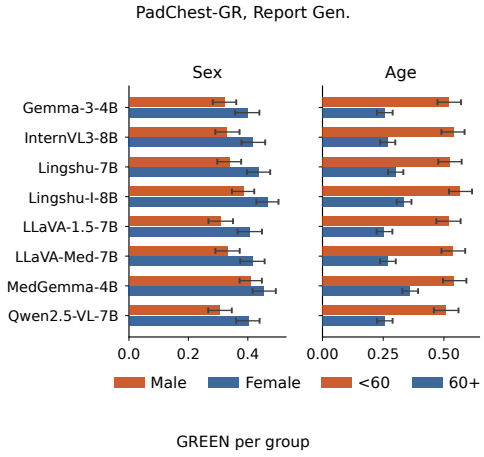

Figure 41: Per-model, per-group fine-tuned utility on PadChest-GR, Report Generation, across all attributes, with bootstrap 95% confidence intervals. All models favor `Female` on `Sex`; all models favor `<60` on `Age`.

Model	Ratio
Qwen2.5-VL-7B	63.8%
Gemma-3-4B	59.6%
Lingshu-7B	55.3%
InternVL3-8B	55.3%
Lingshu-I-8B	55.3%
LLaVA-1.5-7B	53.2%
LLaVA-Med-7B	51.1%
MedGemma-4B	48.9%

Table 6: Fine-tuned: fraction of testable (dataset, task, attribute) cells with a significant within-model gap (bootstrapping on the group-wise utility difference, 95% CI excludes zero, $N = 3{,}000$ resamples), per model.

Dataset	Closed-ended QA				Open-ended QA				Report Generation			
	Sex	Age	Race	Skin	Sex	Age	Race	Skin	Sex	Age	Race	Skin
BRSET	<0.001	<0.001	–	–	–	–	–	–	–	–	–	–
CheXpert Plus	0.011	0.006	0.108	–	0.219	0.804	0.004	–	0.001	0.006	0.036	–
FairVLMed	0.006	0.008	0.132	–	0.307	<0.001	<0.001	–	0.002	<0.001	0.002	–
Fitzpatrick17k	–	–	–	<0.001	–	–	–	–	–	–	–	–
HAM10000	0.071	<0.001	–	–	–	–	–	–	–	–	–	–
Merlin CT	0.083	<0.001	<0.001	–	0.004	0.002	0.059	–	0.664	<0.001	<0.001	–
MIMIC-CXR	0.059	<0.001	<0.001	–	0.008	<0.001	<0.001	–	0.570	<0.001	<0.001	–
PadChest-GR	0.783	<0.001	–	–	<0.001	<0.001	–	–	<0.001	<0.001	–	–

Table 7: Prevalence of group disparity after fine-tuning. For each dataset, task type, and sensitive attribute, we collect the group-wise utility metrics from all models fine-tuned on that dataset and apply a paired t-test (the group-wise utility difference against zero, one paired observation per model) to assess whether one group is favored consistently across models. Cells report the p-value; shaded cells are significant at $p < 0.05$. Cells are marked – when they do not exist, either because the dataset lacks the attribute or because the task type was not built for that dataset.

E.3 BIAS SOURCES AND FAIRNESS

Complete version of Fig. 3: every task type and every sensitive attribute for each dataset (Fitzpatrick17k excluded, since it carries only `skin_type` and has no other attribute to compare). Each figure corresponds to one dataset; each sub-figure is one task type, showing all of that dataset's attributes together (top: per-attribute utility gap; bottom: the five bias sources per attribute), ranked and colored largest-gap-first. Table 2 reports this relationship in aggregate, where individual bias sources correlate positively with the utility gap; the per-setting view here shows that this ordering is not exact case by case, with different bias sources contributing unevenly to the gap across individual (dataset, task, attribute) settings.

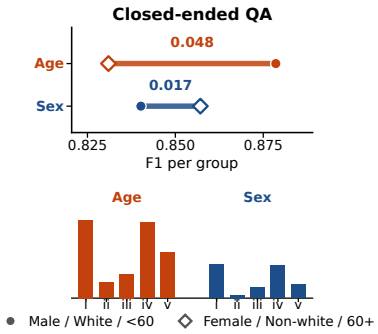

Figure 42: Per-group utility gap (Top) and bias sources (Bottom) of BRSET.

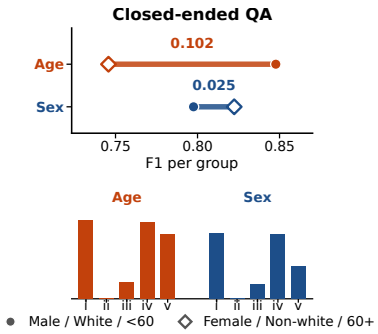

Figure 43: Per-group utility gap (Top) and bias sources (Bottom) of HAM10000.

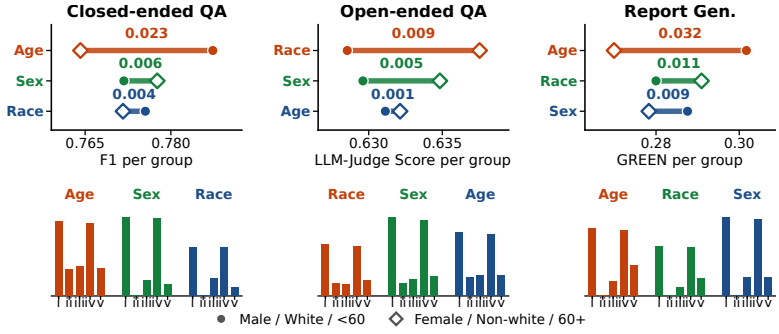

Figure 44: Per-group utility gap (Top) and bias sources (Bottom) of CheXpert Plus.

Sensitivity to the choice of vision encoder. Every bias source above is estimated on frozen CLIP ViT-B/32 embeddings for Z_v (Section 3.3). To check the sensitivity of our observation to the choice of encoder, we recompute the five sources with BiomedCLIP (Zhang et al., 2023) in place of CLIP on all eight datasets, and correlate each source with the utility gap the same way, pooled across

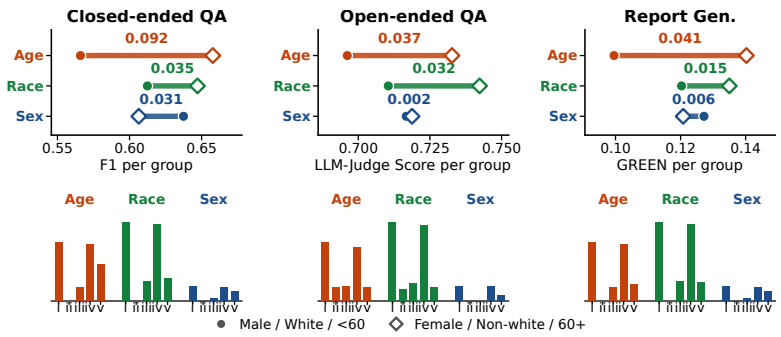

Figure 45: Per-group utility gap (Top) and bias sources (Bottom) of FairVLMed.

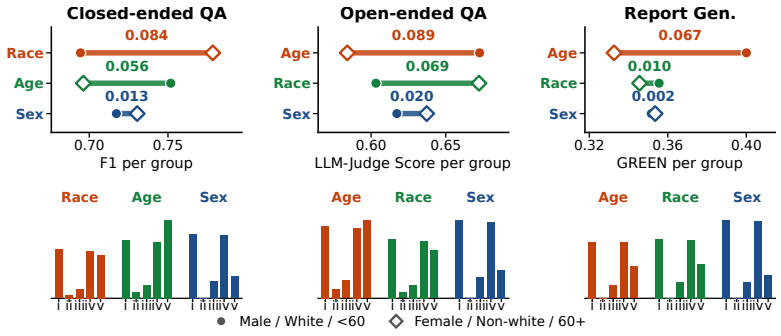

Figure 46: Per-group utility gap (Top) and bias sources (Bottom) of MIMIC-CXR.

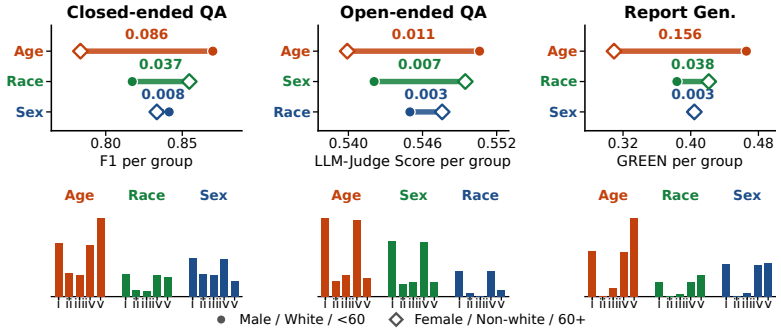

Figure 47: Per-group utility gap (Top) and bias sources (Bottom) of Merlin CT.

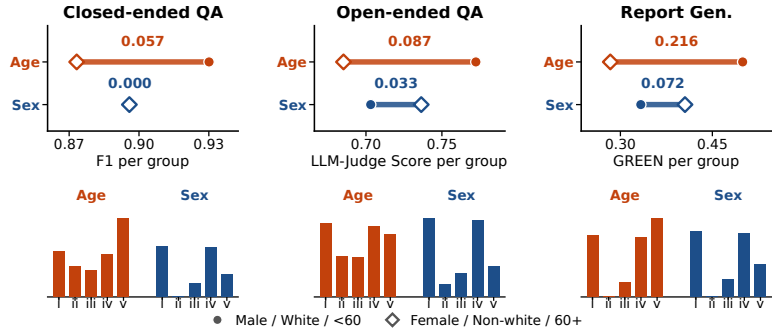

Figure 48: Per-group utility gap (Top) and bias sources (Bottom) of PadChest-GR.

datasets, attributes, and models within each task. Table 8 shows the two encoders agree closely and reproduce a pattern very similar to Table 2: source (v) remains the strongest and most consistent predictor under both encoders in every task, and open-ended QA shows the strongest correlations of the three tasks under either encoder.

Task	Encoder	(i)	(ii)	(iii)	(iv)	(v)
Closed-ended QA ($n = 152$)	CLIP ViT-B/32	0.32	0.28	0.24	0.33	0.71
	BiomedCLIP	0.35	0.32	0.16	0.36	0.71
Open-ended QA ($n = 112$)	CLIP ViT-B/32	0.61	0.36	0.65	0.61	0.81
	BiomedCLIP	0.62	0.36	0.65	0.62	0.81
Report Generation ($n = 112$)	CLIP ViT-B/32	0.23	−0.13	0.16	0.23	0.57
	BiomedCLIP	0.39	−0.12	0.49	0.39	0.58

Table 8: Spearman ρ between the utility gap and each source of bias, CLIP ViT-B/32 vs. BiomedCLIP as the encoder, pooled across datasets, models, and attributes within each task.

E.4 FAIRNESS-MITIGATION METHODS

In this section, we present utility and fairness results of models finetuned with two fairness-mitigation methods: ATTRIBUTE INVARIANT (introducing attribute-invariant mutual-information penalty) and REWEIGHT (group reweighting of the training loss), and compare each against that same backbone's own VANILLA checkpoint without fairness mitigation. Tables 9–16 (one per dataset) report the absolute change (Δ) in utility and utility gap compared with vanilla. For every setting, the change is computed per backbone against that backbone's own vanilla number, then averaged across all models, with a paired Wilcoxon signed-rank test (Okoye & Hosseini, 2024) (one pair per model, against zero change) marking which cells are statistically significant. VANILLA rows report the actual value; ATTRIBUTE INVARIANT and REWEIGHT rows report the mean change from that model's own vanilla baseline, blue for a positive change and red for a negative one, and **bold** when significant at $p < 0.05$. Utility (↑) is better higher; Utility Gap (↓) is measured by the absolute value of utility gap, better lower. Results show that neither method mitigates the utility gap consistently.

Task	Attribute	VANILLA		ATTRIBUTE INVARIANT		REWEIGHT	
		Utility ↑	Utility Gap ↓	ΔUtility ↑	ΔUtility Gap ↓	ΔUtility ↑	ΔUtility Gap ↓
Closed-ended QA	Age	0.851	0.048	+0.005	-0.000	+0.002	-0.001
Closed-ended QA	Sex	0.851	0.017	+0.005	+0.001	+0.002	+0.000

Table 9: Utility and fairness results of different finetuning methods on BRSET.

Task	Attribute	VANILLA		ATTRIBUTE INVARIANT		REWEIGHT	
		Utility ↑	Utility Gap ↓	ΔUtility ↑	ΔUtility Gap ↓	ΔUtility ↑	ΔUtility Gap ↓
Closed-ended QA	Age	0.774	0.023	+0.015	-0.006	**+0.013**	-0.003
Closed-ended QA	Race	0.774	0.006	+0.015	+0.000	**+0.013**	+0.000
Closed-ended QA	Sex	0.774	0.006	+0.015	+0.001	**+0.013**	+0.003
Open-ended QA	Age	0.632	0.008	-0.000	+0.002	**-0.007**	+0.002
Open-ended QA	Race	0.632	0.009	-0.000	-0.002	**-0.007**	-0.001
Open-ended QA	Sex	0.632	0.009	-0.000	-0.001	**-0.007**	-0.002
Report Generation	Age	0.288	0.029	+0.001	+0.003	+0.001	+0.002
Report Generation	Race	0.288	0.012	+0.001	+0.003	+0.001	+0.001
Report Generation	Sex	0.288	0.009	+0.001	+0.001	+0.001	+0.002

Table 10: Utility and fairness results of different finetuning methods on CheXpert Plus.

Task	Attribute	VANILLA		ATTRIBUTE INVARIANT		REWEIGHT	
		Utility ↑	Utility Gap ↓	ΔUtility ↑	ΔUtility Gap ↓	ΔUtility ↑	ΔUtility Gap ↓
Closed-ended QA	Age	0.620	0.092	-0.029	+0.006	**-0.036**	+0.015
Closed-ended QA	Race	0.620	0.056	-0.029	+0.001	**-0.036**	+0.000
Closed-ended QA	Sex	0.620	0.033	-0.029	**-0.012**	**-0.036**	**-0.016**
Open-ended QA	Age	0.718	0.037	-0.002	+0.001	-0.002	-0.001
Open-ended QA	Race	0.718	0.032	-0.002	-0.004	-0.002	-0.003
Open-ended QA	Sex	0.718	0.005	-0.002	+0.003	-0.002	+0.001
Report Generation	Age	0.124	0.041	+0.003	+0.007	+0.006	+0.003
Report Generation	Race	0.124	0.015	+0.003	+0.000	+0.006	+0.005
Report Generation	Sex	0.124	0.007	+0.003	-0.001	+0.006	-0.001

Table 11: Utility and fairness results of different finetuning methods on FairVLMed.

Task	Attribute	VANILLA		ATTRIBUTE INVARIANT		REWEIGHT	
		Utility ↑	Utility Gap ↓	ΔUtility ↑	ΔUtility Gap ↓	ΔUtility ↑	ΔUtility Gap ↓
Closed-ended QA	Skin	0.896	0.032	+0.001	+0.001	+0.002	+0.002

Table 12: Utility and fairness results of different finetuning methods on Fitzpatrick17k.

Task	Attribute	VANILLA		ATTRIBUTE INVARIANT		REWEIGHT	
		Utility ↑	Utility Gap ↓	ΔUtility ↑	ΔUtility Gap ↓	ΔUtility ↑	ΔUtility Gap ↓
Closed-ended QA	Age	0.810	0.102	-0.002	-0.004	**-0.013**	**-0.009**
Closed-ended QA	Sex	0.810	0.031	-0.002	+0.002	**-0.013**	+0.003

Table 13: Utility and fairness results of different finetuning methods on HAM10000.

Task	Attribute	VANILLA		ATTRIBUTE INVARIANT		REWEIGHT	
		Utility ↑	Utility Gap ↓	ΔUtility ↑	ΔUtility Gap ↓	ΔUtility ↑	ΔUtility Gap ↓
Closed-ended QA	Age	0.837	0.086	+0.003	+0.002	+0.006	-0.003
Closed-ended QA	Race	0.837	0.037	+0.003	+0.003	+0.006	+0.003
Closed-ended QA	Sex	0.837	0.010	+0.003	-0.002	+0.006	+0.001
Open-ended QA	Age	0.546	0.011	**-0.004**	+0.002	**-0.004**	-0.001
Open-ended QA	Race	0.546	0.003	**-0.004**	+0.002	**-0.004**	**+0.003**
Open-ended QA	Sex	0.546	0.007	**-0.004**	-0.001	**-0.004**	-0.001
Report Generation	Age	0.393	0.151	-0.003	-0.002	**-0.005**	-0.004
Report Generation	Race	0.393	0.036	-0.003	+0.000	**-0.005**	+0.001
Report Generation	Sex	0.393	0.012	-0.003	+0.002	**-0.005**	-0.000

Table 14: Utility and fairness results of different finetuning methods on Merlin CT.

Task	Attribute	VANILLA		ATTRIBUTE INVARIANT		REWEIGHT	
		Utility ↑	Utility Gap ↓	ΔUtility ↑	ΔUtility Gap ↓	ΔUtility ↑	ΔUtility Gap ↓
Closed-ended QA	Age	0.724	0.056	+0.003	+0.001	-0.002	+0.003
Closed-ended QA	Race	0.724	0.084	+0.003	+0.002	-0.002	+0.000
Closed-ended QA	Sex	0.724	0.019	+0.003	-0.002	-0.002	-0.001
Open-ended QA	Age	0.627	0.089	+0.007	+0.001	-0.002	+0.001
Open-ended QA	Race	0.627	0.069	+0.007	+0.000	-0.002	+0.001
Open-ended QA	Sex	0.627	0.020	+0.007	+0.000	-0.002	-0.000
Report Generation	Age	0.352	0.067	-0.000	+0.006	-0.003	+0.001
Report Generation	Race	0.352	0.010	-0.000	+0.003	-0.003	+0.005
Report Generation	Sex	0.352	0.007	-0.000	+0.001	-0.003	-0.001

Table 15: Utility and fairness results of different finetuning methods on MIMIC-CXR.

Task	Attribute	VANILLA		ATTRIBUTE INVARIANT		REWEIGHT	
		Utility ↑	Utility Gap ↓	ΔUtility ↑	ΔUtility Gap ↓	ΔUtility ↑	ΔUtility Gap ↓
Closed-ended QA	Age	0.896	0.057	+0.002	-0.003	+0.002	-0.002
Closed-ended QA	Sex	0.896	0.003	+0.002	**+0.004**	+0.002	+0.001
Open-ended QA	Age	0.720	0.087	+0.002	+0.004	+0.004	**+0.005**
Open-ended QA	Sex	0.720	0.033	+0.002	-0.001	+0.004	+0.001
Report Generation	Age	0.371	0.216	+0.002	+0.017	-0.006	+0.001
Report Generation	Sex	0.371	0.072	+0.002	**+0.011**	-0.006	-0.005

Table 16: Utility and fairness results of different finetuning methods on PadChest-GR.

E.5 DISTRIBUTION-SHIFT AND FAIRNESS

Figures 49–56 show the full set of ID vs. OOD utility and fairness results for all dataset pairs, task types, and attributes. Each figure corresponds to one dataset pair and one task type; each sub-figure is one attribute, showing per-group utility (top) and the per-attribute utility gap (bottom). The $y = x$ line marks no change in utility or fairness from ID to OOD. Utility typically drops under OOD, and this direction is consistent across models most of the time. The direction of the fairness change is likewise mostly consistent across models within an attribute, but varies across attributes, indicating that the two domains' distributions shift by different amounts for different attributes. `Sex` shows a more mixed effect than the other attributes, consistent with Table 1, where `Sex` is the attribute least likely to yield a significant bias across models.

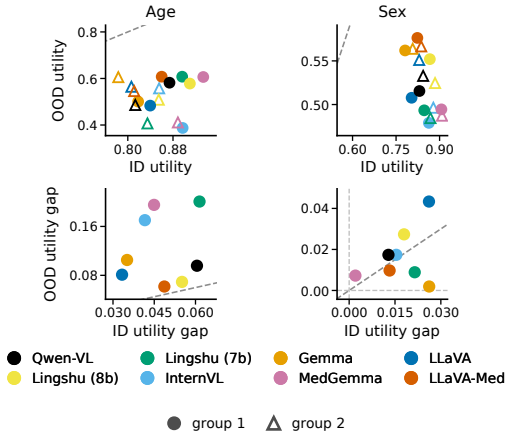

Figure 49: ID vs. OOD utility and fairness, BRSET → FairVLMed, Closed-ended QA.

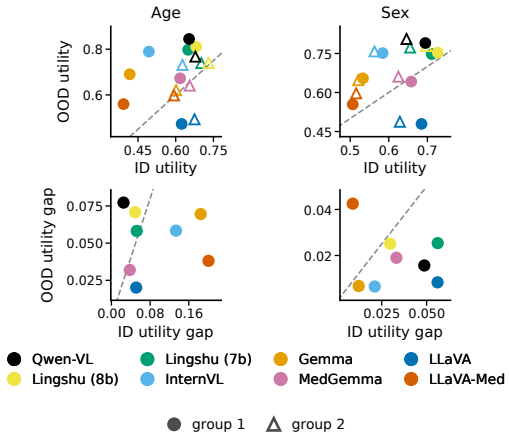

Figure 50: ID vs. OOD utility and fairness, FairVLMed → BRSET, Closed-ended QA.

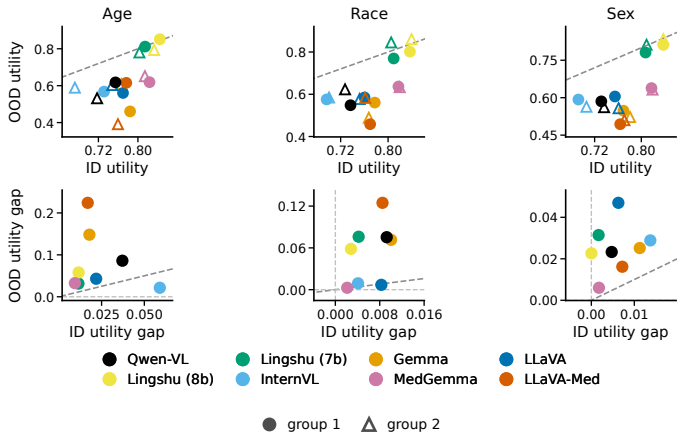

Figure 51: ID vs. OOD utility and fairness, CheXpert Plus → MIMIC-CXR, Closed-ended QA.

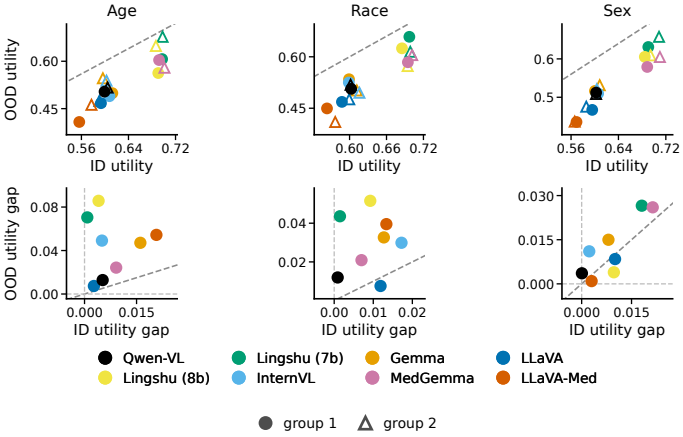

Figure 52: ID vs. OOD utility and fairness, CheXpert Plus → MIMIC-CXR, Open-ended QA.

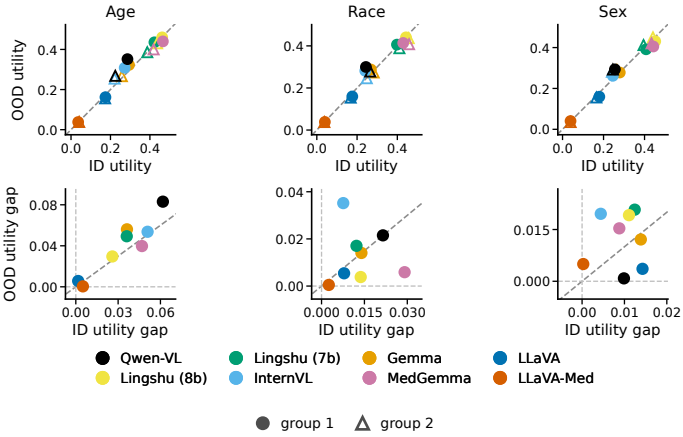

Figure 53: ID vs. OOD utility and fairness, CheXpert Plus → MIMIC-CXR, Report Generation.

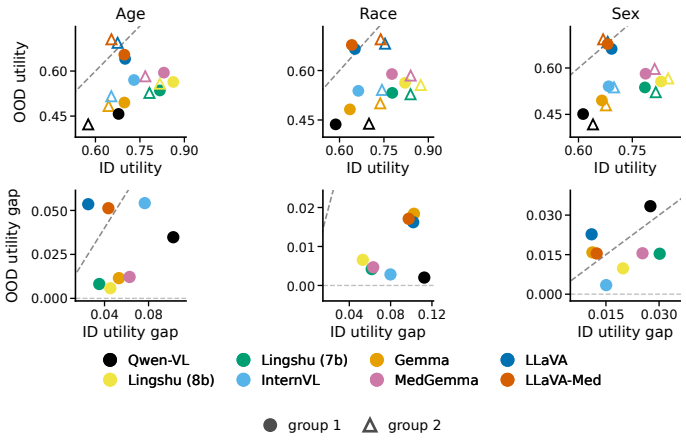

Figure 54: ID vs. OOD utility and fairness, MIMIC-CXR → CheXpert Plus, Closed-ended QA.

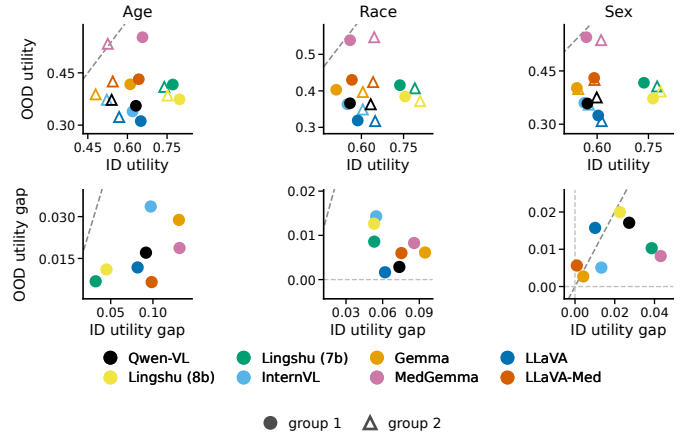

Figure 55: ID vs. OOD utility and fairness, MIMIC-CXR → CheXpert Plus, Open-ended QA.

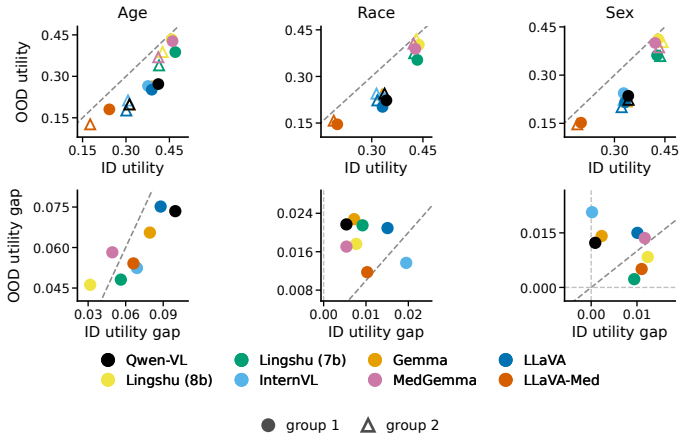

Figure 56: ID vs. OOD utility and fairness, MIMIC-CXR → CheXpert Plus, Report Generation.

E.6 OOD SOURCE AND FAIRNESS

Figures 57–64 show every (source → target, task type) pair under the OOD scenario, with one subfigure per attribute (top: the source-vs.-target utility dumbbell and the signed change per group; bottom: the five OOD sources per group). Values are taken from the best-performing model on the target dataset, to avoid noise from low target performance. The two groups usually show a similar distribution over OOD sources, indicating that the distribution shift affects both groups similarly. When the OOD sources are highly concentrated (e.g., CheXpert Plus → MIMIC-CXR, Open-ended QA), the correlation between OOD sources and the utility change is clearer, since this limits the mixed effect of the other sources.

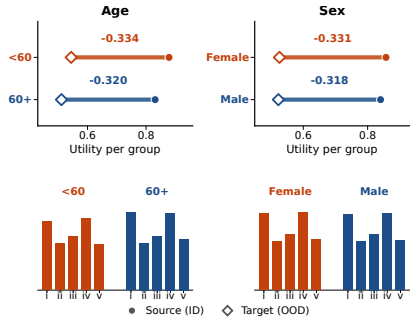

Figure 57: BRSET → FairVLMed, Closed-ended QA, utility change and OOD sources

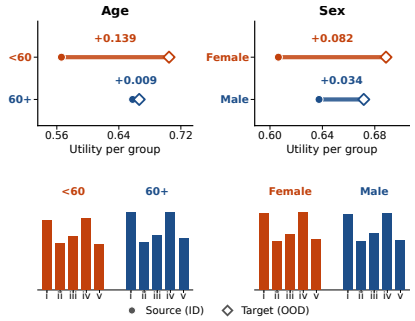

Figure 58: FairVLMed → BRSET, Closed-ended QA, utility change and OOD sources

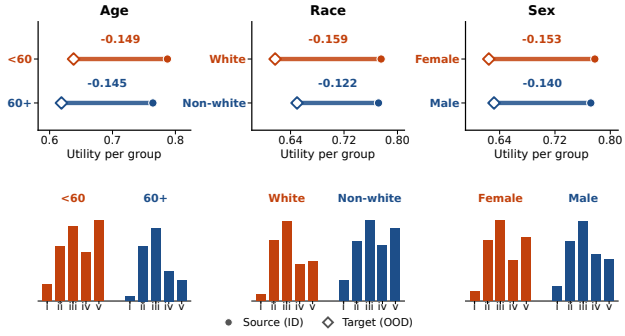

Figure 59: CheXpert Plus → MIMIC-CXR, Closed-ended QA, utility change and OOD sources

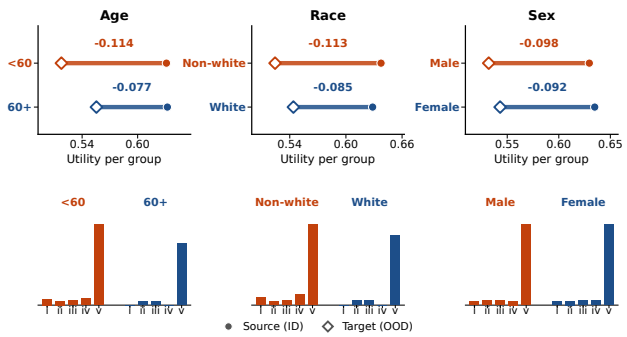

Figure 60: CheXpert Plus → MIMIC-CXR, Open-ended QA, utility change and OOD sources

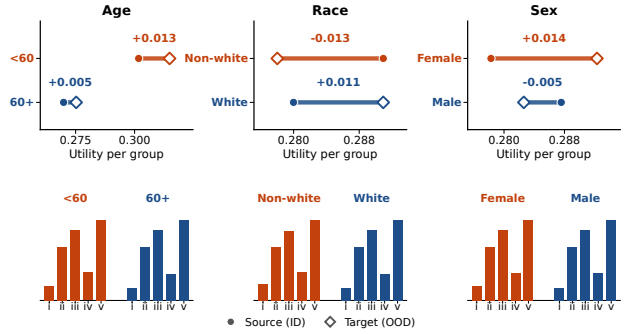

Figure 61: CheXpert Plus → MIMIC-CXR, Report Generation, utility change and OOD sources

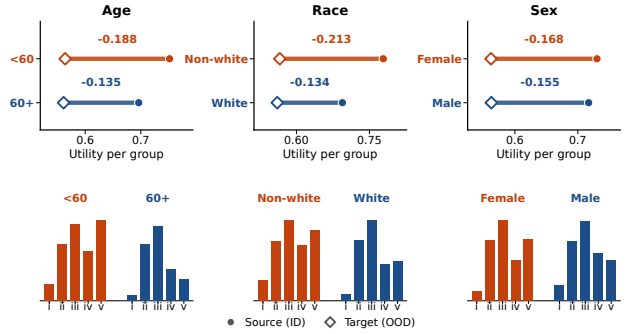

Figure 62: MIMIC-CXR → CheXpert Plus, Closed-ended QA, utility change and OOD sources

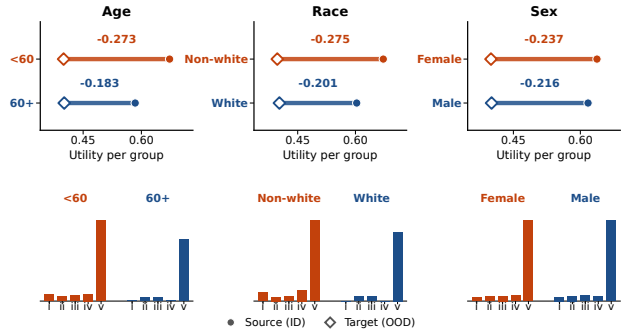

Figure 63: MIMIC-CXR → CheXpert Plus, Open-ended QA, utility change and OOD sources

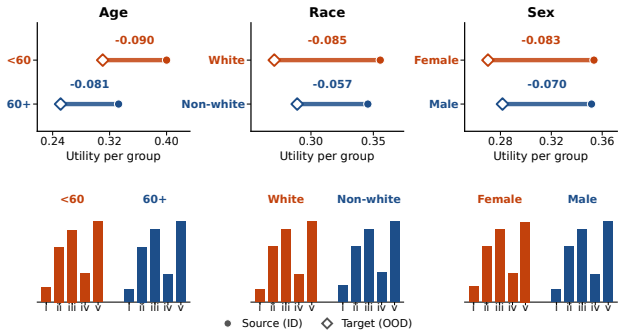

Figure 64: MIMIC-CXR → CheXpert Plus, Report Generation, utility change and OOD sources